

AD-A121 713

THEORY ELECTRO-OPTICAL DESIGN TESTING AND CALIBRATION
OF A PROTOTYPE ATMO..(U) OPHIR CORP DENVER CO

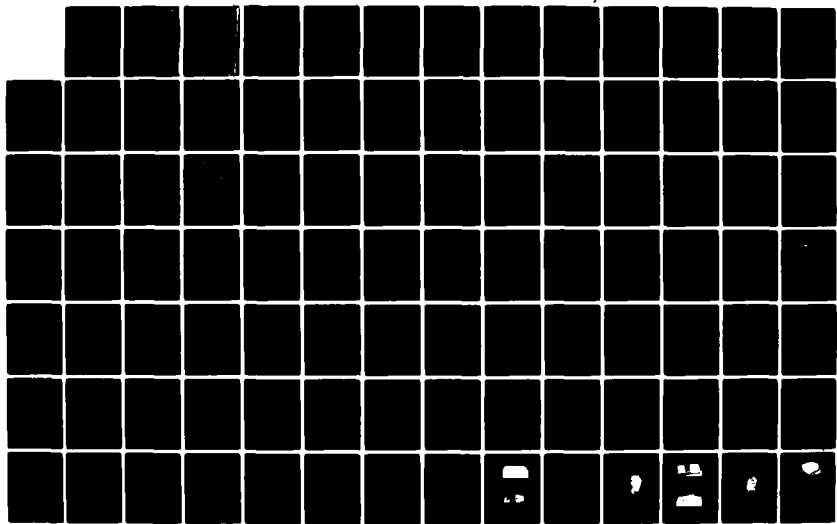
1/2

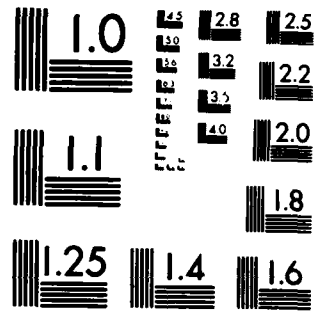
L D NELSON 15 JUL 82 AFGL-TR-82-0283 F19628-81-C-0071

F/G 4/2

NL

UNCLASSIFIED





MICROCOPY RESOLUTION TEST CHART
NATIONAL BUREAU OF STANDARDS-1963-A

AD A121713

AFML-TR-82-0400

**THEORY, PLANNING, TECHNICAL DESIGN, AND FIELD TESTS FOR
CALIBRATION OF A PHOTOGRAPHIC SYSTEM FOR MEASURING
SUPERSATURATION, HUMIDITY, AND DROplet SIZE IN THE ATMOSPHERE**

Loren D. Nelson

OPHIR Corporation
240 South Broadway
Denver, Colorado 80209

Final Report
March 1981 - July 1982

15 July 1982

Approved for public release; distribution unlimited

AIR FORCE GEOPHYSICS LABORATORY
AIR FORCE SYSTEMS COMMAND
UNITED STATES AIR FORCE
WRIGHT-PATTERSON AFB, OHIO 45433-6731

DTIC
SELECTED
S NOV 22 1982

82 11 22 116

Qualified requesters may obtain additional information from the Defense Technical Information Center, and a copy of the report will be supplied to the National Technical Information Service.

REPORT DOCUMENTATION PAGE		READ INSTRUCTIONS BEFORE COMPLETING FORM								
1. REPORT NUMBER AFGL-TR-82-0283	2. GOVT ACCESSION NO. AD-A222 723	3. RECIPIENT'S CATALOG NUMBER								
4. TITLE (and Subtitle) Theory, Electro-optical Design, Testing, and Calibration of a Prototype Atmospheric Supersaturation, Humidity, and Temperature Sensor	5. TYPE OF REPORT & PERIOD COVERED Final Report March 81 thru July 82									
7. AUTHOR(s) Loren D. Nelson	6. PERFORMING ORG. REPORT NUMBER									
9. PERFORMING ORGANIZATION NAME AND ADDRESS Ophir Corporation 240 S. Broadway Denver, CO 80209	10. PROGRAM ELEMENT, PROJECT, TASK AREA & WORK UNIT NUMBERS 62101F 667012BA									
11. CONTROLLING OFFICE NAME AND ADDRESS Air Force Geophysics Laboratory Hanscom AFB, Massachusetts 01731 Monitor/Robert O. Berthel/LYC	12. REPORT DATE 15 July 1982									
14. MONITORING AGENCY NAME & ADDRESS (if different from Controlling Office)	13. NUMBER OF PAGES 115									
	15. SECURITY CLASS. (of this report) Unclassified									
	15a. DECLASSIFICATION/DOWNGRADING SCHEDULE									
16. DISTRIBUTION STATEMENT (of this Report) Approved for public release; distribution unlimited.										
17. DISTRIBUTION STATEMENT (of the abstract entered in Block 20, if different from Report)										
18. SUPPLEMENTARY NOTES										
19. KEY WORDS (Continue on reverse side if necessary and identify by block number) <table> <tr> <td>Infrared Sensors</td> <td>Infrared Radiometry</td> </tr> <tr> <td>Humidity</td> <td>Supersaturation</td> </tr> <tr> <td>Temperature</td> <td>Vapor Transmissometer</td> </tr> <tr> <td>Air Temperature Radiometer</td> <td>Cloud Physics</td> </tr> </table>			Infrared Sensors	Infrared Radiometry	Humidity	Supersaturation	Temperature	Vapor Transmissometer	Air Temperature Radiometer	Cloud Physics
Infrared Sensors	Infrared Radiometry									
Humidity	Supersaturation									
Temperature	Vapor Transmissometer									
Air Temperature Radiometer	Cloud Physics									
20. ABSTRACT (Continue on reverse side if necessary and identify by block number) <p>A new infrared differential absorption - passive thermal emission based instrument designed to make accurate in-cloud measurements of absolute humidity, air temperature, relative humidity, and ice and water supersaturations has been developed.</p> <p>Absolute humidity is measured by the differential infrared</p>										

C-111

Unclassified

SECURITY CLASSIFICATION OF THIS PAGE(When Data Entered)

absorption of a broad-band light beam between 2.45 microns wavelength and the strongly absorbing water vapor band at 2.67 microns. Air temperature is sensed by a passive radiometric measurement of the Planck's law radiance emitted by carbon dioxide molecules in their very intense emission band at 4.25 microns. Significant operational advantages over previous 14-16 micron band radiometers are achieved. These non-contact optical measurements of absolute humidity and true air temperature can then be combined to yield relative humidity values with respect to both water and ice which remain valid in condensing supersaturated conditions and in spite of hydrometeors in the sample volume.

1

Authorization For	
NT - GRANT	
14-16 TIR	
U.S. Standard	
Instrumentation	
P-2	
Distribution	
1. 14-16 TIR	
2. 14-16 TIR	
3. 14-16 TIR	
4. 14-16 TIR	
5. 14-16 TIR	
6. 14-16 TIR	
7. 14-16 TIR	
8. 14-16 TIR	
9. 14-16 TIR	
10. 14-16 TIR	
11. 14-16 TIR	
12. 14-16 TIR	
13. 14-16 TIR	
14. 14-16 TIR	
15. 14-16 TIR	
16. 14-16 TIR	
17. 14-16 TIR	
18. 14-16 TIR	
19. 14-16 TIR	
20. 14-16 TIR	
21. 14-16 TIR	
22. 14-16 TIR	
23. 14-16 TIR	
24. 14-16 TIR	
25. 14-16 TIR	
26. 14-16 TIR	
27. 14-16 TIR	
28. 14-16 TIR	
29. 14-16 TIR	
30. 14-16 TIR	
31. 14-16 TIR	
32. 14-16 TIR	
33. 14-16 TIR	
34. 14-16 TIR	
35. 14-16 TIR	
36. 14-16 TIR	
37. 14-16 TIR	
38. 14-16 TIR	
39. 14-16 TIR	
40. 14-16 TIR	
41. 14-16 TIR	
42. 14-16 TIR	
43. 14-16 TIR	
44. 14-16 TIR	
45. 14-16 TIR	
46. 14-16 TIR	
47. 14-16 TIR	
48. 14-16 TIR	
49. 14-16 TIR	
50. 14-16 TIR	
51. 14-16 TIR	
52. 14-16 TIR	
53. 14-16 TIR	
54. 14-16 TIR	
55. 14-16 TIR	
56. 14-16 TIR	
57. 14-16 TIR	
58. 14-16 TIR	
59. 14-16 TIR	
60. 14-16 TIR	
61. 14-16 TIR	
62. 14-16 TIR	
63. 14-16 TIR	
64. 14-16 TIR	
65. 14-16 TIR	
66. 14-16 TIR	
67. 14-16 TIR	
68. 14-16 TIR	
69. 14-16 TIR	
70. 14-16 TIR	
71. 14-16 TIR	
72. 14-16 TIR	
73. 14-16 TIR	
74. 14-16 TIR	
75. 14-16 TIR	
76. 14-16 TIR	
77. 14-16 TIR	
78. 14-16 TIR	
79. 14-16 TIR	
80. 14-16 TIR	
81. 14-16 TIR	
82. 14-16 TIR	
83. 14-16 TIR	
84. 14-16 TIR	
85. 14-16 TIR	
86. 14-16 TIR	
87. 14-16 TIR	
88. 14-16 TIR	
89. 14-16 TIR	
90. 14-16 TIR	
91. 14-16 TIR	
92. 14-16 TIR	
93. 14-16 TIR	
94. 14-16 TIR	
95. 14-16 TIR	
96. 14-16 TIR	
97. 14-16 TIR	
98. 14-16 TIR	
99. 14-16 TIR	
100. 14-16 TIR	
101. 14-16 TIR	
102. 14-16 TIR	
103. 14-16 TIR	
104. 14-16 TIR	
105. 14-16 TIR	
106. 14-16 TIR	
107. 14-16 TIR	
108. 14-16 TIR	
109. 14-16 TIR	
110. 14-16 TIR	
111. 14-16 TIR	
112. 14-16 TIR	
113. 14-16 TIR	
114. 14-16 TIR	
115. 14-16 TIR	
116. 14-16 TIR	
117. 14-16 TIR	
118. 14-16 TIR	
119. 14-16 TIR	
120. 14-16 TIR	
121. 14-16 TIR	
122. 14-16 TIR	
123. 14-16 TIR	
124. 14-16 TIR	
125. 14-16 TIR	
126. 14-16 TIR	
127. 14-16 TIR	
128. 14-16 TIR	
129. 14-16 TIR	
130. 14-16 TIR	
131. 14-16 TIR	
132. 14-16 TIR	
133. 14-16 TIR	
134. 14-16 TIR	
135. 14-16 TIR	
136. 14-16 TIR	
137. 14-16 TIR	
138. 14-16 TIR	
139. 14-16 TIR	
140. 14-16 TIR	
141. 14-16 TIR	
142. 14-16 TIR	
143. 14-16 TIR	
144. 14-16 TIR	
145. 14-16 TIR	
146. 14-16 TIR	
147. 14-16 TIR	
148. 14-16 TIR	
149. 14-16 TIR	
150. 14-16 TIR	
151. 14-16 TIR	
152. 14-16 TIR	
153. 14-16 TIR	
154. 14-16 TIR	
155. 14-16 TIR	
156. 14-16 TIR	
157. 14-16 TIR	
158. 14-16 TIR	
159. 14-16 TIR	
160. 14-16 TIR	
161. 14-16 TIR	
162. 14-16 TIR	
163. 14-16 TIR	
164. 14-16 TIR	
165. 14-16 TIR	
166. 14-16 TIR	
167. 14-16 TIR	
168. 14-16 TIR	
169. 14-16 TIR	
170. 14-16 TIR	
171. 14-16 TIR	
172. 14-16 TIR	
173. 14-16 TIR	
174. 14-16 TIR	
175. 14-16 TIR	
176. 14-16 TIR	
177. 14-16 TIR	
178. 14-16 TIR	
179. 14-16 TIR	
180. 14-16 TIR	
181. 14-16 TIR	
182. 14-16 TIR	
183. 14-16 TIR	
184. 14-16 TIR	
185. 14-16 TIR	
186. 14-16 TIR	
187. 14-16 TIR	
188. 14-16 TIR	
189. 14-16 TIR	
190. 14-16 TIR	
191. 14-16 TIR	
192. 14-16 TIR	
193. 14-16 TIR	
194. 14-16 TIR	
195. 14-16 TIR	
196. 14-16 TIR	
197. 14-16 TIR	
198. 14-16 TIR	
199. 14-16 TIR	
200. 14-16 TIR	
201. 14-16 TIR	
202. 14-16 TIR	
203. 14-16 TIR	
204. 14-16 TIR	
205. 14-16 TIR	
206. 14-16 TIR	
207. 14-16 TIR	
208. 14-16 TIR	
209. 14-16 TIR	
210. 14-16 TIR	
211. 14-16 TIR	
212. 14-16 TIR	
213. 14-16 TIR	
214. 14-16 TIR	
215. 14-16 TIR	
216. 14-16 TIR	
217. 14-16 TIR	
218. 14-16 TIR	
219. 14-16 TIR	
220. 14-16 TIR	
221. 14-16 TIR	
222. 14-16 TIR	
223. 14-16 TIR	
224. 14-16 TIR	
225. 14-16 TIR	
226. 14-16 TIR	
227. 14-16 TIR	
228. 14-16 TIR	
229. 14-16 TIR	
230. 14-16 TIR	
231. 14-16 TIR	
232. 14-16 TIR	
233. 14-16 TIR	
234. 14-16 TIR	
235. 14-16 TIR	
236. 14-16 TIR	
237. 14-16 TIR	
238. 14-16 TIR	
239. 14-16 TIR	
240. 14-16 TIR	
241. 14-16 TIR	
242. 14-16 TIR	
243. 14-16 TIR	
244. 14-16 TIR	
245. 14-16 TIR	
246. 14-16 TIR	
247. 14-16 TIR	
248. 14-16 TIR	
249. 14-16 TIR	
250. 14-16 TIR	
251. 14-16 TIR	
252. 14-16 TIR	
253. 14-16 TIR	
254. 14-16 TIR	
255. 14-16 TIR	
256. 14-16 TIR	
257. 14-16 TIR	
258. 14-16 TIR	
259. 14-16 TIR	
260. 14-16 TIR	
261. 14-16 TIR	
262. 14-16 TIR	
263. 14-16 TIR	
264. 14-16 TIR	
265. 14-16 TIR	
266. 14-16 TIR	
267. 14-16 TIR	
268. 14-16 TIR	
269. 14-16 TIR	
270. 14-16 TIR	
271. 14-16 TIR	
272. 14-16 TIR	
273. 14-16 TIR	
274. 14-16 TIR	
275. 14-16 TIR	
276. 14-16 TIR	
277. 14-16 TIR	
278. 14-16 TIR	
279. 14-16 TIR	
280. 14-16 TIR	
281. 14-16 TIR	
282. 14-16 TIR	
283. 14-16 TIR	
284. 14-16 TIR	
285. 14-16 TIR	
286. 14-16 TIR	
287. 14-16 TIR	
288. 14-16 TIR	
289. 14-16 TIR	
290. 14-16 TIR	
291. 14-16 TIR	
292. 14-16 TIR	
293. 14-16 TIR	
294. 14-16 TIR	
295. 14-16 TIR	
296. 14-16 TIR	
297. 14-16 TIR	
298. 14-16 TIR	
299. 14-16 TIR	
300. 14-16 TIR	
301. 14-16 TIR	
302. 14-16 TIR	
303. 14-16 TIR	
304. 14-16 TIR	
305. 14-16 TIR	
306. 14-16 TIR	
307. 14-16 TIR	
308. 14-16 TIR	
309. 14-16 TIR	
310. 14-16 TIR	
311. 14-16 TIR	
312. 14-16 TIR	
313. 14-16 TIR	
314. 14-16 TIR	
315. 14-16 TIR	
316. 14-16 TIR	
317. 14-16 TIR	
318. 14-16 TIR	
319. 14-16 TIR	
320. 14-16 TIR	
321. 14-16 TIR	
322. 14-16 TIR	
323. 14-16 TIR	
324. 14-16 TIR	
325. 14-16 TIR	
326. 14-16 TIR	
327. 14-16 TIR	
328. 14-16 TIR	
329. 14-16 TIR	
330. 14-16 TIR	
331. 14-16 TIR	
332. 14-16 TIR	
333. 14-16 TIR	
334. 14-16 TIR	
335. 14-16 TIR	
336. 14-16 TIR	
337. 14-16 TIR	
338. 14-16 TIR	
339. 14-16 TIR	
340. 14-16 TIR	
341. 14-16 TIR	
342. 14-16 TIR	
343. 14-16 TIR	
344. 14-16 TIR	
345. 14-16 TIR	
346. 14-16 TIR	
347. 14-16 TIR	
348. 14-16 TIR	
349. 14-16 TIR	
350. 14-16 TIR	
351. 14-16 TIR	
352. 14-16 TIR	
353. 14-16 TIR	
354. 14-16 TIR	
355. 14-16 TIR	
356. 14-16 TIR	
357. 14-16 TIR	
358. 14-16 TIR	
359. 14-16 TIR	
360. 14-16 TIR	
361. 14-16 TIR	
362. 14-16 TIR	
363. 14-16 TIR	
364. 14-16 TIR	
365. 14-16 TIR	
366. 14-16 TIR	
367. 14-16 TIR	
368. 14-16 TIR	
369. 14-16 TIR	
370. 14-16 TIR	
371. 14-16 TIR	
372. 14-16 TIR	
373. 14-16 TIR	
374. 14-16 TIR	
375. 14-16 TIR	
376. 14-16 TIR	
377. 14-16 TIR	
378. 14-16 TIR	
379. 14-16 TIR	
380. 14-16 TIR	
381. 14-16 TIR	
382. 14-16 TIR	
383. 14-16 TIR	
384. 14-16 TIR	
385. 14-16 TIR	
386. 14-16 TIR	
387. 14-16 TIR	
388. 14-16 TIR	
389. 14-16 TIR	
390. 14-16 TIR	
391. 14-16 TIR	
392. 14-16 TIR	
393. 14-16 TIR	
394. 14-16 TIR	
395. 14-16 TIR	
396. 14-16 TIR	
397. 14-16 TIR	
398. 14-16 TIR	
399. 14-16 TIR	
400. 14-16 TIR	
401. 14-16 TIR	
402. 14-16 TIR	
403. 14-16 TIR	
404. 14-16 TIR	
405. 14-16 TIR	
406. 14-16 TIR	
407. 14-16 TIR	
408. 14-16 TIR	
409. 14-16 TIR	
410. 14-16 TIR	
411. 14-16 TIR	
412. 14-16 TIR	
413. 14-16 TIR	
414. 14-16 TIR	
415. 14-16 TIR	
416. 14-16 TIR	
417. 14-16 TIR	
418. 14-16 TIR	
419. 14-16 TIR	
420. 14-16 TIR	
421. 14-16 TIR	
422. 14-16 TIR	
423. 14-16 TIR	
424. 14-16 TIR	
425. 14-16 TIR	
426. 14-16 TIR	
427. 14-16 TIR	
428. 14-16 TIR	
429. 14-16 TIR	
430. 14-16 TIR	
431. 14-16 TIR	
432. 14-16 TIR	
433. 14-16 TIR	
434. 14-16 TIR	
435. 14-16 TIR	
436. 14-16 TIR	
437. 14-16 TIR	
438. 14-16 TIR	
439. 14-16 TIR	
440. 14-16 TIR	
441. 14-16 TIR	
442. 14-16 TIR	
443. 14-16 TIR	
444. 14-16 TIR	
445. 14-16 TIR	
446. 14-16 TIR	
447. 14-16 TIR	
448. 14-16 TIR	
449. 14-16 TIR	
450. 14-16 TIR	
451. 14-16 TIR	
452. 14-16 TIR	
453. 14-16 TIR	
454. 14-16 TIR	
455. 14-16 TIR	
456. 14-16 TIR	
457. 14-16 TIR	

Table of Contents

LIST OF ILLUSTRATIONS.....	1
1 OBJECTIVES OF THE STUDY.....	2
1.1 Introduction, Objectives, and End-User Relevance.....	2
1.1.1 Cloud Seeding Research and Operations.....	3
1.1.2 Ice Supersaturation Measurements.....	4
1.1.3 Clear-Air Ice Crystal Survival Studies.....	4
1.1.4 Liquid Water Supersaturations in Severe Storms.....	4
1.1.5 Shipboard Measurements in the Marine Boundary Layer.....	5
1.1.6 Atmospheric Effects on Electromagnetic Propagation.....	6
1.2 Possible Classes of Solutions/Design Requirements.....	6
1.3 Infrared Absorption of Water Vapor.....	7
1.3.1 Other Absorbing Gases.....	11
1.3.2 Differential Absorption Techniques.....	12
1.3.3 Rejection of Hydrometeors in the Sample Volume.....	13
1.3.4 Measuring Supersaturated Vapor.....	17
1.4 Passive 4.3 micrometer Carbon Dioxide Band Air Temperature Radiometry.....	18
1.4.1 Previous 14.3 Micrometer Band Radiometers.....	21
1.4.2 The Proposed 4.255 Micrometer Band Air Temperature Radiometer.....	23
1.5 Supersaturation Derived from Absolute Humidity and Air Temperature.....	26
2 INSTRUMENT DESIGN.....	26
2.1 Introduction.....	26
2.2 Functional Block Diagram.....	27
3 ABSOLUTE HUMIDITY SENSOR.....	31
3.1 Optical Design.....	31
3.1.1 Window Materials.....	31
3.1.2 Light Source.....	33
3.1.3 Focusing Optics.....	37
3.1.4 Beamsplitter.....	40
3.1.5 Infrared Wavelength Selection.....	42
3.1.6 Infrared Narrowband Filters.....	43
3.1.7 Potential Optical Problem Areas.....	44
3.2 Electronic Design.....	45
3.2.1 Lead Sulfide Photodetectors.....	45
3.2.2 DC Ratiometric Coupling.....	52
3.2.3 Transmissivity Transfer Equation.....	53
3.2.4 Light Source Filament Temperature Controller.....	56
3.2.5 Thermoelectric Lead Sulfide Temperature Control.....	58
3.2.6 Potential Electronic Problem Areas.....	59
3.3 Mechanical Design.....	61
3.3.1 Enclosures/Prototype System.....	61
3.3.2 Enclosure Desiccation.....	62
3.3.3 Zero and Span Calibration.....	63

3.3.4 Potential Mechanical Problem Areas.....	63
4 AIR TEMPERATURE RADIOMETER.....	63
4.1 Optical Design.....	64
4.1.1 Wavelength Selection.....	65
4.1.2 Aperture and Field of View Tradeoffs.....	65
4.1.3 Focusing Optics and Aperture Stops.....	66
4.1.4 Narrowband Infrared Filter.....	67
4.1.5 Instrument Thermal Emissions.....	68
4.1.6 Photo-Chopping Signal Modulation.....	68
4.1.7 Window Materials.....	70
4.1.8 Solar Blindness.....	70
4.1.9 Potential Optical Problem Areas.....	70
4.2 Electronic Design.....	70
4.2.1 Thermoelectrically Cooled Lead Selenide Photodetectors.....	70
4.2.2 Synchronous Chopper Driver.....	73
4.2.3 Digital Synchronous Demodulator.....	75
4.2.4 Reference Synthesis from Internal Temperature.....	78
4.2.5 Non-linear Conversion of Radiance to Temperature.....	78
4.2.6 Potential Electronic Problem Areas.....	80
4.3 Mechanical Design.....	80
4.3.1 Enclosures and Prototyping System.....	80
4.3.2 Carbon Dioxide Emissions in Enclosures.....	80
4.3.3 Potential Mechanical Problem Areas.....	80
5 SUPERSATURATION SENSOR DESIGN SUMMARY.....	81
5.1 Absolute Humidity Sensor Design Specification Goals.....	81
5.2 Air Temperature Radiometer Design Specification Goals.....	81
6 PROTOTYPE HARDWARE FABRICATION.....	82
6.1 Absolute Humidity Sensor Laboratory Prototype.....	82
6.2 Air Temperature 4.25 Micrometer Radiometer Laboratory Prototype.....	84
7 LABORATORY AND FIELD PROTOTYPE TESTING AND CALIBRATION.....	84
7.1 Absolute Humidity Sensor Testing.....	88
7.1.1 Laboratory Tests.....	88
7.1.2 Field Testing and Calibration.....	92
7.2 Air Temperature 4.25 Micrometer Radiometer Calibration and Testing.....	95
7.2.1 Laboratory Tests and Calibration.....	95
7.2.2 Field Tests of the 4.25 micrometer Air Temperature.....	97
8 SUMMARY AND CONCLUSIONS.....	98
8.1 Design Feasibility.....	98
8.2 Recommendations for Future Work.....	98
9 ACKNOWLEDGMENTS.....	101
REFERENCES.....	102
APPENDIX I (Manufacturer's Data Sheets).....	107

LIST OF ILLUSTRATIONS

<u>Figure</u>	<u>Legend</u>	<u>Page</u>
Fig. (1.1)	Saturation Vapor Density versus Temperature	3
Fig. (1.2)	Water Vapor Transmissivity at 2.665 Micrometers	9
Fig. (1.3)	Effects of $t(a)$ and $p(a)$ on Water Vapor Absorption	11
Fig. (1.4)	Infrared Hygrometer Conceptual Diagram	13
Fig. (1.5)	Particulate Extinction Cross Sections	15
Fig. (1.6)	Atmospheric Trace Gas Infrared Absorption	20
Fig. (1.7)	Black Body Spectral Radiance Curves	22
Fig. (1.8)	Spectral Radiance in the Carbon Dioxide Bands	23
Fig. (1.9)	Carbon Dioxide Band Emission versus Temperature	24
Fig. (1.10)	Radiometer Spatial Weighting Function	25
Fig. (2.1)	Supersaturation Sensor Block Diagram	27
Fig. (2.2)	Transmissometer Error Propagation	30
Fig. (2.3)	Air Temperature Error Propagation	30
Fig. (3.1)	Absorption Coefficient of Sapphire	32
Fig. (3.2)	Absolute Humidity Sensor Light Source	34
Fig. (3.3)	Quartz Absorption Coefficients	35
Fig. (3.4)	Vapor Pressure of Tungsten	36
Fig. (3.5)	Resistivity of Tungsten	37
Fig. (3.6)	Filament Temperature Control Accuracy	38
Fig. (3.7)	Parabolic Reflector Segment Shapes	39
Fig. (3.8)	Parabolic Reflector Segment Mount	40
Fig. (3.9)	Silicon Two-Surface Fresnel Reflectivity	42
Fig. (3.10)	Lead Sulfide Sensor Hermetic T0-5 Package	46
Fig. (3.11)	Spectral Response of Lead Sulfide	47
Fig. (3.12)	Semiconductor Band-Gap Structure	47
Fig. (3.13)	Photoconductor Test and Bias Circuit	50
Fig. (3.14)	Lead Sulfide Resistance Curve	51
Fig. (3.15)	Transmissometer Electro-optical Schematic	54
Fig. (3.16)	Switching Light Source Regulator Schematic	57
Fig. (3.17)	Switching Thermoelectric Cooler Schematic	59
Fig. (3.18)	Lead Sulfide D^* versus Chopper Frequency	60
Fig. (4.1)	Sensor Aperture and Field-of-view Relations	66
Fig. (4.2)	Temperature Sensor Optical Diagram	67
Fig. (4.3)	Lead Selenide Spectral Background Selectivity	69
Fig. (4.4)	Lead Selenide Low-level Amplifier Schematic	71
Fig. (4.5)	Photochopper Phase-Locked Driver Schematic	73
Fig. (4.6)	Photochopper Timing Diagram	74
Fig. (4.7)	Irradiance Signal Lock-in Demodulator	76
Fig. (4.8)	Temperature-Irradiance Converter Schematic	79
Fig. (6.1)	Absolute Humidity Sensor Readout Panel	83
Fig. (6.2)	Absolute Humidity Sensor Remote Head	83
Fig. (6.3)	Detailed View of Humidity Sensor Receiver (cover removed)	85
Fig. (6.4)	Absolute Humidity Sensor Head (cover in place)	86

Fig. (6.5)	Air Temperature Radiometer Readout Panel	86
Fig. (6.6)	Air Temperature Radiometer Remote Head (covers removed)	87
Fig. (6.7)	Air Temperature Radiometer Remote Head (covers in place)	88
Fig. (7.1)	Chart Recorder Trace Resulting from Breathing into Humidity Sensor Beampath	89
Fig. (7.2)	Preliminary Variable Path Tests of Absolute Humidity Sensor	90
Fig. (7.3)	Infrared Spectrophotometer Traces of Actual Filter Bandpass and Atmospheric Absorption Bands	91
Fig. (7.4)	Sensor Placement on NOAA/BAO Tower	93
Fig. (7.5)(a)	Scatter Diagram - Ophir Vapor Transmissometer Output Voltage versus Aspirated Dew Point Hygrometer Reading in Degrees Celsius (10 Second Averages)	94
Fig. (7.5)(b)	Scatter Diagram - NCAR Lyman-Alpha Hygrometer Output Voltage versus Aspirated Dew Point Hygrometer Reading in Degrees Celsius (10 Second Averages)	94
Fig. (7.6)	Ophir Air Temperature Radiometer Spatial Weighting Function	96
Fig. (7.7)	Laboratory Calibration of the Absolute Temperature Accuracy of Ophir 4.25 Micrometer Radiometer	97
Fig. (8.1)	Artist's Conception - Airborne 4.25 Micrometer Air Temperature Radiometer	99
Fig. (8.2)	Artist's Conception - Airborne 2.67 Micrometer Water Vapor Transmissometer	100

ACKNOWLEDGMENTS

A number of scientific and technical personnel outside Ophir Corporation have made contributions to the development and testing of the sensing technology presented herein. Dr. Arnold Barnes, Mr. Vernon Plank, and Mr. Robert Berthel of AFGL provided technical discussions and hardware equipment loans under the contract. A Black-Body Calibration Test Facility was made available by Dr. Byron Phillips and Mr. Alex Kennel of the NCAR Aviation Facility. Encouragement and laboratory and field test facilities were made available by Dr. Chandrin Kaimal of NOAA and Dr. John Wyngaard of NCAR. Dr. John Gaynor and Mr. Tant Priestley of NOAA made it possible for these sensors to take part in ongoing field trials at the Boulder Atmospheric Observatory. Field support was provided by Mr. Don Wolf, Mr. Norbert Szczepczynski, and Mr. Jim Newman of the Boulder Atmospheric Observatory.

1 OBJECTIVES OF THE STUDY

1.1 Introduction, Objectives, and End-User Relevance

Ophir Corporation, based on an unsolicited proposal, has been awarded Contract No.F19628-81-C-0071 from the U.S. Air Force Geophysics Laboratory (AFGL/LYC) to design, fabricate, and test a laboratory prototype of an airborne absolute humidity, in cloud air temperature, and supersaturation sensor. This airborne device is intended for accurate use in hydrometeor filled condensing environments in the interior of clouds and at high altitude subfreezing temperatures.

The proposed atmospheric moisture and supersaturation sensing device is an adaptation of an existing proprietary (patent pending) Ophir Corporation technology and involves simultaneous active and passive differential infrared irradiance measurements in the vibration-rotation absorption bands of water vapor and carbon dioxide. This final report entitled 'Theory, Electro-optical Design, Testing, and Calibration of a Prototype Atmospheric Supersaturation, Humidity, and Temperature Sensor' is the last deliverable end item called for in the contract. It contains a theoretical description of the devices and the actual engineering implementation that was accomplished during construction and testing.

Atmospheric moisture content has always been one of the most difficult physical measurements required of the meteorological community. Showalter (1965) pointed out many of the difficulties which still remain more than a decade later as evidenced by the survey of McKay (1978). Such problems in achieving reliable moisture measurements are compounded when the sample must be taken from a rapidly moving aircraft in in situ undisturbed environmental conditions, in the presence of hydrometeors, at very high or very low relative humidities, in subfreezing environments, without significant hysteresis, at low absolute humidity, over a wide dynamic range, or with a fast response time. Figure (1.1) shows the saturation vapor density of water vapor as a function of temperature. Measurements of vapor content made in clouds can be expected to fall near or within Regions II or III on Figure (1.1) where all of the above conditions are most likely to compound measurement problems.

Because of the difficulty of such measurement conditions, no commercial or research instrument available today is capable of making in-cloud measurements in supersaturated vapor. The simpler problem of accurate moisture measurement in cloudy but unsaturated conditions is also unsolved. Johnson and Smith (1980) report that they have chosen not to include a humidity sensor on their sophisticated T-28 thunderstorm aircraft at the Institute of Atmospheric Sciences of the South Dakota School of Mines and Technology. They have made this decision because the emphasis of their research '...is on the interior characteristics of storms and no satisfactory method is available for measuring humidity in clouds.' Unfortunately, this same in-cloud quasi-saturated environment is the moisture condition of most interest to the cloud physics and weather modification communities.

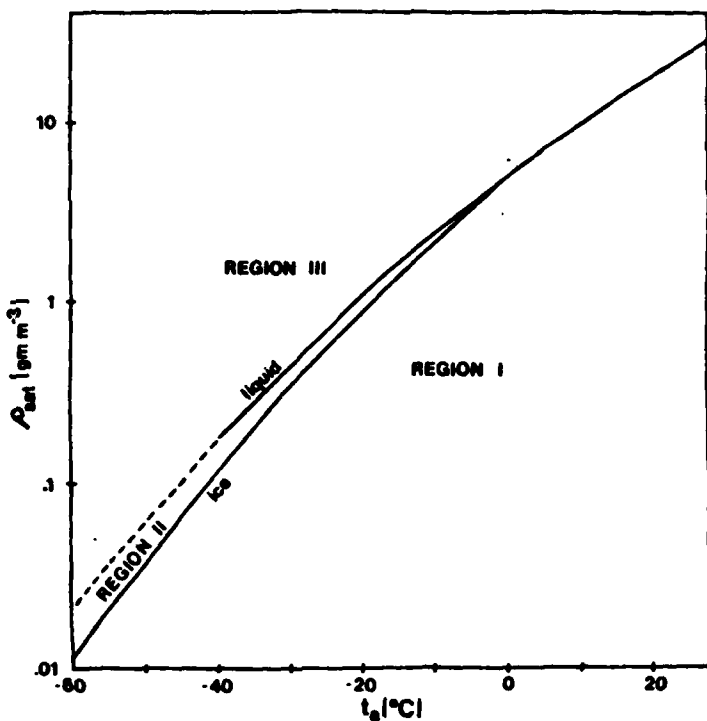


Fig. (1.1) Saturation Vapor Density versus Temperature

1.1.1 Cloud Seeding Research and Operations

Gerber (1981) recently described a new and innovative moisture sensor based on the equilibrium size of small salt droplets of known nuclei content on a very thin thermally heated substrate. The device is reported to have a range of 95 - 105% relative humidity. Transitory humidity excursions outside this range can destroy the delicate sensing surface and the device is not suited for subfreezing use and has a slow response time. Even this new state-of-the-art instrument does not seem to be suited to routine in-cloud airborne humidity measurement. Yet, the entire science of cold cloud and winter weather modification with ice-forming agents such as silver iodide and dry ice is predicated upon the rapid transfer of water substance from liquid to ice hydrometeors by means of intermediary vapor supersaturations with respect to ice. Vapor densities in or above Region II are thus a necessary condition for such cloud seeding to be effective and it can be readily argued that in-cloud ice supersaturation ratios would be an excellent quantitative indicator of cloud seedability. Ice nucleation on both natural and artificial ice nuclei is critically dependent upon available supersaturation (Anderson

and Hallett, 1976; Edwards and Evans, 1960; Gagin, 1972; Huffman, 1973). Once nucleated, ice crystal habits, growth rates, and modes are also strongly supersaturation dependent (Pruppacher and Klett, 1978; Lamb and Hobbs, 1971; Rottner and Vali, 1974). The subsequent growth of these crystals when the vapor is supersaturated with respect to ice is by way of the Bergeron-Findeisen process, the dominant mid and high latitude precipitation forming mechanism.

1.1.2 Ice Supersaturation Measurements

Lala (1969), in an extensive series of tests using dry ice carried by balloons, has shown that clear air layers of ice supersaturation but water subsaturation exist in the atmosphere about 3% of the time. Since it has been conclusively demonstrated that ice nucleation on deposition nuclei commonly occurs at water subsaturation (Huffman, 1973; Gagin, 1972), such unstable layers are fundamentally due to a dearth of deposition ice nuclei rather than a lack of water saturation. Such unstable clear-air ice-supersaturation layers have military relevance to contrail formation and provide a mechanism whereby persistent contrails from heavy commercial jet traffic can influence the earth's local thermal radiation budget (Kuhn, 1970; Knollenberg, 1972). While attempts have been made to investigate such layers with carbon strip hygrometers (Bigg and Meade, 1971), such results must be viewed with extreme caution since any solid surface exposed to such conditions is likely to act as a substrate for deposition ice nucleation. Therefore, reliable quantitative measurements have awaited the development of a non-contact sensor.

1.1.3 Clear-Air Ice Crystal Survival Studies

Reports of ice crystal survival and growth in clear-air can be found in a growing number of literature sources. See, for example, Braham and Spyres-Duran (1967) and Hall and Pruppacher (1976). This phenomenon has relevance to climatic models, global radiative transfer balances, natural ice crystal seeding of developing thunderstorms, and a number of military applications such as aerospace vehicles and optical radiation sources and sensors. Again, the lack of an airborne measurement capability for humidity above ice saturation has prevented quantification of this apparently common phenomenon in the high troposphere.

1.1.4 Liquid Water Supersaturations in Severe Storms

The very existence of water clouds is prima facie evidence of at least transitory supersaturation with respect to liquid water in the free atmosphere. Early numerical simulations of the beginning stages of condensation on a nuclei distribution at cloud base (Neiburger and Chien, 1960; Howell, 1949), found that under these conditions supersaturation was transitory and did not exceed about 0.1%. This quantity is still tacitly accepted today by most of the cloud physics community. Since physical contact sensors such as rawinsonde humidity

elements and dew point mirrors will become watercoated and cannot measure saturation ratios greater than one, it is common practice to use an assumed in-cloud humidity of 100% to correct for sensor calibration drifts. However, one must be cautious not to use the lack of a measurement capability as an argument to support the hypothesis that a phenomenon does not exist. Absence of evidence is not evidence of absence. In condensation nuclei free conditions, the atmosphere can theoretically support water vapor saturation ratios of 300 - 400% before homogeneous nucleation occurs (Pruppacher and Klett, 1978). Such conditions are routinely achieved in laboratory expansion cloud chambers (Allen and Kassner, 1969), and in thermal diffusion chambers (Heist and Reiss, 1973). Das (1969) was the first to point out that the rate of production of available vapor by adiabatic expansion in the central cores of cumulus updrafts could easily exceed the rate of vapor condensation onto the existing hydrometeors in the updraft, resulting in large supersaturations. He hypothesized that the conditions in such updraft cores would also be favorable to the scavenging of the cloud condensation nuclei (CCN) aerosol to the droplets, thus inhibiting the activation of new droplets that might otherwise lower the supersaturation. By means of numerical models wherein the rates of vapor production and depletion are decoupled, and assuming no new activation of droplets above cloud base, several authors have theoretically computed supersaturations of 110 - 150% in such updraft cores (Clark, 1973; Soong, 1974; Nelson, 1979). Subbarao and Das (1975) explicitly formulated rates of nuclei scavenging and activation in a model that produced saturation ratios in excess of 1.07. If such high water saturation ratios could be experimentally verified in strong cumulus updrafts, they would constitute a new mechanism of precipitation formation to augment the Bergeron-Findeisen and coalescence processes.

1.1.5 Shipboard Measurements in the Marine Boundary Layer

The salt-spray environment of the low-level marine boundary layer is extremely destructive to conventional humidity sensors. Both outright failures and unpredictable calibration drifts occur. The non-contact sensor to be described in this document, however, presents only a totally inert sapphire window to the marine environment and thus is not subject to such failures. In fact, the proposed sensor can be totally immersed in salt water without damage or loss of calibration, thus suiting it to shipboard use. Liquid water droplets on the sapphire window and partial salt encrustations are automatically compensated by the differential measurement technique to be presented in Section (1.3.2) and by the choice of system wavelengths to be more sensitive to vapor than liquid water as discussed in Section (1.3). The proposed sensor thus would, for example, be extremely well suited to the investigation of refractive index caused radar ducting in the low-level marine inversion layer.

1.1.6 Atmospheric Effects on Electromagnetic Propagation

Refractive index changes caused by humidity and temperature fluctuations have significant effects on the propagation of infrared and microwave radiation through the atmosphere. Peak atmospheric degradation of radar signals occurs from fluctuations on the scale of one-half the transmitted wavelength. Airborne measurements of the temperature structure function are feasible on this scale length (Balsey and Peterson, 1981) but the humidity component has apparently never been directly measured since existing moisture sensors have such slow response times and large hysteresis. The sensor proposed here will have a response time on the order of 1000 microseconds and thus should permit in situ humidity and composite refractive index structure function measurements from fast moving aircraft. Minor redesign could result in even faster response times.

1.2 Possible Classes of Solutions/Design Requirements

Having shown the operational need for and utility of an airborne supersaturation sensor, a number of stringent design criteria can be listed which, if simultaneously met, will theoretically allow such a measurement of vapor, both sub- and supersaturation, in the presence of cloud. Such a sensor should:

- a. measure without physical contact since condensation would form on exposed sensors prohibiting the measurement of supersaturated vapor (See Gerber, 1981 for an alternative but essentially impractical approach);
- b. sample in situ without sampling chambers or plumbing to avoid disturbing disequilibrium conditions in the environment;
- c. reject liquid and ice hydrometeors in the sample volume and potentially wetting exposed sensor surfaces;
- d. have sufficient accuracy that instrument error and noise is much smaller than the saturation ratios of interest over a dynamic range of several orders of magnitude in absolute humidity;
- e. measure some variant of absolute humidity (i.e., grams per cubic meter) and then calculate saturation ratio by means of a concurrent and also noncontacting ambient temperature measurement (no sensors are available for direct non-contact measurement of relative humidity);
- f. avoid adding or subtracting moisture to or from the environment, to avoid disturbing disequilibrium conditions;
- g. be capable of use from a moving aircraft and be hysteresis free with a rapid response time (i.e., on the order of milliseconds) to achieve good spatial resolution.

Satisfying the above criteria for an airborne in-cloud supersaturation sensor design thus requires two simultaneous but essentially independent measurements. First, one must measure absolute humidity (grams per cubic meter) with a non-contacting sensor. Candidate devices for this include the Lyman-Alpha hygrometer, microwave hygrometers, refractive index instruments, and infrared absorption hygrometers. The absolute humidity measurement will be implemented by way of a measurement of infrared short path transmissivity at the water vapor 2.67 micrometer vibration-rotation absorption peak. The second instrumental requirement is a non-contact measurement of air temperature that is not affected by hydrometeors in its sample volume. Candidate devices for this include a carefully compensated sonic anemometer configured to extract the temperature component of sound velocity and passive infrared radiometry in a strong atmospheric absorption band. The proposed instrument will measure true air temperature by way of passive measurement of atmospheric irradiance in the strong 4.25 micrometer vibration-rotation band of carbon dioxide. Having measured absolute humidity and true air temperature by way of non-contacting means; a simple table lookup of the temperature dependent saturation water vapor density enables a calculation of saturation ratio with respect to either water or ice. Computed values remain accurate regardless of supersaturated atmospheric conditions. Before presenting a proposed hardware implementation of these devices, a brief review of the theory of infrared gas radiometry is presented to provide a framework for the engineering design tradeoffs that will be given in later sections.

1.3 Infrared Absorption of Water Vapor

While the details of the molecular water vapor absorption band mechanism are complex and quantum mechanical in origin (Wyatt *et al.*, 1964), for the purposes of this discussion it will be sufficient to think of the water vapor molecule as a tiny oscillator or 'tuning fork' capable of being excited in a number of resonant modes and harmonics by impinging electromagnetic radiation. It thus acts as a micro-miniature optical analog of a violin string resonating in response to an externally applied sound at its natural frequency. Since the water molecule is non-linear it can have resonances due to vibrational, rotational, and combined vibration-rotation modes. Fundamental vibrational resonances occur at wavelengths of 6.269, 2.738, and 2.663 micrometers with a large number of overtones and combination resonances extending into the visible region of the electromagnetic spectrum (Johns, 1965). If a collimated beam of monochromatic incident radiation of some given wavelength is passed through a water vapor atmosphere then the fractional absorption of the beam due to the vapor is given by the Beer-Lambert Absorption Law which we can express as:

$$T = I/I_0 = \exp (-K_\lambda P_r) \quad (1.1)$$

where T is the fraction of the beam transmitted, $I(0)$ is the incident radiation intensity, I is the emergent radiation intensity, $K(\lambda)$ is the water vapor absorption coefficient at wavelength $[\lambda]$, and $P(r)$ is the precipitable equivalent depth of water vapor in the beam path as given by:

$$P_r = 1.0 \times 10^{-6} \{ \rho_w / \rho_l \} L \quad (1.2)$$

where $\rho(w)$ is the absolute humidity in grams per cubic meter, L is the path length in centimeters, $\rho(l)$ is the density of liquid water in grams per cubic centimeter. It is important to note that the absorption $[A]$ due to a given equivalent vapor depth $[P(r)]$ in the vapor state will not be the same as that due to a liquid layer of the same depth $[P(r)]$. In liquid water the resonating molecules are confined by their close neighbors and resonant frequencies and intensities are shifted from those of the vapor state. Because of this damping effect, the absorption coefficient of liquid water changes much less rapidly with wavelength than does that of vapor. For liquid layer absorption, Equation (1.1) thus holds for narrow band (± 0.01 micrometers) illumination as well as for strictly monochromatic light. For water molecules in the vapor state illuminated by narrow band radiation, the situation is much more complex. Even at a narrow infrared filter bandwidth of ± 0.01 micrometers, many absorption lines are present, each having a different $K(\lambda)$ coefficient. When the nonlinear absorption contributions from these many lines are summed over the narrow band wavelength range, the non-monochromatic nature of the light causes so called 'instrumental' deviations from Equation (1.1). Elsasser and Culbertson (1960) have proposed that for narrow band radiation over a limited range of absorption (A) one can approximate:

$$A = (1.0 - T) = k P_r^{\frac{1}{2}} \quad (1.3)$$

A more complex but accurate formulation valid over a wider range of absorption $[A]$ is given by Bogomolova et al. (1974) as:

$$I_{\Delta\lambda} / I_0 = \exp (-K_{\Delta\lambda} P_r^B) \quad (1.4)$$

where $\Delta\lambda$ indicates a narrow but non-monochromatic wavelength interval and B is a constant exponent. Figure (1.2) illustrates this instrumental deviation from Beer's Law for a narrow band light source at a center wavelength of 2.665 micrometers and spectral width of ± 0.01 micrometers. Triangles indicate the data of Wyatt et al., (1962) and the smooth line is the best fit to those data obtained from Equation (1.4) where $K(\Delta\lambda) = 15.82 \text{ cm}^{-1}$ and $B = 0.360$. The transmission that would result from a liquid water depth of $P(r)$ is also plotted on Figure (1.2) using Equation (1.1) where the liquid water absorption coefficient is $K(2.67 \text{ micrometers, liquid}) = 162.2 \text{ cm}^{-1}$ as taken from the data of Irvine and Pollack (1968). The labeled ice absorption line represents the absorption of an equal amount of bulk ice using $K(2.67 \text{ micrometers, ice}) = 116.0 \text{ cm}^{-1}$ as given by the same authors and assuming the density of ice to be 0.917 grams per cubic centimeter. The upper scale converts precipitable water to absolute humidity by way of Equation (1.2) assuming a path length of 20 centimeters. It can be seen from Figure (1.2) that measurement of a transmission ratio $[T]$ of narrow band 2.665 micrometers radiation through water vapor can be theoretically expected to give a valid measurement of water vapor density over a dynamic range of at least four orders of magnitude in absolute humidity. Further, at this particular wavelength, the absorption will be much more sensitive to vapor than liquid water. At transmissions higher than 30%, the band transmission is more than an order of magnitude more sensitive to water vapor than to liquid water. Solid ice is rejected at an even higher level. This counter-intuitive behavior is a function of the

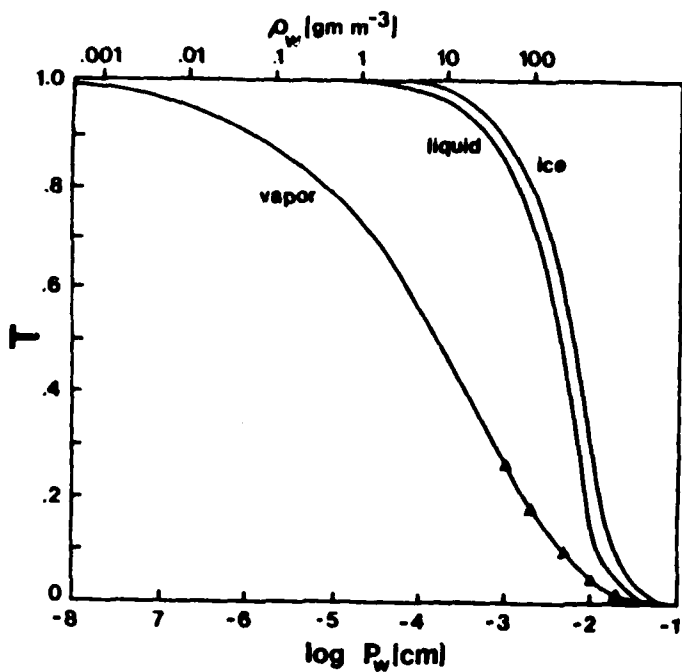


Fig. (1.2) Water Vapor Transmissivity at 2.665 micrometers

particular wavelength chosen (2.665 micrometers) and is not generally true at most other wavelengths. It occurs here because the 2.665 micrometer band is the most intense water vapor absorption band to be found anywhere between 1.0 and 9.5 micrometers when viewed with a 0.02 micrometer bandpass filter and is located at the lower wavelength edge of a band of intense water vapor absorption. In liquid water the band absorption peak is shifted to longer wavelengths (2.95 micrometers) and is a much less rapidly changing function of wavelength and therefore Equation (1.1) represents the liquid absorption law. The ice absorption peak is shifted even farther to 3.075 micrometers as shown by Irvine and Pollack (1968). The resulting high rejection of bulk liquid water and ice at the 2.665 micrometer water vapor absorption peak is an important factor in the rejection of hydrometeors in the instrument sample volume and possible water and ice on instrument windows. It can also be seen from Figure (1.2) that such a humidity sensor based on the measurement of transmission [T] has the uniquely desirable property of actually becoming more sensitive at lower absolute humidities. This is in sharp contrast to conventional sensors such as dewcells, cooled surfaces, and psychrometric hygrometers that become less sensitive under such conditions.

The data shown in Figure (1.2) illustrate the infrared absorption of water vapor at a temperature of 300° Kelvin at sea level. However, the absorption of narrowband infrared radiation by water vapor also is influenced to second order by both ambient pressure and temperature. When a resonating water vapor molecule collides with another molecule (probably nitrogen or oxygen in the free atmosphere) it is detuned slightly from its natural frequency. The many discreet quantum absorption lines in a narrow (i.e. ± 0.01 micrometer) bandpass interval will thus be pressure-broadened by these collisions and the total transmission [T] in the band will decrease as the amount of water vapor [$P(r)$] is increased at constant atmospheric pressure [$p(a)$] and will also always decrease as the ambient pressure is increased while the amount of water vapor is held constant.

A second order water vapor absorption dependence on ambient temperature is also present and is caused by a temperature dependence of the frequency of molecular collisions (Burch *et al.*, 1962). Over the tropospheric range of pressure and temperature, this pressure and temperature dependence can be accurately represented as:

$$A = (1.0 - T) = 1.0 - \exp\{kP_r^B (p_a/p_0)^C (t_0/t_a)^D\} \quad (1.5)$$

Figure (1.3) graphically illustrates the pressure and temperature dependence of water vapor absorption set forth in Equation (1.5) at a wavelength of 2.665 micrometers and a ± 0.01 micrometer filter bandpass. Under these conditions the coefficients of best fit in Equation 1.5 are $k = -15.82$, $B = 0.360$, $C = 0.365$, and $D = 0.350$. The triangular symbols in the figure represent the data of Wyatt *et al.*, from which these coefficients of best fit were calculated. The symbols $t(a)$ and $p(a)$ represent standard conditions at 1 atmosphere and 300° Kelvin. From the long quasi-linear sections of the curves, it can be seen that logarithmic interpolation of A over pressure and temperature is justified and that for small A and over fairly wide ranges of $P(a)$, the simplification of Elsasser and Culbertson (1960), given here as Equation (1.3), is reasonably valid as a limiting approximation to the more generally valid relation given as Equation (1.5).

Equation (1.5) provides a measure of the absorption [A] caused by a given amount of precipitable water vapor [$P(a)$] at any ambient pressure [$p(a)$] and ambient temperature [$t(a)$]. Equation (1.2) permits the calculation of absolute humidity [$\rho(a)$] from a measure of precipitable water vapor [$P(r)$] taken at a given instrument path length [L]. Substitution of Equation (1.2) into Equation (1.5) and a rearrangement of terms thus permits an accurate calculation of absolute humidity [$\rho(a)$], given a pathlength [L] and concurrent measurements of A or T , $p(a)$ and $t(a)$. The equation remains valid for any combination of these parameters to be found in the troposphere.

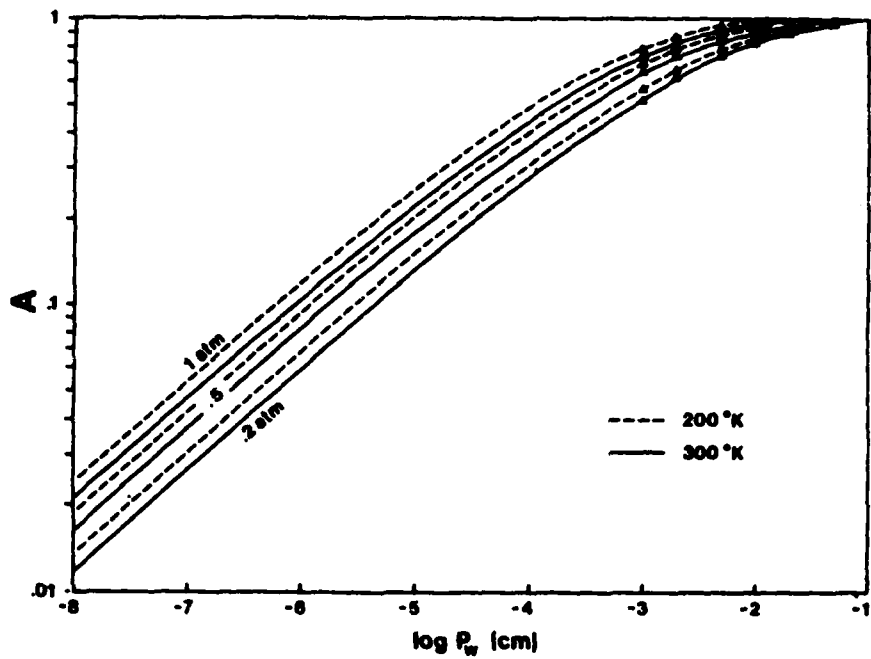


Fig. (1.3) Effects of $t(a)$ and $p(a)$ on Water Vapor Absorption

1.3.1 Other Absorbing Gases

Equation (1.5) will only be accurate at 2.665 micrometers if no other atmospheric constituents or trace gases contribute significantly to A at that wavelength. Rothman *et al.*, (1978) have compiled transmission data for the seven primary infrared active atmospheric constituents (water vapor, carbon dioxide, ozone, nitrous oxide, sulfur dioxide, nitrogen dioxide, and ammonia). Of these listed gases only water vapor and carbon dioxide absorb significantly at 2.665 micrometers. It will be shown in a later section of this report that a path length, $L = 20$ centimeters, represents a practical hygrometer size. At an assumed carbon dioxide concentration of 0.033% by volume and standard temperature and pressure there will be 0.0066 atmosphere centimeters of carbon dioxide in this path length. Absorbing path lengths of carbon dioxide are, by convention, given in units of atmosphere centimeters. Values of carbon dioxide absorber concentration in these units are determined by multiplying the absorber path length in centimeters by the partial pressure of the absorbing carbon dioxide in atmospheres, corrected to standard temperature. The data of Stull *et al.* (1964) indicates that the absorption of this amount of carbon dioxide will be

much less than 0.1% and thus totally negligible in comparison to the extremely strong water vapor band at 2.665 micrometers.

1.3.2 Differential Absorption Techniques

Instrumentation for water vapor measurements via infrared absorption has been in existence since Fowle (1912) used the sun as a source for a spectroscopic bolometer estimate of the total atmospheric vapor content. Since his early work, each new advance in technology has led many other authors to propose solar slant path and artificial source infrared hygrometers (Foskett and Foster, 1943; Foskett *et al.*, 1953; Wood, 1958; Tank and Wergin, 1965; Statts *et al.*, 1965; Vyaltseva *et al.*, 1969; Bogomolova *et al.*, 1974; Hyson and Hicks 1975; and Tomasi and Guzzi, 1974). Such instruments have in general tended to be complex, prone to calibration drifts, bulky and electrically power intensive, composed of complex mechanically moving parts such as optical chopping wheels and servo driven wedges, and have usually required long path lengths. Logarithmic and power law response curves have added to system unwieldiness. It is apparently because of such problems that these infrared hygrometers have not been widely used or accepted in the meteorological and cloud physics communities.

Recent advancements in the engineering technologies of extremely narrowband infrared filters, small stable non-cryogenic infrared detectors, low-noise and low-power operational amplifiers, wide band infrared beamsplitters, and vastly improved air-worthy analog and digital computers now make it possible to configure a stable, flight-qualified 20 centimeter path length hygrometer that will also respond to supersaturated vapor and reject hydrometeors in the instrument sample volume. Consider the instrument schematically drawn in Figure (1.4) where broadband collimated infrared radiation is passed through a 20 centimeter absorbing sample atmospheric path and split by a 50/50 beamsplitter into two equal intensity beams. The two received beams are then passed through narrowband filters at center wavelengths $[\lambda(1)]$ and $[\lambda(2)]$ and the filtered radiation falls on matched lead sulfide photoconductive cells to be perceived as received intensities $[I(1)]$ and $[I(2)]$.

Following Equation (1.4):

$$2 I_1/I_0 = \exp (- k_1 P_r^{B1}) \quad (1.6)$$

$$2 I_2/I_0 = \exp (- k_2 P_r^{B2}) \quad (1.7)$$

Eliminating $I(0)$ between these two equations

$$I_1/I_2 = \exp (k_2 P_r^{B2} - k_1 P_r^{B1}) \quad (1.8)$$

Choose $\lambda(1)$, to be 2.665 micrometers in the previously discussed intense water vapor absorption band and for simplicity let $\lambda(2)$ be a non-absorbing wavelength (i.e. 2.45 micrometers) so that $I(2)=1/2 I(0)$. Equation (1.8) then simplifies to:

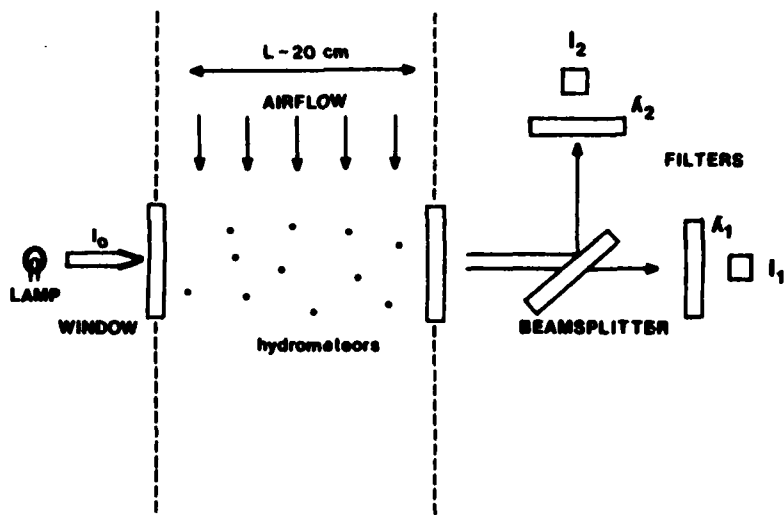


Fig. (1.4) Infrared Hygrometer Conceptual Diagram

$$I_1/I_2 = \exp (-k_1 p_r B_1) \quad (1.9)$$

Measurement of the ratiometric output $[I(1)/I(2)]$ then permits the calculation of absolute humidity independent of source intensity drifts and intervening scatterers and absorbers that do not exhibit wavelength dependent extinction between $\lambda(1)$ and $\lambda(2)$. Light source intensity changes, beam misalignment changes, dirty optics, and moving or stationary objects partially occluding the beam have no influence on the measurement. By thermoelectrically cooling the two lead sulfide detectors to a constant temperature of -30° Celsius, detector temperature drifts are also nulled out of the measurement.

1.3.3 Rejection of Hydrometeors in the Sample Volume

As discussed above, objects large enough to cast geometric shadows will obscure the beam in a wavelength-independent fashion and thus be rejected from the ratiometric measurement of $[I(1)/I(2)]$. When the beam sample volume contains micrometer sized Mie scatterers of sizes comparable to the wavelengths $[\lambda(1)]$ and $[\lambda(2)]$, then only first order wavelength independence is achieved and the particulate extinction at wavelengths $[\lambda(1)]$ and $[\lambda(2)]$ may be written (Chylek, 1978) as:

$$I_1/I_0 \mid \text{Particulate extinction} = \exp(-k_{p1}L) \quad (1.10)$$

$$I_2/I_0 \mid \text{Particulate extinction} = \exp(-k_{p2}L) \quad (1.11)$$

where the particulate extinction coefficient $[k_p(i)]$ is given as:

$$k_{pi} = \pi \int_0^{\infty} Q_{ext}(r, \lambda_i) r^2 n(r) dr \quad \text{for } i = 1, 2 \quad (1.12)$$

Note that the only wavelength dependence of the hydrometer extinction coefficient $[k_p(i)]$ resides in the Mie theory dimensionless extinction efficiency factor $[Q_{ext}(r, \lambda)]$. At sizes large compared to the wavelength Q_{ext} approaches 2.0 and in this geometric optics regime the particulate extinction coefficient is only the total of the projected cross-sectional areas of the particulates summed over their size distribution $n(r)$.

If we again eliminate $I(0)$ from Equations 1.10 and 1.11 to obtain the received intensity ratios then:

$$I_1/I_2 \mid \text{Particulate extinction} = \exp(-\Delta k_p L) \quad (1.13)$$

where:

$$\Delta k_p = \pi \int_0^{\infty} \{Q_{ext}(r, \lambda_1) - Q_{ext}(r, \lambda_2)\} r^2 n(r) dr \quad (1.14)$$

Calculation of the exact Mie extinction efficiency factor $[Q_{ext}(r, \lambda)]$ in the case of particulates having complex indices of refraction and thus acting as both radiation absorbers and radiation scatterers is discouragingly tedious (Stewart, 1977). Fortunately, Deirmendjian (1969) has provided an empirical approximation formula for $Q_{ext}(r, \lambda)$ valid within $\pm 5\%$ for spherical particles having complex indices of refraction $[M]$ where the refractive index is such that the real component is less than 1.5 and the imaginary absorption component is within the range of 0.0 to 0.25. His approximation is thus valid for water drops of any size in air at all infrared wavelengths and is given below as:

$$Q_{ext}(\rho, m) = (1 + d) \times_{ex} (\rho, m) \quad (1.15)$$

where:

$$\begin{aligned} \times_{ex}(\rho, m) &= 2 - 4 \cos g/\rho \exp(-\rho \tan g) \sin(\rho - g) \\ &+ 4(\cos g/\rho)^2 \{ \cos 2g - \exp(-\rho \tan g) \cos(\rho - 2g) \} \end{aligned} \quad (1.16)$$

$$\rho = 2x(v-1)$$

$$g = \arctan(\kappa/(v-1))$$

$$x = 2\pi r/\lambda$$

and:

$$d = \{(v-1)^2/1.632v\} \{f(g) + 1\} + \{0.2 \rho - v + 1\} / \{(v-1)f(g)\} \quad (1.17)$$

for $\rho < 5(v-1)$;

$$d = \{(v-1)/8.16v\} \{f(g) + 1\} \rho \quad \text{for } 5(v-1) \leq \rho \leq 4.08/(1 + 3(\tan g));$$

$$d = (v - 1) \{f(g) + 1\} / \{2 v(1 + 3 \tan g)\}$$

$$\text{for } 4.08 / \{1 + 3(\tan g)\} \leq \rho \leq 4.08 / \{1 + \tan g\};$$

$$d = 2.04(v - 1) \{f(g) + 1\} / \{v f(g) \rho\} \text{ for } \rho > 4.08 / \{1 + \tan g\};$$

$$\text{where: } f(g) = 1 + 4 \tan g + 3 \tan^2 g$$

At the vapor absorption peak at 2.665 micrometer, the complex index of refraction of water $M = 1.138 + 0.003449i$ while at the non-attenuating wavelength 2.45 micrometer we have $M = 1.270 + 0.001189i$ as tabulated by Irvine and Pollack (1968). Figure (1.5) illustrates the behavior of $Q_{ext}(r, 2.665)$, $Q_{ext}(r, 2.450)$, and $Q_{ext} = Q_{ext}(r, 2.665) - Q_{ext}(r, 2.450)$. At all wavelengths the measurement of differential

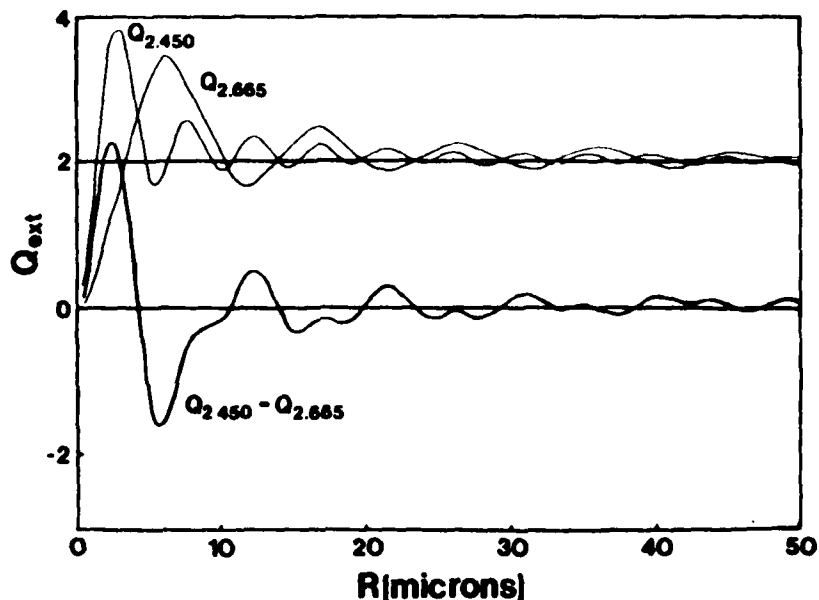


Fig. (1.5) Particulate Extinction Cross Sections

received radiation intensity significantly reduces the particulate error signal, Equation (1.13), over that of an unnormalized single beam attenuation instrument as, for example, described by Hyson and Hicks (1975). As shown in Figure (1.5) when $\Delta Q_{ext} = 0.0$, particles of that size will be perfectly rejected by the differential instrument and droplets larger than about 75 micrometers in radius will always be insignificant in contaminating the ratio of received light intensities. The largest error signal would be caused by a large number of monodisperse particles having a 3.5 micrometer radius. Since the ΔQ_{ext} curve oscillates above and below zero the particle size dependent differential extinction integrated over realistic and always

non-monodisperse atmospheric droplet distributions [$n(r)$] as in Equation (1.14) will cause the particulate error signal in $I(1)/I(2)$ to be dramatically reduced and to in fact approach zero for realistic size distributions [$n(r)$]. Thus particulates whose extinction is integrated over reasonably broad size distributions [$n(r)$] will be rejected by the differential instrument even though they may not be large with respect to the system wavelengths and may contribute significant total absorption at both wavelengths $\lambda(1)$ and $\lambda(2)$. This is in contrast to a single-ended measurement of transmission [$I/I(0)$] at a single wavelength [λ] where Q_{ext} approaches 2.0 and the particulate extinction does not vanish but is instead proportional to the total hydrometer projected cross-sectional area as per Equation (1.10), resulting in a larger contamination of the vapor absorption signal as the particulate concentration increases. Since the differential extinction efficiency difference of each particle ΔQ_{ext} must be multiplied by its geometric cross section to obtain the differential extinction due to that particle, the higher ΔQ_{ext} of small particles are compensated by their smaller size. Feedback mechanisms involved in condensation and coalescence growth of hydrometeors also inhibit the maintenance of large mass concentrations of monodisperse particles on the order of 3 micrometers in radius. As the number concentration of particles increases, they themselves cause the conditions that make them grow to larger sizes and broader size distributions where the ΔQ_{ext} attributable to their liquid water content becomes less significant. Also, the Mie scattering theory predicts that, for a given hydrometeor size distribution, the scatter will tend to become more efficient at shorter wavelengths. Thus the ratiometric measurement of $I(2.665)/I(2.450)$ in Equation (1.9) will tend to be increased by the presence of hydrometeor scatterers in the beam, leading to an underestimate of the absolute humidities and supersaturations. This conservative nature of possible second order system errors is a desirable property in an instrument designed to investigate anomalously high absolute humidities and supersaturations.

Before calculating a detailed aerosol extinction error from Equation (1.13), one can infer the effective rejection of hydrometeors in the sample volume by order of magnitude arguments. Pinnick et al. (1979) have tabulated the aerosol extinction coefficient [$k(p)$] of Equation (1.12) from a wide variety of in-cloud fog and haze measurements by different authors in different geographical locales and under many different meteorological conditions at a wide variety of wavelengths. In no case did a measured $k(p)$ exceed a value of 0.001 cm^{-1} . The aerosol extinction coefficient can be related to routinely observed meteorological range (Johnson, 1963) as:

$$V_r = 3.921/k_p \quad (1.18)$$

A $k(p)$ of 0.001 cm^{-1} thus corresponds to a visual range [$V(r)$] of 39.2 meters. This seems a realistic upper limit for $k(p)$ since, for example, the lowest range marker on the International Visibility Scale is 50 meters (Middleton, 1958). The values of $k(p) = 0.001 \text{ cm}^{-1}$ and $L = 20$ centimeters in Equation (1.10) yield a transmissivity, $T = 0.980$. From Figure (1.5), it seems reasonable, by inspection, to expect a twentyfold reduction in the $\Delta k(p)$ of Equation (1.14) over the single ended value of

$k(p)$ as used in Equation (1.10). This would indicate that the ratio of received intensities [$I(1)/I(2)$] will always be greater than 0.999 in realistic worst case hydrometeor interference conditions at the two wavelengths chosen and a 20 centimeter pathlength. The minimum estimated 20 fold reduction in $\Delta k(p)$ is supported by inspection of extensive tabulations of $k(p)$ as calculated by Tampieri and Tomasi (1976) for many different wavelengths and droplet size distributions. Their 'worst' size distribution is a modified gamma size distribution with modal radius at 3.0 micrometers and a very low skewness and standard deviation. Inserting that stratocumulus size distribution in Equation (1.13) with $\lambda(1) = 2.665$, $\lambda(2) = 2.450$, $L = 20$ centimeters indicates a worst case differential particulate extinction error of less than 0.01% of reading for this particular configuration. Under most conceivable cloud conditions, we can expect the rejection of liquid hydrometeors to be very much greater than this. A similar analysis has been performed for ice hydrometeors and indicates even greater rejection of ice particles in the beam, mainly due to the intrinsically much larger sizes of ice crystals (>10 micrometers) in normal atmospheric conditions. Such hydrometeor rejection ratios are, of course, only achievable in a very narrow and intense water vapor absorption band that permits sample path lengths on the order of 20 centimeters.

1.3.4 Measuring Supersaturated Vapor

The validity of Equation (1.5), permitting the measurement of absolute humidity by means of the instrument schematically shown in Figure (1.4) depends on the tacit assumption that the given effective vapor absorption coefficient depends only on absolute humidity (grams per cubic meter) and the second order influence of ambient pressure and temperature. If this coefficient were to also change markedly as a function of saturation ratio, then the utility of the instrument in measuring supersaturated vapor would be compromised. Vyaltseva *et al.* (1967) found their infrared humidity sensor gave readings too large at relative humidities greater than 90% and attributed this to the formation of complexes and aggregations of water vapor molecules which caused added infrared attenuation in their 2.58 micrometer wavelength channel. Apparently no other authors have reported such an effect. Theoretical estimates of the mole fraction of water substance involved in dimer and polymer cluster aggregates (Owicki *et al.*, 1975; Hale and Plummer, 1974; Carlon, 1978; and Carlon, 1979) indicate that the total mass fraction [F] of water vapor molecules bound into clusters of any size greater than the monomer is a linear function of saturation ratio [S]. For example, at 293° Kelvin the relationship is:

$$F = 0.00006 S \quad (1.19)$$

It is thus quite conservative to assert that the total mole fraction of water clusters of all sizes in the free atmosphere never exceeds 0.0001. This conclusion is supported by the experimental data of Lin (1973) and Searey and Fen (1974). Furthermore, the effect of cluster formation will be to inhibit absorption at the 2.6 micrometer

band by constraining interatomic resonances while cluster intermolecular resonances appear as continuum absorption at much larger wavelengths (Suck *et al.*, 1979). For example, dimer resonance occurs at about 9 micrometers and trimer resonance peaks near 11 micrometer (Carlon, 1979b). Water cluster formation would thus seem to not only have a negligible effect on vapor absorption in the 2.6 micrometer band, but the effect should be of opposite sign to that postulated by Vyaltseva, *et al.* (1967) to explain their experimental results. Their anomalous results are much more readily explained by differential water adsorption on surfaces in their instrument which used two different beam paths and thus was not truly ratiometric. For example, Howard (1963) has discussed the disturbing influence of wall adsorption of water vapor on infrared measurements. Also many common infrared window materials such as sodium chloride, potassium bromide, potassium chloride, thallium bromide, cesium iodide, lithium fluoride, and potassium iodide are hygroscopic at high humidities and could have caused the effect if used as their unspecified windows and lenses. There appears to be no theoretical reason to expect the measured received intensity ratio $[I(1)/I(2)]$ of the instrument proposed here to be affected by relative humidity or saturation ratio.

1.4 Passive 4.3 micrometer Carbon Dioxide Band Air Temperature Radiometry

Previous sections of this report have disclosed a non-contact technique whereby concurrent measurements of the ratio $[I(1)/I(2)]$, and $t(a)$ and $p(a)$ (as second order effects) enable a very accurate measurement of absolute humidity even in the presence of interfering hydrometeors and at saturation ratios with respect to ice or water substantially in excess of one. However, the parameter of more direct interest in many meteorological and cloud physics applications is relative humidity or supersaturation ratio, the calculation of which requires a simultaneous measurement of ambient temperature $[t(a)]$. In clear subsaturated conditions any accurate temperature sensor will suffice. In saturated or possibly subsaturated but still cloudy conditions, provisions must be made to prevent cloud drops from wetting the temperature sensor as is done in standard airborne reverse flow temperature sensors. In supersaturated vapor, the situation is much more difficult. Consider for a moment an airborne humidity sensing system consisting of wet and dry bulb thermometers exposed to ambient airflow and having similar thermal mass. As the saturation ratio exceeds 1.0, condensation will occur on both which then act as matched wet bulbs and are elevated in temperature above true ambient temperature by the latent heat of condensation upon them. A calculation of relative humidity from these measurements would thus indicate 100% relative humidity at a falsely elevated temperature rather than the true situation, supersaturation at a lower ambient temperature. If absolute humidity measured in supersaturated conditions is to be converted to saturation ratios in excess of 1.0, then the concurrent temperature measurement must also operate without contact and meet the same criteria set forth in Section (2) for the absolute humidity sensor. Sonic thermometry and passive infrared thermometry are both non-contact techniques that could possibly meet these requirements. Sonic techniques would not seem practical in an airborne environment since aircraft speeds are a significant fraction of the speed of sound, leading to large cosine

errors (Kaimal and Businger, 1963). High vibration, high sound levels, air turbulence, and aircraft induced pressure changes are also complicating factors causing transducer response errors. A further complication is caused by the speed of sound in air being a function of virtual rather than actual temperature. In fact, Low (1967) has discussed the possibility of using an acoustic virtual temperature measurement in combination with an (unspecified) actual temperature measurement to calculate sub- and supersaturation ratios.

Passive radiometry would seem a much more suitable airborne non-contact temperature measuring technique. Consider a monochromatic passive infrared sensor looking into a uniform medium which has significant absorption at its wavelength $[\lambda]$. The radiance $[N(\lambda)]$ received by the sensor will be related to the gaseous absorber temperature by Planck's law. Since Kirchoff's Law of local thermodynamic equilibrium applies in the free atmosphere we may equate emissivity and absorptivity at any given wavelength $[\lambda]$. Then the received radiance at the sensor will be given as:

$$N(\lambda) = P(\lambda, t_e) \int^{\infty} \partial \tau(\lambda) / \partial \lambda d\lambda \quad (1.20)$$

where $P(\lambda, t(a))$ is the Plank Law Relation:

$$P(\lambda, t_e) = 2\pi c^2 h \lambda^{-5} \{ \exp(hc/\lambda k_b t_e) - 1.0 \}^{-1} \quad (1.21)$$

c = the velocity of light, 2.9979×10^10 cm/sec

h = the electron charge, 6.626×10^{-27} erg.sec

k = Boltzmann's constant, 1.3806×10^{-16} ergs per $^{\circ}$ Kelvin

$t(e)$ = emitter temperature, $^{\circ}$ Kelvin

and where $\tau(\lambda)$ represents the transmittance of the material in the path length $[L]$ as measured from the detector. Thus in the case of a gaseous emitter and a narrowband but non-monochromatic receiver we have by analogy to Equation (1.4):

$$\tau(\Delta\lambda) = \exp(-k_{\Delta\lambda} \lambda^B) \quad (1.22)$$

Since the gas is absorbing at wavelength band $\Delta\lambda$, for sufficiently large λ we have:

$$\int_0^{\infty} \partial \tau(\Delta\lambda) / \partial \lambda d\lambda \rightarrow 1.0; \lambda \rightarrow \infty \quad (1.23)$$

So for sufficiently large sample path $[L]$, Equation (1.19) reduces to:

$$N(\lambda) = P(\lambda, T) \quad (1.24)$$

Thus the sensor response can be directly related to absorber (air) temperature and the effect of various absorber concentrations and degrees of opaqueness only influence the sample volume over which the gaseous absorber temperature is averaged. The weighting function for this spatial average of temperature is just $d\tau(\lambda)/dL$, and for any path of sufficiently long length $[L]$, the effective emissivity of the gas is 1.0. Infrared gaseous temperature measurements are thus exact and not dependent

on grey body emissivity approximations.

This derivation of passive infrared temperature measurement and sample volume considerations has been cursory; a much more rigorous and detailed derivation can be found in Chapter 17 of the book by Eckert and Drake (1972).

The measurement of air temperature via Equation (1.24) requires that an atmospheric strongly absorbing wavelength band be selected such that Equation (1.23) holds and the gas become 'black' over a reasonable path length [L]. The absorbing component should also be a relatively constant constituent of the atmosphere to minimize temperature sample volume changes due to absorber concentration changes.

Figure (1.6) illustrates the regions of absorption of the common infrared-active trace gases. Only carbon dioxide with an atmospheric abundance of 0.033% by volume qualifies as a constant mixing ratio stable trace gas. With the exception of water vapor it is also the most molecularly abundant atmospheric infrared absorbing trace gas. From Figure

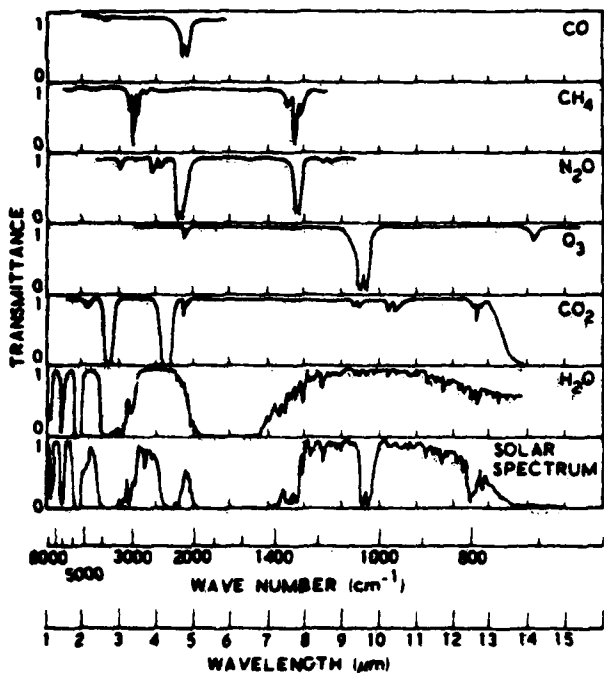


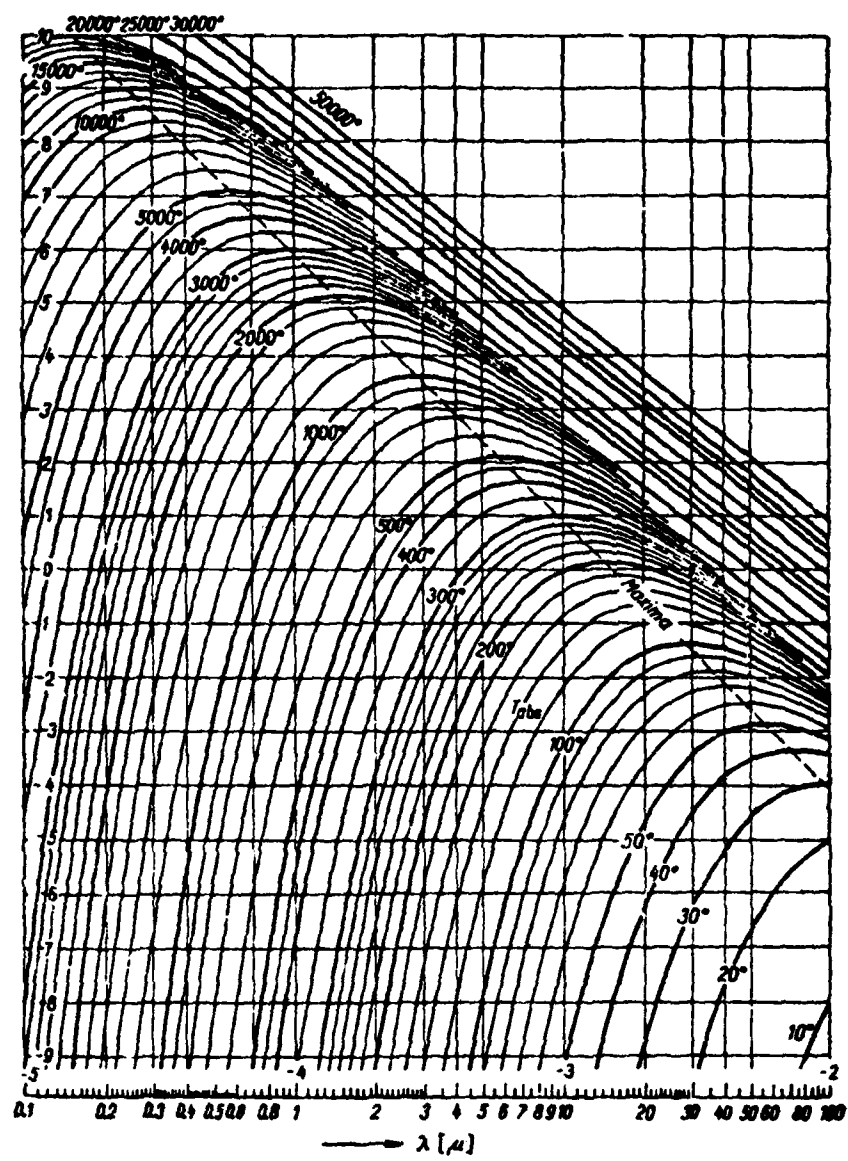
Fig. (1.6) Atmospheric Trace Gas Infrared Absorption

(1.6) it can be seen that carbon dioxide has strong absorption bands at about 2.75, 4.25, and at 14 - 16 micrometers. Inspection of the Planck's

Law radiance curves of Figure (1.7) reveals that the thermal atmospheric reradiation in the 2.75 micrometer band at tropospheric temperatures of 225 - 300° Kelvin will be two to four orders of magnitude less than in the 4.25 and 14 - 16 micrometer bands. The choice is thus from selected wavelengths in the carbon dioxide 4.25 and 14 - 16 micrometer absorption bands. Figure (1.8) shows the same black body radiance Planck's law curve as Figure (1.7) but for a temperature of 0° Celsius and plotted on a linear scale. At tropospheric temperatures the carbon dioxide 14 - 16 micrometer band falls on the long wavelength side of the spectral Wein's Law peak and the 4.3 micrometer band radiates at the short wavelength side of the peak. At 0° Celsius, the thermal reradiation from the 14 - 16 micrometer band is about six times as intense as that from the 4.3 micrometer band. Figure (1.9) illustrates the relative intensity of black body atmospheric radiance from a thick isothermal gas layer as a function of gas temperature at the 4.255 and 14.3 micrometer bands. The 4.3 micrometer radiance is on the order of tenfold lower than the 14.3 micrometer radiance throughout the tropospheric temperature range. It is apparently for this reason, higher radiance at wavelengths closer to the Wein's Law peak, that all past carbon dioxide band air temperature radiometers of which we are aware have chosen to utilize the 14 - 16 micrometer long wavelength absorption band.

1.4.1 Previous 14.3 Micrometer Band Radiometers

The first serious attempt to measure free air temperature via passive 14 - 16 micrometer band carbon dioxide radiance was apparently the Barnes Engineering Company Model No. 14-202 Free Air Thermometer developed in the early 60's with support from the Air Force Geophysics Laboratory and the U. S. Army Electronic Research and Development Laboratory. The device was on the leading edge of then contemporary technology and used a germanium immersed thermistor bolometer detector, germanium optics, and a filter bandpass of 14.3 - 16.3 micrometers. According to Astheimer (1962) the effective sample volume was a field of view 40° horizontally by 10° vertically and between 200 and 4,000 feet long. Neither Barnes or any other company of which the authors are aware currently manufacture a carbon dioxide band air temperature thermometer, probably because in situ temperature weighted over such an immense non-isothermal volume loses its operational utility. Commercial equipment has, however, been adapted for this use by the scientific community. For example, Albrecht et al. (1979) have recently reported on a series of airborne non-contact infrared temperature measurements using a moderately narrow band thermistor bolometer sensor at 14.8 micrometers and inverting temperature by means of Equation (1.23). They found that temperature variations of less than 0.05° Celsius could easily be resolved. Their effective sample path length was on the order of 30 - 100 meters depending on vapor concentrations and hydrometeor content. Contributions to 14.8 micrometer emission by both vapor and particulates caused their measured temperature to be weighted in an unknown fashion between vapor temperature and hydrometer temperature and also cause significant sample volume variations as a function of both cloudiness and humidity. Their 14.8 micrometer wavelength was apparently chosen since it corresponds to the peak Planckian emission of substances at tropospheric temperatures. Platt (1976) using a filtered sensor in the atmospheric 10 - 12 micrometer window found that the



Nomogram of the monochromatic radiance L_{01} of a perfect black body in double logarithmic scales, applying to non-polarized radiation. $\log \lambda$ (cm) has been plotted on the

axis of abscissae, $\log L_{01} \left[\frac{W}{cm^3 \text{ sterad}} \right]$ on the axis of ordinates.

Wavelengths [μ] are indicated on the lower scale. The dashed line indicates the position of the peaks of the radiation

Fig. (1.7) Black Body Spectral Radiance Curves

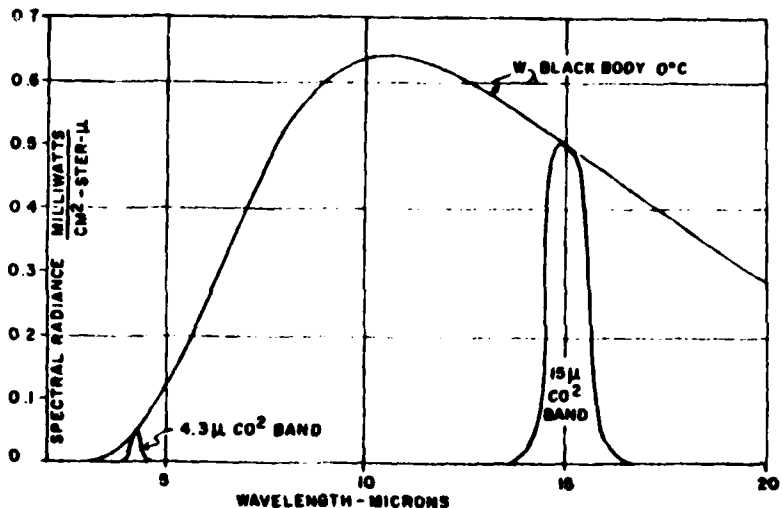


Fig. (1.8) Spectral Radiance in the Carbon Dioxide Bands

hydrometeors in typical stratocumulus clouds cause them to become 'black' in a sample depth of 100 - 400 meters, so the data of Albrecht et al. (1979) seems to be about equally weighted by air temperature and in-cloud hydrometer temperature. Uncontaminated in-cloud air temperature measurements via passive radiometry will require a much more intense absorption band that effectively turns 'black' in a much smaller distance than do in cloud hydrometeor distributions. Therefore, it is believed this smaller effective temperature sample volume can be achieved by operating in the strongly absorbing 4.255 micrometer carbon dioxide band.

1.4.2 The Proposed 4.255 Micrometer Band Air Temperature Radiometer

Wyatt et al., (1962) provide data at the carbon dioxide 4.255 micrometer absorption peak at a filter band pass wavenumber of 50 cm⁻¹. Assuming a constant 0.033% carbon dioxide content by volume for the free atmosphere, then the above data can be fit by a relation analogous to Equation (1.4) as:

$$(I/I_0)_{CO_2} = \exp(-KL^B) \quad (1.25)$$

where:

K (carbon dioxide, 4.255 micrometers, 300° Kelvin, 1 atmosphere, 50 cm⁻¹ wave number) = 0.0351726

B (carbon dioxide, 4.255 micrometers, 300° Kelvin, 1 atmosphere, = 0.64238

Figure (1.10) shows this 4.255 micrometer carbon dioxide transmission

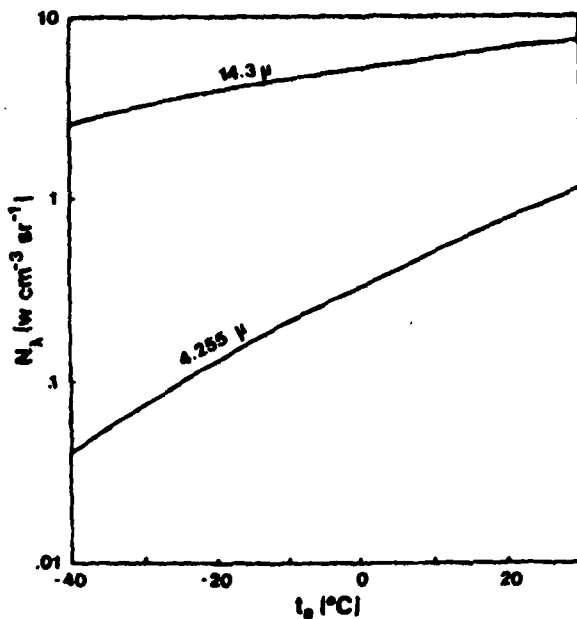


Fig. (1.9) Carbon Dioxide Band Emission versus Temperature

ratio as a function of path length [L]. Substitution of Equation (1.24) in Equation (1.14) indicates that one can interpret T in Figure (1.10) as the fractional contribution to the temperature spatial weighting function coming from distances greater than L. Thus one-half of the temperature average comes from distances [L] less than one meter from the sensor and the effective sample volume is consistent with the sampling length of 20 centimeters for the proposed absolute humidity sensor, is much smaller than that attainable by 10 to 14 micrometer wavelength band sensors, and goes to 'blackness' much more rapidly than cloud hydrometeor distributions.

Figure (1.9) shows the monochromatic radiance received at a sensor from a thick isothermal gas layer as a function of gas layer temperature at 4.255 and 14.3 micrometers as calculated from Equation (1.23). Although the 4.255 micrometer channel has a lower received radiance it is also a much stronger function of temperature. Further, lead selenide (PbSe) detectors having a peak detectivity at 4.255 micrometers are about 200 times more responsive (volts/incident watt) than thermistor bolometers as used by Albrecht *et al.* (1979) at 14.3 micrometers as shown by Wollman (1979). This more than compensates for the lower Plank's Law radiance of the 4.25 micrometer channel.

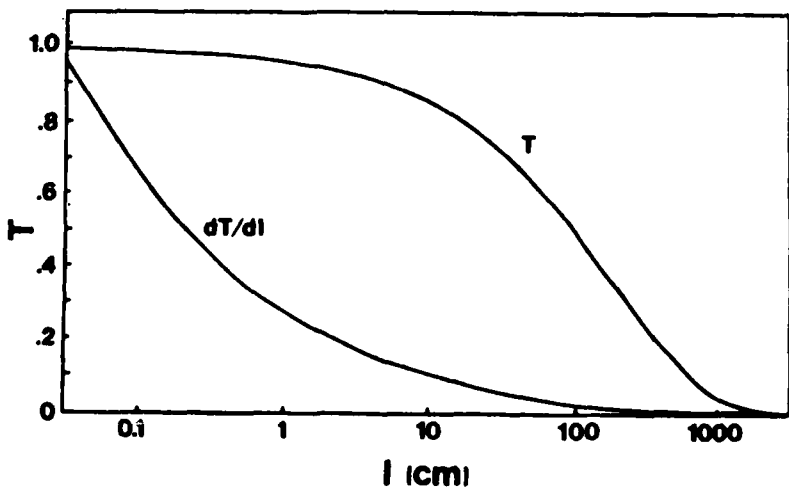


Fig. (1.10) Radiometer Spatial Weighting Function

At 4.255 micrometer, a 0.1 micrometer bandpass and a 1 steradian field of view, a 1 millimeter square lead selenide detector will intercept about 0.1 microwatt of thermal radiation from a gas at 30° Celsius and about 0.005 microwatt at -40° Celsius. At a responsivity of $1 E + 5$ volt/watt, voltage signal output should range from 0.5 to 10 millivolts over this temperature range. This is a higher signal level, for example, than that attained by a conventional type 'K' thermocouple. Only moderate optical gain is thus required to make an effective small sample volume passive infrared temperature sensor in the 4.255 micrometer carbon dioxide absorption band. Since the Lead Selenide detector is spectrally selective and does not respond to photons having wavelengths longer than about 5 micrometers, stray thermal radiation from longer wavelength near the Wein's Law thermal peak does not deteriorate the signal as would be the case if a non-wavelength selective (i.e., thermopile or thermistor bolometer) sensor were used. This point will be discussed in more detail in Section (4.1.5).

Since the temperature weighting of substances in the detector field of view is proportional to their absorptivity, relatively optically thin or transparent substances at 4.255 micrometer wavelength such as sensor windows and cloud hydrometeors contribute only negligibly to the temperature measurement. The measured radiance is thus a measure of true air (i.e., carbon dioxide) temperature independent of hydrometeor content or particulate temperature since atmospheric carbon dioxide is much more absorptive at this wavelength than any conceivable cloud.

1.5 Supersaturation Derived from Absolute Humidity and Air Temperature

Concurrent non-contact measurements of absolute humidity [$\rho(a)$] from Equation (1.5) and true air temperature [$t(a)$] from Equation (1.24), enable calculations of saturation ratios with respect to either ice or water regardless of hydrometeor content or supersaturation in the sample volume. The saturation ratio [S] is calculated as:

$$S = \rho(a) / \rho(\text{sat}) \quad (1.26)$$

where the currently accepted saturation vapor densities of water vapor [$\rho(\text{sat})$] with respect to liquid and ice are tabulated as functions of ambient temperature [$t(a)$] by List (1963) and can be readily calculated by, for example, the empirical Goff-Gratch Formulation as given in the same reference. A more contemporary and accurate formulation of the temperature dependence of water vapor density at saturation is given by Wexler and Greenspan (1971).

Thus, a measurement of the transmission ratio [$I(1)/I(2)$] of the 2.665 and 2.45 micrometer radiation over a short (nominally 20 centimeters) path, a concurrent passive atmospheric measure of radiance at the 4.225 micrometer carbon dioxide absorption band, and a crude estimate of atmospheric pressure enables the calculation of:

- (a) absolute humidity (grams per cubic meter)
- (b) true air temperature ($^{\circ}$ Celsius)
- (c) saturation ratio with respect to ice
- (d) saturation ratio with respect to water

All of the above derived quantities remain theoretically valid regardless of adiabatic heating at high aircraft speeds, hydrometeors in the sample volume, and possible vapor supersaturations with respect to both water and ice.

2 INSTRUMENT DESIGN

2.1 Introduction

Section (1.0) above has reviewed the theoretical basis for making the first accurate measurements of temperature and humidity conditions in cloudy supersaturated environments. In this section, a functional description of a prototype electro-optical instrument to evaluate this technology will be presented. The supersaturation sensor consists of two essentially independent subsystems; an absolute humidity sensor and a true air temperature sensor.

2.2 Functional Block Diagram

A functional block diagram illustrating the operation and interrelation of the two supersaturation sensor subsystems is given in Figure (2.1). A light beam from a broad band source such as a quartz

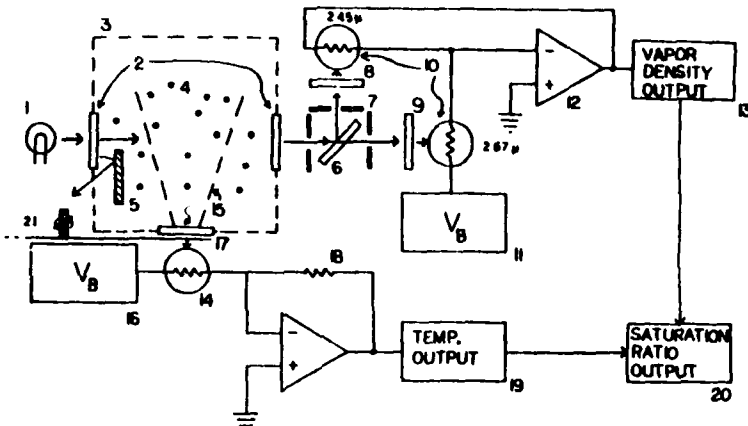


Fig. (2.1) Supersaturation Sensor Block Diagram

halogen tungsten filament lamp (1) is transmitted through a heated transparent window system (2) into a sample volume (3) which contains the gaseous admixture of water vapor in air and possible particulate hydrometeors (4). Possible changes in the intensity of the incident beam due to source intensity drifts, beam misalignment, dirt on optics and solid bodies partially occultating the beam are represented schematically as a solid beam occultating body (5). After having passed through the sample volume (3) over a path length of about 20 centimeters, the broad band light beam is split into two parts by the beam splitter (6). A narrow band interference filter at 2.67 micrometers (8) isolates the strongly absorbing water vapor absorption band. An unabsorbed reference wavelength at 2.45 micrometers is selectively transmitted by a second narrow band interference filter (9).

The received light intensity in these two narrow wavelength bands passed by the two bandpass filters (8) and (9) impinges on a matched pair of thermoelectrically cooled photoconductive lead sulfide detectors (10). By means of a bias voltage (11) applied to the photoconductor pair configured as load and feedback resistors of an operational amplifier (12), an output voltage (13) proportional to the ratio of the received intensities $[I(1)/I(2)]$ from Equation (1.9) as sensed by the photoconductors is generated. The beam attenuation at the two wavelengths due to water vapor is in each case determined by the Beer-Lambert

absorption law as corrected for instrumental deviations and finite filter bandpasses.

Since non-wavelength-dependent attenuating causes such as particulates in the beam, source intensity drifts, beam misalignment, and partial occultation result in equal changes in the intensity sensed by the two matched receiving photoconductors (10), these effects do not appear at the ratiometric output (13), which senses only wavelength dependent attenuation between the two narrow band received beam intensities. Since vapor, liquid, and gaseous absorption peaks of water vapor occur at different wavelengths; choice of these filter bandpasses to assure high differential water vapor absorption and low differential liquid water and ice absorption results in high order rejection of the liquid and solid phases. A system of baffles (7) assures that the detectors view only the direct collimated rays from the light source (1). The output signal (13), however subsequently conditioned, is a direct monotonic measure of water vapor concentration (grams per cubic meter) in the sample volume regardless of hydrometeors or supersaturated conditions in the sample volume. In this proof of concept laboratory prototype, the output signal (13) will be the transmissivity, $T = I(1)/I(2)$ from Equation (1.9). Signal conditioning via Equation (1.4) will be done manually rather than implemented in hardware or microprocessor software.

Further processing of the ratiometric output via logarithmic converters, power law expansions, conversion from transmittance to absorbance, system linearizing functions, conversion to absolute humidity via Equation (1.4), and the like can be readily implemented once the basic device theory has been proven by a laboratory prototype and calibration program.

A substantially concurrent measurement of gas temperature is achieved by a passive radiometric sensor which is implemented by a lead selenide photoconductor (14) having a field of view (15) and filtered by a narrow band 4.255 micrometer filter (17) whose bandpass wavelength has been selected to be in a strong absorption band of carbon dioxide, a relatively constant atmospheric constituent with an abundance of approximately 330 parts per million by volume. A maximization of the intensity of carbon dioxide absorption by selection of the wavelength interval to encompass the strongest absorption band minimizes the effective sample volume to be commensurate with the active sample volume (3) of the absolute humidity sensor. Changes in pressure or carbon dioxide content of the atmosphere affect only the volumetric temperature spatial weighting function Equation (1.19), while true air temperature is exactly given by the black-body Planckian emission law at the selected filtered wavelength. Since temperature weighting of the sensor is inversely proportional to the sampled substance absorptivity at the sampled wavelength, other materials in the sample volume such as liquid water aerosols having small optical density at 4.225 micrometers contribute only negligibly to the temperature measurement.

A true measure of gas temperature independent of hydrometeor content thus results. Since the measurement of temperature is non-contact and the filter window (17) can be heated to prevent condensation, true gas temperature readings can be taken in particulate laden supersaturated

condensing conditions. In this embodiment the signal from the Lead Selenide temperature sensing element (14) is conditioned by a bias voltage (16) and a feedback resistor (18) in the feedback loop of an operational amplifier (15) to produce a signal proportional to the narrow band passive irradiance received on the sensor (14) and thus by the Planckian emission law, proportional to the air temperature.

Since the instrument housing and the atmospheric sample volume are of roughly comparable temperatures, they both contribute significantly to the thermal emission received by the Lead Selenide sensor (14). A rotating chopper wheel (21) periodically interrupts the atmospheric irradiance signal, resulting in an AC signal component (the atmospheric temperature irradiance signal as per Equation (1.19)) which is synchronously demodulated by a phase reference signal derived from the chopper wheel rotation rate and scaled via a temperature-irradiance conversion according to the Wein's Law approximation to Equation (1.21). The result is a direct readout (19) of the true air temperature. Details of this demodulation and scaling process and second order effects such as thermal emission from the chopper wheel are given in Section (4.0).

Having in this way achieved a substantially concurrent measure of absolute humidity (grams per cubic meter) from (13) and true air temperature from (19), a synergistic combination of these two quantities (20) results in a measurement of saturation ratio that remains valid in supersaturation conditions and in hydrometeor-laden atmospheres. Calculation of saturation ratio from absolute humidity and air temperature is well known and can be accomplished by tabular means such as for example, the Smithsonian Meteorological Tables or by analytical or empirical formulas such as for example, the Goff-Gratch Formulation as discussed in Section (1.5). The saturation ratio calculation can either be accomplished in a post-processing mode by manual or computer aided calculation as proposed for this prototype instrument or in quasi-real time by analog or digital processing techniques.

As a design goal, we will attempt to measure the transmissivity, $T = I(1)/I(2)$, from Equation (1.9) to an accuracy of 0.1% or 1 part per thousand. From Equation (1.5) we can readily translate this design goal to a percentage absolute humidity error as a function of the vapor density in a fixed (i.e. 20 centimeter) path length. This conversion is presented in Figure (2.2) where the percent absolute humidity error caused by a 0.1% transmissivity error in a 20 centimeter path length is plotted against the log of absolute humidity. It can be seen that a 20 centimeter path minimizes the absolute humidity error (0.4% of reading, not full scale) at laboratory temperatures for our prototype evaluation. The error remains remarkably small over a dynamic range of 3 to 4 orders of magnitude and is minimized when the measured transmissivity is about 0.5 (see Figure 1.2). The absolute humidity error minimum can thus be easily moved to lower vapor densities by simply changing the path length [L] to slightly larger values, as would be the case in an instrument optimized for high altitude measurements. The design goal thus translates to an absolute humidity accuracy of 1% of reading or better over a dynamic range of about 4 orders of magnitude.

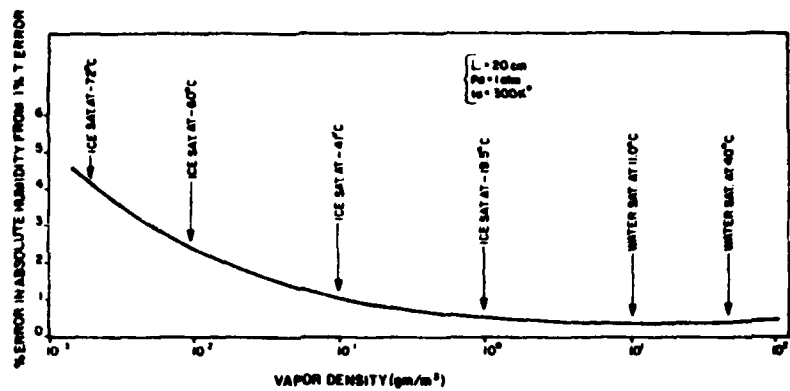


Fig. (2.2) Transmissometer Error Propagation

If we are to retain this inherent accuracy in the calculation of relative humidity using the measurement of true air temperature, then we must seek to measure air temperature to a similar resolution. Figure (2.3) shows the relative humidity error introduced by a 0.1° Celsius error in the

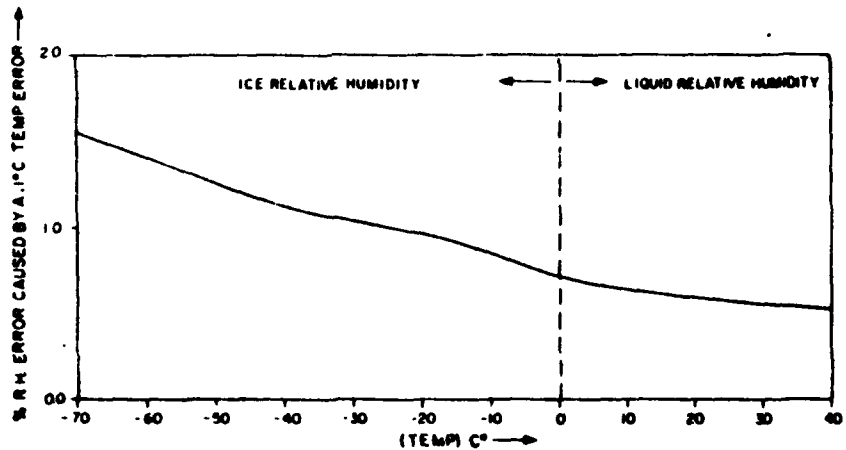


Fig. (2.3) Air Temperature Error Propagation

measurement of air temperature.

From Figures (2.2) and (2.3) it can be seen that an air temperature design goal accuracy of $\pm 0.1^\circ$ Celsius is commensurate with the design goal of 0.5% accuracy in absolute humidity and would permit the calculation of relative humidity and saturation ratios to an accuracy of better than 1% over a dynamic range of about 76° Celsius in temperature and about three orders of magnitude in absolute humidity.

Achieving a radiometric temperature accuracy of $\pm 0.1^\circ$ Celsius will be a difficult task. Albrecht *et al.*, (1979) report an airborne in-cloud system temperature resolution of better than ($\pm 0.05^\circ$ Celsius) using a 14.8 micrometer bandpass filter and a thermistor bolometer sensor. A thermoelectrically cooled Lead Selenide sensor at 4.25 micrometer theoretically has detectivity (D^*) about two orders of magnitude higher than a thermistor bolometer while the black body radiance at 4.25 micrometers is only about 1 order of magnitude lower than at 14.3 micrometers. Therefore, it can be theoretically expected to better their system temperature resolution. Absolute accuracies of $\pm 0.1^\circ$ Celsius will be difficult to achieve and will require very careful nulling of instrument thermal self emissions and offset drifts. The best commercial low temperature surface radiometers claim absolute accuracies of about $\pm 0.3^\circ$ Celsius, but do not have the gas sensing luxury of being able to assume a surface emissivity of exactly 1.000. It would, however, seem likely that $\pm 0.1^\circ$ Celsius absolute accuracy in a gas temperature radiometer is at the extreme edge of the state of the art and that air temperature measurement accuracy rather than absolute humidity sensor errors will be the limiting factor in the accuracy of saturation ratios from the data of the proposed supersaturation sensing system.

The following Sections (3) and (4) will discuss the detailed component-level design of the optical, electronic, and mechanical systems by which it is intended to fabricate the evaluation prototype of the absolute humidity and radiometric air temperature subsystems of the supersaturation sensor shown schematically in Figure (2.1). In these sections that follow, it may be helpful to the reader to refer back from time to time to Figure (2.1) to see the relation of each particular component to the system as a whole.

3 ABSOLUTE HUMIDITY SENSOR

3.1 Optical Design

3.1.1 Window Materials

System windows will be optical grade highly polished single crystal artificial sapphire provided by Crystal Systems, Inc. Sapphire has a number of unique physical, mechanical, and chemical properties that make it invaluable in this application. It is hydrophobic, non-hygroscopic, has zero porosity, is insoluble in water below 1000° Celsius, is the third hardest substance following only diamond and boron nitrate, is chemically inert, has excellent rain erosion resistance, a very high mechanical strength and is optically stable under high illumination.

levels. It has high optical transmission in the infrared and low refractive index and Fresnel reflection losses. It is an excellent electrical insulator with a thermal conductivity one-half that of iron and low thermal expansion thus facilitating the heating of system windows and is also surprisingly cost-effective. Contrast this material to the magnesium fluoride or lithium fluoride windows required in the Lyman-Alpha device to achieve optical transmission in the far ultraviolet. Such windows are slightly hygroscopic, slightly soluble in water, degenerate with time in the atmosphere, adsorb water at high relative humidity, are mechanically soft, and have a transmissivity that degenerates with time upon exposure to ultraviolet radiation (Tillman, 1965). This latter deficiency is especially serious since lack of stable far ultraviolet narrow-band filters (to be discussed later) prevents the Lyman-Alpha device from nulling out source intensity drifts via differential techniques as proposed here in this infrared sensor.

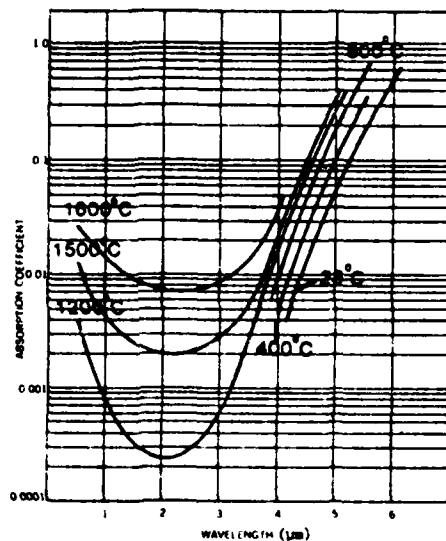


Fig. (3.1) Absorption Coefficient of Sapphire

Figure (3.1) shows the absorption coefficient of sapphire as a function of wavelength and temperature. From the data of Figure (3.1) and the Beer-Lambert Absorption Law (Equation 1.1), it can be seen that a 3 millimeter thick sapphire window can be heated to 1200° Celsius and still have an emissivity of only 0.0001 at 2.67 micrometers. At 4.25 micrometers, a 1 millimeter thick filter at the melting point of solder (400° Celsius) will have an emissivity of only 0.001. Thus, sapphire windows can be heated to remove water and ice from cloud penetrations

without causing window thermal emission or absorption to interfere with the optical measurements at either 2.67 or 4.25 micrometers. This feature is significant since an airborne version of the prototype device must be concerned with possible condensation on system windows. There is, however, another effect to consider. Any substance with a refractive index not equal to 1.0 will suffer surface reflection losses according to the Fresnel relations. At normal incidence, the single surface reflectivity (r) will be given by:

$$r = (n-1)^2 / (n+1)^2 \quad (3.1)$$

where n is the refractive index of the window. The reflection loss of a normal parallel beam due to a two-surface window is then:

$$r_2 = 1 - (1-r)^2 \quad (3.2)$$

Compared to other infrared transmitting substances the refractive index of sapphire is quite low (1.66371 at 4.255 micrometers) and thus Fresnel reflection losses are small. Normal 2-surface window reflectivity will be only 0.140. This can be neglected as a constant offset in the two-wavelength absolute humidity sensor.

In the 4.25 micrometer temperature sensor, it causes both a constant offset in the atmospheric irradiance through the window and a 14% contamination of the atmospheric signal via reverse reflection of the thermal emissions of the instrument housing. Methods for removing this error source will be dealt with in detail in Section (4). The important point is that all of these effects are constant offsets independent of the sapphire window temperature.

3.1.2 Light Source

The light source will be a quartz halogen tungsten filament lamp operated at less than its rated voltage to increase the lamp life and move the light emission peak towards the infrared. Precedent for successful use of such a light source in an infrared hygrometer at 2.7 micrometers can be found in Hysor and Hicks (1975). A principal requirement is that the light source be broad-band, wavelength selection being made later by the narrow-band infrared filters (8 and 9). This is directly opposite to the Lyman-Alpha Humidiometer where the light source is the narrow spectral Lyman-Alpha line at 1215.6 Angstrom and the windows pass a broad ultraviolet spectrum.

Since the bandpass filters (8 and 9) are quite narrow (about 0.01 micrometer) to permit a bandpass entirely within the most intense water vapor absorption band, much of the light source output does not reach the Lead Sulfide sensors and a quite intense broadband light source is required. It is intended to use an Osram Model 64635 tungsten halogen infrared reflector lamp (150 watts, 15 VDC) as the absolute humidity sensor light source. About 80% of the lamp output is concentrated by an integral front surface ellipsoidal gold reflector to a focus 19 millimeters in front of the reflector opening as shown in Figure (3.2).

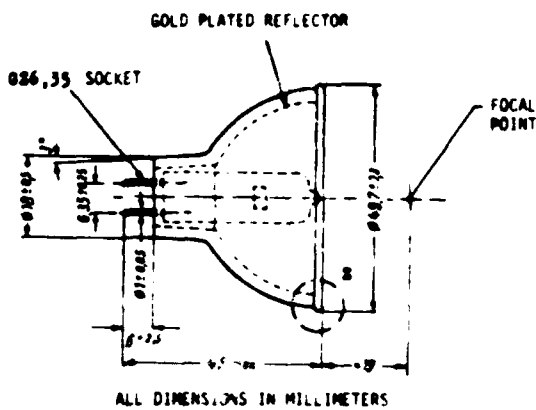


Fig. (3.2) Absolute Humidity Sensor Light Source

One additional optical element (described in Section 3.13) can thus put about 120 watts of optical power in a parallel beam of 1 inch diameter. Since the system operates at 2.67 micrometers, and glass and quartz have an O-H radical absorption peak at about 2.75 micrometers, an investigation of the absorption behavior of the lamp's quartz envelope seems prudent. Most halogen lamp manufacturers have no data on the infrared absorption behavior of these quartz envelopes. While specially processed water free (infrared grade) quartz can eliminate the 2.75 micrometer absorption band, we will assume that ordinary quartz (Vitrosil or Spectrosil) is used in the lamp envelope. The best data on the infrared absorption of quartz (fused silica) is given by Edwards (1966). Figure (3.3) shows the expected absorption coefficient of ordinary quartz (Corning Optical Grade) as a function of temperature and wavelength as taken from his article. A quartz envelope thickness of 1 millimeter at 2.67 micrometers thus translates (via Equation 1.1) to about 10% envelope absorption. Since Kirchoff's Law holds, this 10% will be reradiated according to the envelope temperature by Plank's Law. Envelope temperature will be several hundred degrees Celsius, while the filament temperature will be about 2000° Celsius. From Figure (1.7) it is apparent that this reradiation from the warm envelope will be (at 2.67 micrometers) about four orders of magnitude down from the primary filament radiance and thus negligible. Further, the reflector geometry of Figure (3.2) induces strong off-axis aberrations and thus envelope reradiation will be reduced even further in the light source collimated output beam. From Figure (3.3) the absorption coefficient change with temperature at 2.67 micrometers and in the 2.45 - 2.55 micrometer range is similar and small. The roughly 10% absorption at 2.67 micrometers is thus a constant offset readily removed during the calibration process, permitting the use of conventional quartz halogen lamps in a 2.67 micrometer radiometer. This result is in keeping with previous

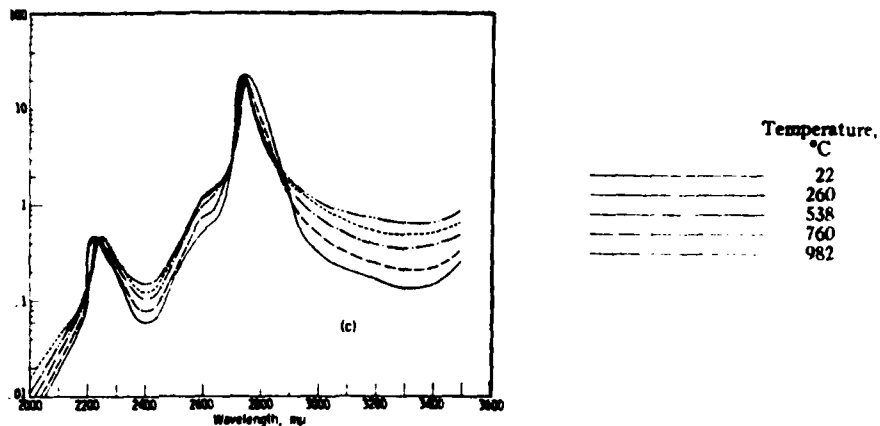


Fig. (3.3) Quartz Absorption Coefficients

experimental work (Hyson and Hicks, 1975) and permits significant savings in both expense and complexity over specialized infrared sources.

It is now possible to estimate the spectral output of such a lamp. According to Stair *et al.* (1963), a 200 watt quartz halogen lamp will produce about 1.04 microwatt per square centimeter per nanometer bandpass irradiance at a 43 centimeter distance at 2.6 micrometer center wavelength. Assuming spherically isotropic filament radiation and that one captures usefully about 75% of this output, the 150 watt Osram lamp (No.64635) will produce 18 watts/micrometer at 2.6 micrometer wavelength. If the filter bandpasses are 0.01 micrometers, then there is a beam power accessible to the filtered detectors of about 90 milliwatts. Even after allowing for system losses, this is more than adequate and allows the filament to be operated at much less than rated current and voltage, resulting in longer life and reduced thermal problems. Figure (3.4) shows the vapor pressure of tungsten as a function of temperature. The Osram No. 64635 lamp has a design life of 50 hours at an operating filament temperature of 3400° Kelvin. If we ignore the halogen cycle then the lamp life is inversely proportional to the tungsten vapor pressure of Figure (3.4), and the same lamp operated at a filament temperature of 2000° Kelvin will last essentially indefinitely. Filament evaporation and thus mechanical resistance changes are totally negligible.

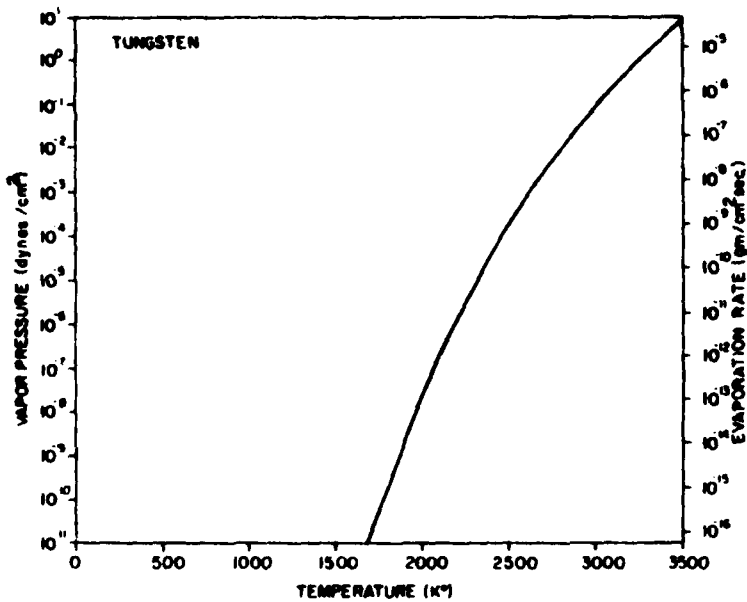


Fig. (3.4) Vapor Pressure of Tungsten

The tungsten filament electrical resistance is a strong function of filament operating temperature according to Equation (3.3):

$$R/R(0) = (t/t(0))^{1.20} \quad (3.3)$$

where t = filament temperature, $t(0)$ = a reference temperature, R = filament resistance, $R(0)$ = filament resistance at $t = t(0)$. Figure (3.5) illustrates this tungsten resistivity change as a function of temperature. Thus, by knowing the particular filament resistance at room temperature and using Equation (3.3) one can configure a feedback controller that will sense the filament resistance (and thus its temperature) and adjust the electrical power through the filament to maintain it at constant temperature regardless of external influences such as ambient temperature and cooling airflow. The engineering details of this will be described in Section (3.2.4)

Since it is necessary to measure the ratios of the received powers $I(1)$ and $I(2)$ at 2.67 and about 2.45 micrometers to 0.1% as a design goal, is also necessary to maintain the filament temperature fairly constant since changing the filament grey body temperature will change the spectral output according to Planck's law. Figure (3.6) illustrates the absolute and relative filament temperature control accuracy required to maintain the intensity ratio [$I(1)/I(2)$] from Equation (1.2) error due to source spectral drifts to the design goal of 0.1%. The signal

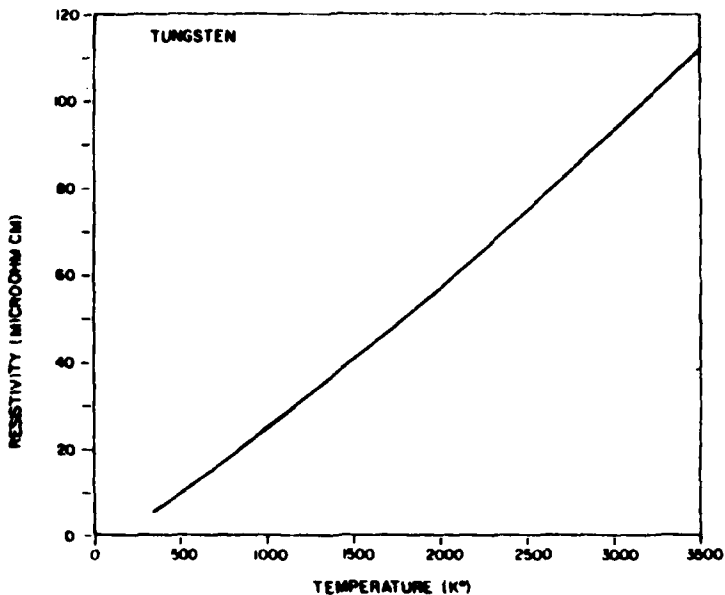


Fig. (3.5) Resistivity of Tungsten

wavelength is fixed at 2.65 micrometers and curves are presented for reference channels at 2.45 and 2.55 micrometer center wavelength. Moving the signal and reference filter wavelengths closer together significantly reduces required filament temperature control accuracies as does operating the lamp at higher temperatures. As discussed above, a lamp filament temperature of about 2000° Kelvin is a good operating point from the standpoint of lamp life and filament geometric stability.

From Figure (3.6) it can be seen that a lamp filament temperature feedback controller with an accuracy of only 0.5% will be sufficient to keep filament temperature related transmission errors within 0.1% if it is operated at a reference wavelength of 2.45 micrometers. Engineering design of the filament temperature controller and readout are given in Section (3.2.4).

3.1.3 Focusing Optics

The infrared light intensity from the light source (Figure 2.1, Item 1) must be efficiently captured and focused into a collimated beam to be transmitted through the sample volume (3). In this implementation, a one inch diameter beam will be transmitted through the sample volume. This is mechanically convenient and large enough to permit any reasonable hydrometeor particle to occult the beam without

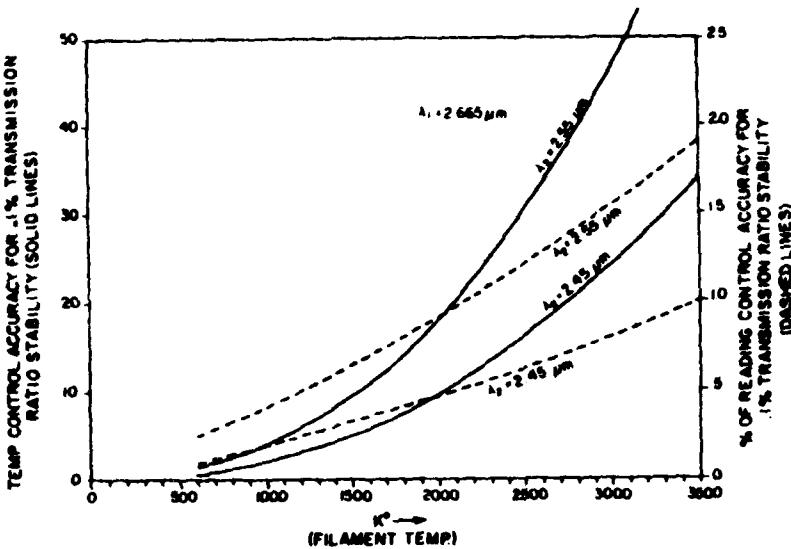


Fig. (3.6) Filament Temperature Control Accuracy

causing a significant absolute beam energy loss. After passing the sample volume the beam is split, filtered, and then refocused on the 1 millimeter square active areas of the Lead Sulfide detectors (10).

Conventional glass optics are not suitable for this optical focusing since they are somewhat absorptive in this region of the infrared. Low F/number optics are also desirable in this application to reduce mechanical size. It will be shown in Section (4.2) that air irradiance temperature signal level is inversely proportional to system F/number. Low F/number infrared optics are even more critical in that application. Low F/number (less than 1.0) infrared refractive optical elements have severe spherical aberrations that limit their ability to efficiently focus collimated energy to a 1 millimeter spot. The typically high index of refraction of most infrared transmitting materials leads to Fresnel reflection losses from lens surfaces that may approach 50%, and anti-reflection coatings increase cost and delivery time while reducing durability. Corrected multi-element lenses are prohibitive in cost. Also, infrared alignment of refractive optical chains can be a problem since refractive index changes with wavelength will focus infrared and visible light to different points. Also, many infrared optical materials are opaque in the visible. For all of these reasons, only reflecting infrared focusing elements will be used in both this and the air temperature radiometer design. Reflective elements have no chromatic or spherical aberrations and thus have small focused spot sizes and permit alignment with visible light at low F/numbers.

Reflecting surface efficiencies (vacuum deposited gold) approach 99.4% and are stable with time. All focusing elements will be off-axis 90° segments cut from electro-formed paraboloidal reflectors as shown in Figure (3.7) For an incoming 1 inch diameter beam, the reflector

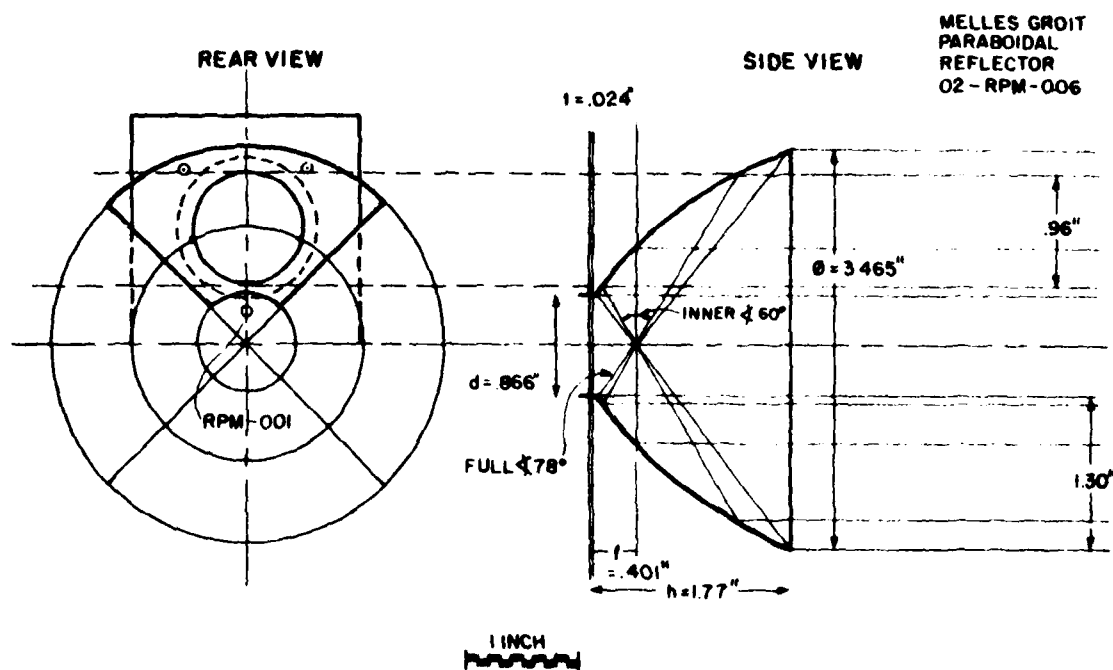


Fig. (3.7) Parabolic Reflector Segment Shapes

effective F/number is about 0.87. For a 1.3 inch diameter beam using the full reflector segment area, the effective F/number is reduced even further to 0.62. When mounted as shown in Figure (3.8), each off-axis parabolic segment will turn an incoming collimated beam 90° and bring it to a sharp focus. The reflector surfaces will be front-surface coated with a highly specular reflective vacuum-deposited gold layer. Four significant benefits result. First, since gold is very reflective in the 2.4-4.3 micrometer region, a surface specular reflectivity approaching 99.4% yields much improved system efficiency. Second, by Kirchoff's Law, thermal emission from the mirror surface is reduced to an effective emissivity of about 0.006. Third, gold being a very stable substance, yields infrared mirrors whose reflectivity change with age is minimal compared to more conventional coatings such as aluminum.

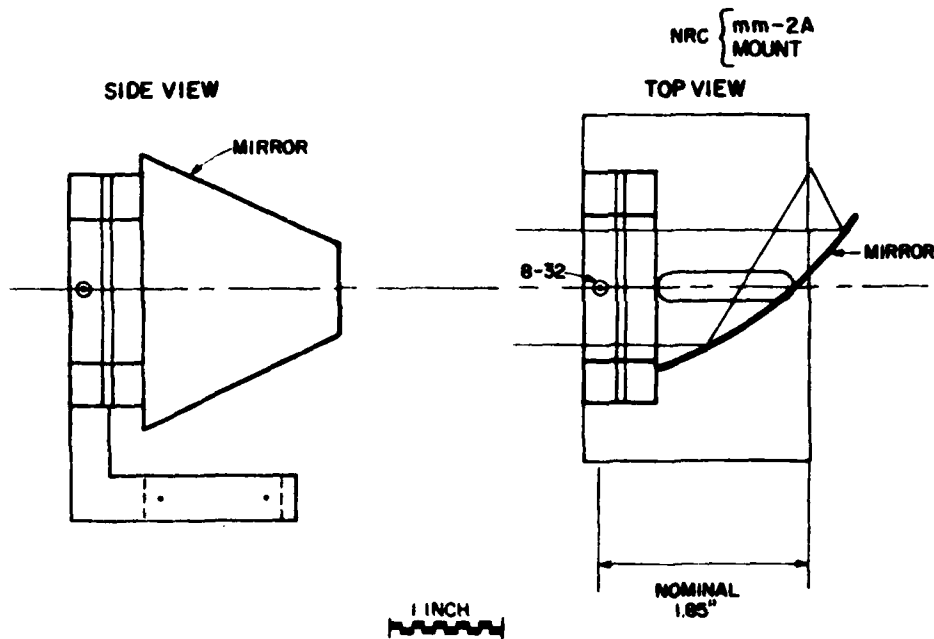


Fig. (3.8) Parabolic Reflector Segment Mount

Mechanical softness of the gold layer is not significant since the reflective optics will be used in a closed hermetically sealed environment. Fourth, the gold layer has infrared (2.5-4.3 micrometer) reflectivity of about 99.4% while its visible light reflectivity is about 50% and thus acts as a dichroic mirror to reduce the transmission of potential interfering solar radiation and the short-wavelength light from the strong broadband emitting light source.

3.1.4 Beamsplitter

The broadband infrared beamsplitter will be a 1 millimeter thick polished but uncoated germanium or silicon circular wafer provided by the Unique Optical Company of Farmingdale, New York. These materials have an extremely high (about 4.0) infrared refractive index leading to a correspondingly high surface reflection coefficient. They are therefore used with custom deposited anti-reflection coatings tailored to a specific wavelength in most infrared optical applications. In this particular use as a broadband beamsplitter, the high reflectivity and low bulk absorption at 2 - 3 micrometers of the uncoated substances becomes an advantage. Transmission/reflection ratios at normal

incidence for an uncoated germanium beamsplitter are nominally 53/47% while uncoated silicon yields nominally 46/54%. Multiple internal reflections and 'ghost' images are not of concern since this is an intensity splitting rather than an image forming application. While germanium has slightly better optical properties, silicon has better mechanical and environmental stability and is not subject to runaway power absorption at temperatures above 50° Celsius and will thus be used for the design presented here.

As shown schematically in Figure (2.1), mechanical constraints make it necessary to use the silicon beamsplitter at other than normal incidence where the simplified reflectance equations (3.1) and (3.2) must be replaced by the full polarization dependent Fresnel equations. These full equations may be found in any theoretical optics text and are reproduced below for a single reflecting surface in air as:

$$R_{\parallel} = \tan^2 (\theta_i - \theta_t) / \tan^2 (\theta_i + \theta_t) \quad (3.4)$$

$$R_{\perp} = \sin^2 (\theta_i - \theta_t) / \sin^2 (\theta_i + \theta_t) \quad (3.5)$$

where: $\Phi(t)$ and $\Phi(i)$ are the transmitted and incident apex angles, related by Snell's Law given as:

$$\sin \theta_i / \sin \theta_t = n_1 / n_2 \quad (3.6)$$

The parallel and perpendicular symbols refer to the electric vector components parallel and perpendicular to the plane of incidence on the beamsplitter substrate. R is the surface reflectivity. Since thermally generated radiation from a hot surface is composed of equal components of both polarizations, one may calculate the beamsplitter effective polarization independent reflectivity as:

$$\bar{R} = \frac{1}{2} (R_{\parallel} + R_{\perp}) \quad (3.7)$$

Interference effects are neglected in the above discussion, since neither source coherence nor beamsplitter flatness is sufficient to act as a Palby-Perot interferometer. Incoherent intensity summation is thus valid.

Knowing that the index of refraction [n] is 3.44 for silicon in the wavelength range of 2.4-2.7 micrometers and that its absorption coefficient is 0.01 cm⁻¹, then Equations (3.4) through (3.7), Beer's Law, and Kirchoff's Law are sufficient for a ray-tracing analysis of the beamsplitting ratio of a 1 millimeter thick 2-surface silicon window as a function of incidence angle. Since the results are numerically complex, this analysis has been implemented as a FORTRAN program rather than analytically. The results showing 2.4-2.7 micrometer silicon beamsplitter efficiency as a function of incidence angle are shown in Figure (3.9). As shown in the figure, a silicon window at 45° incidence angle will thus act as a stable broadband (45%/65%) intensity beamsplitter. For mechanical ease, this 45° incidence angle will be used in the electro-optical design. If the input beam diameter is 1 inch, a 2 inch diameter silicon beamsplitter is thus required.

Polarization differences in the transmitted and reflected beams as shown

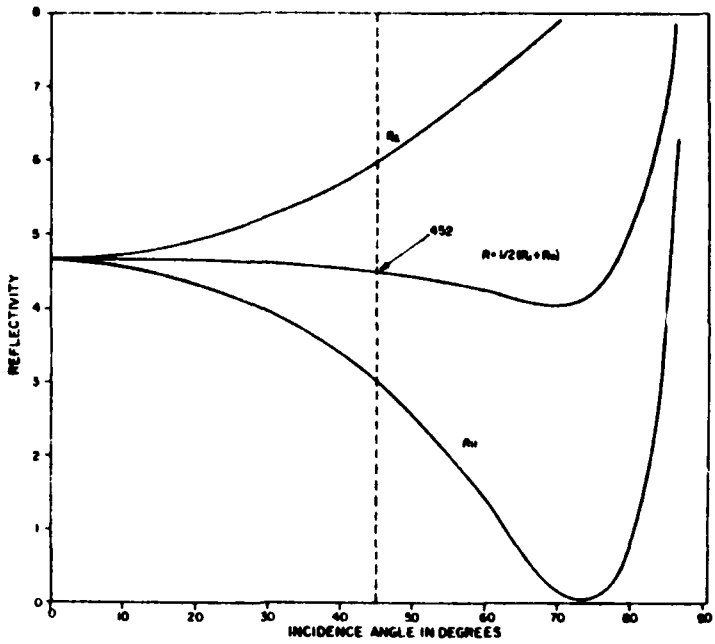


Fig. (3.9) Silicon Two-Surface Fresnel Reflectivity

in Figure 3.9 are not detrimental since the sensors are normal to the beam and respond equally to both polarizations.

3.1.5 Infrared Wavelength Selection

The absorbed signal channel will be at 2.666 micrometers which is the strongest available infrared water vapor absorption peak and thus results in a minimal path length device. Filter bandpass will be 0.01 micrometer nominal, this tight filtering being required to remain in the strongest portion of the absorption band. The reference channel will be chosen at a shorter wavelength than the signal channel so that the second order effect of particulates in the beam will be to cause conservative underestimates of absolute humidity as shown earlier in Section (1.3). Exact wavelength position of the reference channel is not critical. As shown in Section (3.1.2), the closer the reference channel is to the signal channel in wavelength, the less critical is the light source temperature stability requirement. The 2.45 micrometer reference channel wavelength position discussed in Section (1.3) was chosen since this wavelength is a local minimum in the water vapor absorption. Over a 20 centimeter path, any conceivable atmospheric

water vapor density will have an absorption at 2.45 micrometers of much less than 0.001. The 2.67 micrometer channel will be completely solar blind but the instrument light source intensity in the 2.45 micrometer reference channel will be roughly comparable to direct solar irradiation and only about 50% of the 2.45 micrometer solar rays will be absorbed in the intervening atmosphere. Thus the reference channel is not blind to direct solar radiation. However, the diffuse component of skylight is many orders of magnitude lower than direct solar energy and by configuring the detector aperture to view only the light source window, it will be insured that the detector will never 'see' direct sunlight. Sunlight specularly reflected from the light source window could be seen by the detector and thus some thought needs to be given to the eventual mounting orientation to be minimize this possibility. A vertical orientation with the light source above the receiver would seem best. An alternate solution would be to move the reference channel further into the absorption band (say 2.55 micrometers) so that both become solar-blind. However, then Equation (1.8) cannot be simplified to Equation (1.9) and the analysis becomes much more complex. This option will therefore only be investigated when the 2.45 micrometer reference channel has been proven experimentally and only if laboratory tests show solar interference to be a problem. Another solution method would be to modulate the instrument light source and detect synchronously. This technique will be avoided in order to permit the use of a unique self-calibrating ratiometric electronic system to be described in Section (3.2.2).

3.1.6 Infrared Narrowband Filters

The system 2.45 and 2.66 micrometer, 0.01 micrometer bandwidth filters will be custom fabricated by Omega Optical Inc. of Brattleboro, Vermont. They will be 2 cavity interference filters with out-of-band blocking from X-ray to beyond the response cut-off of the lead sulfide detectors. While pure Fabry-Perot transmission filters have spurious sideband multiple order transmission peaks occurring at shorter wavelengths and pure all-dielectric multi-layer bandpass filters generate sidebands on both sides of the filter wavelength, the filters proposed are not simple all-dielectric multi-layer bandpass filters and contain other components to block these sideband transmission peaks. High wavelength sidebands are blocked by low-pass colored glass elements and low wavelength sidebands are blocked by an induced transmission filter stack, resulting in a true single peak bandpass filter. Rejection outside the passband is typically by a factor of 1,000 to 10,000. As opposed to ultraviolet bandpass filters, infrared narrow-band filters are quite stable. Several manufacturers routinely manufacture them to the temperature and humidity requirements of MIL-STD 810B. Center wavelength shift with temperature is typically 0.005%/° Celsius. Peak transmission changes with temperature at about 0.01%/° Celsius and bandwidth changes with temperature are less than 0.01 Angstrom/° Celsius. Measured bandpass curves will be provided with each filter. Such filters have been used in the field by, for example, Hysun and Hicks (1975). Off-axis shifts in center wavelengths are eliminated by a system of collimating baffles (7) which also insure that the detectors view only the light source aperture (1).

It is interesting to note that stable narrow band filters are not available in the Lyman-Alpha region of the vacuum ultraviolet thus prohibiting the far ultraviolet implementation of the differential technique that gives the proposed infrared instrument its stability and hydrometeor rejection properties.

The off-axis characteristics off the interference filters impose two design constraints upon the optical system. First, off-axis light will shift the filter center wavelength to lower wavelengths according to the following relation:

$$\lambda_x / \lambda_0 = [(1.65)^2 - \sin^2 \theta]^{\frac{1}{2}} / 1.65 \quad (3.8)$$

Thus if the collimated light beam is incident on the filter at less than 90° incidence the filter center wavelength will be shifted slightly to shorter wavelengths. This effect can be used to fine tune a filter wavelength to an exact center value but it must begin with the filter normal to the input beam. The second filter design constraint is more stringent. It can be seen from Equation (3.8) that the effect of a convergent or divergent light beam striking the filter will be both to broaden the bandpass and to shift it to shorter wavelengths. In practice, this effect is negligible at system F/numbers of F/11 and above. However, the off-axis parabolic segments will generate effective F/numbers as low as 0.6 and the interference filters cannot be placed in this highly convergent focused beam. They must instead be placed in an essentially parallel beam prior to the parabolic focusing element.

3.1.7 Potential Optical Problem Areas

There are two potential problem areas relating to the optical design of the absolute humidity sensor. One relates to the light source stability and the other concerns the bandpass filters and their out of band blocking and solar blindness.

In Section (3.1.2) we discuss the use of a conventional quartz-halogen lamp as a light source in spite of its envelope absorption of about 10% at 2.67 micrometers. While both the discussed theory and previous publications indicate that the envelope absorption should not degrade the differential intensity measurements at 2.67 and 2.45 micrometer, it is possible that the quartz halogen lamp will prove unsuitable when actually used in detailed laboratory tests and calibrations. If this proves to be the case then a conventional far-infrared glowbar, nerst-glower, nichrome-ceramic element, or possibly an oxidation resistant thorium filament will be substituted.

The out of band rejection of the narrowband filters must also be considered since the light source is quite intense at all wavelengths. It can reasonably be expected that a filter out of band rejection of 99.99% is achievable. Also, the Lead Sulfide detectors have a sharply spectrally sensitive response peaking at 2.5 - 2.75 micrometers as will be shown in Section (3.2.1). It is nevertheless possible that an additional long-pass infrared filter with an approximately 2.4 micrometer cut-on will prove useful in reducing out of band signal

contamination. Obviously, careful baffling to reduce stray light in the detector housing will be essential. Also, the 2.45 micrometer sensor will not be totally solar blind to either direct or specularly reflected solar irradiation. Some thought will therefore need to be given to orientation and field of view in an eventual aircraft location. This solar effect will be investigated in the prototype and proposed solutions commensurate with the experimental severity of the effect will be made. The first indication is that simple mechanical orientation of the sensor and field of view limitations will be adequate to remove any possible solar effects.

3.2 Electronic Design

3.2.1 Lead Sulfide Photodetectors

Infrared detection of the filtered narrow band wavelengths will be accomplished by a matched pair of photoconductive lead sulfide detectors (10) provided in hermetically sealed TO-5 packages by Optoelectronics, Inc. They will be a matched pair selected at the factory for compatible dark resistance, signal to noise ratio, detectivity, responsivity and temperature drift. They behave as variable resistors whose resistance is approximately inversely proportional to incident radiation intensity and have an ideally suited response function which peaks in the 2.4 - 2.7 micrometer wavelength range. They are quite stable and routinely fabricated to withstand the temperature humidity environment of MIL-STD 331, Test 105, shock in excess of 10 G, high vacuum, and nuclear radiation effects.

Their dark-resistance varies by about 2% per $^{\circ}$ Celsius at room temperature and thus true system accuracy (0.1%) requires that their temperature be held constant to about 0.06 $^{\circ}$ Celsius. This sensor substrate temperature stability will be achieved via a commercially available sensor, thermoelectric cooler, and feedback thermistor module in a TO-5 can as illustrated in Figure (3.10). This evacuated, cooled solid-state package permits the sensing surface to be maintained at a constant temperature of -30 $^{\circ}$ Celsius. This cold temperature decreases background level and system noise while increasing the Lead Sulfide responsivity and detectivity by about a factor of three over room temperature operation. Another significant benefit is that the device wavelength dependent response sharply peaks in the 2.45 - 2.67 micrometer region when cooled to -30 $^{\circ}$ Celsius as shown in Figure (3.11).

It is proposed that the Lead Sulfide sensors be used in an unconventional bias and amplification mode as will be discussed in Section (3.2.2). To explain this mode of operation, it will be useful to present a quick review of the basic theory of photoconductive detectors in this section. Since both the Lead Sulfide and the Lead Selenide detectors are intrinsic photoconductors, the discussion will apply equally to both sensors.

OTC-22-5

SERIES TWO STAGE
THERMOELECTRICALLY COOLED
LEAD SULFIDE DETECTORS

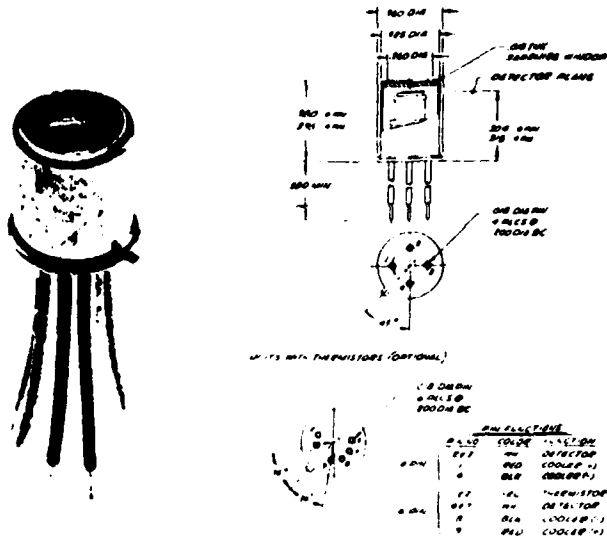


Fig. (3.10) Lead Sulfide Sensor Hermetic T0-5 Package

In free atoms, the electrons are confined to well defined quantum orbits and energy states. In solids, the effect of neighboring atoms is to smear and overlap these energy levels into 'bands'. In electrical non-conductors, the electrons are still closely associated with their individual molecules or atoms in the valence band and not free to migrate. In metallic conductors, some electrons are in the conduction band and free to migrate throughout the substance. These are conduction electrons and under the influence of an electric field they comprise the current conducted through the metal. The electrical conductivity of the metal (i.e. the reciprocal of resistivity) is just the number [N] of these conductance band electrons per unit volume times their mobility [m]. Intrinsic semiconductors such as lead selenide and lead sulfide are an intermediate case between insulators and metals. Normally, most of their electrons are tightly bound in valence band orbits as shown in Figure (3.12). In semiconductors the energy gap [Eg] between the valence and conduction bands is relatively small and if an electron is somehow (thermal excitation or photon absorption) given sufficient energy it will be excited into the conduction band. It leaves behind its empty quantum site (a positive 'hole') and eventually falls back and becomes bound in a vacant site in the valence band.

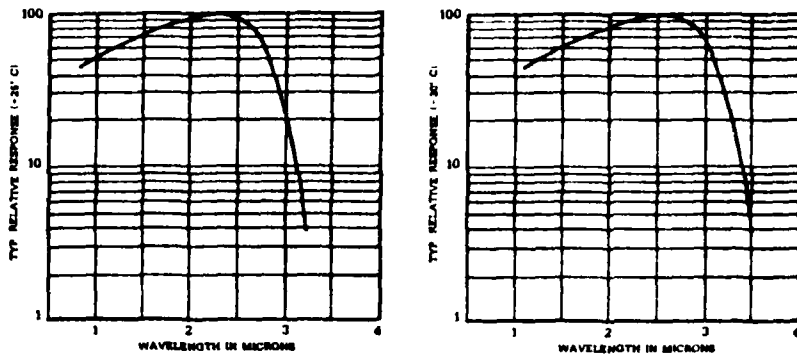


Fig. (3.11) Spectral Response of Lead Sulfide

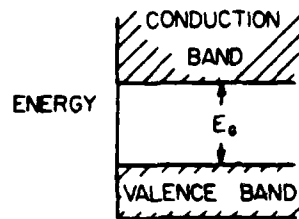


Fig. (3.12) Semiconductor Band-Gap Structure

While in the conduction band it is free to wander through the crystal lattice and contribute to the semiconductor conductivity [C] according to:

$$C = Nme \quad (3.9)$$

where e is the electron charge. Note that conductivity and conductance, as opposed to resistance and resistivity, are linearly related to the number density [N] of free electrons. In intrinsic semiconductors such as Lead Sulfide and Lead Selenide, electrons can be promoted to the conduction band by both random thermal motion in the substrate and by capturing incident photons.

In the absence of incident photons, the number of electrons $[N_{th}]$ in the solid having random thermal energies in excess of the bandgap energy $[E_g]$ is given by the Boltzman distribution as:

$$N_{th} = N_0 \exp(-E_g / 2 k T) \quad (3.10)$$

where T is Kelvin temperature and k is Boltzman's Constant. For Lead Sulfide and Lead Selenide at tropospheric temperatures, this thermal effect results in a temperature dependence of dark resistance (inverse conductance) of about -2% Kelvin. If the substrate temperature is held constant then there is still a finite number $[N]$ of electrons in the conductance band (Equation 3.10) even if no light illuminates the photoconductor. This results in a Lead Sulfide dark resistance at room temperature of about one megohm/square. If the substrate temperature were to increase slightly, the increased conductance according to Equation (3.9) would be indistinguishable from that caused by an increased photon flux.

If the increased number of conductance band electrons $[\Delta N]$ is due to photon capture rather than an increase in substrate temperature, the phenomenon is called 'photoconductivity'. If an absorbed photon is to cause an electron to be promoted across the quantum energy gap $[E_g]$ in Figure (3.12) then it must have an energy in excess of :

$$E_g = h \nu \quad (3.11)$$

where ν is the frequency of the photon and h is Plank's Constant. This results in a long-wavelength cutoff beyond which photons are not energetic enough to knock photoconductor electrons into the conduction band. This cutoff is not perfectly sharp but is a fairly steep function of frequency. It is also temperature sensitive, moving to lower frequencies (higher wavelengths) with decreasing temperature. This is because of changes in the width of the forbidden band gap $[E_g]$ with temperature and explains the Lead Sulfide temperature and wavelength detector efficiency curves given in Figure (3.11).

Now consider a photoconductor illuminated with $q(\nu)$ photons/second at frequency $[\nu]$. By Beer's Law a fraction $\exp(-\alpha(\nu) N(0) d)$ will be absorbed where $\alpha(\nu)$ is the absorption cross section of the valence band electrons and d is the detector thickness. The number density of light-generated conduction band electrons is thus:

$$N_{\nu} = q_{\nu} \tau \exp[-\alpha_{\nu} N_0 d] \quad (3.12)$$

where τ is the mean lifetime of the electrons before falling back into a vacant 'hole' in the valence band. Thus the photoconductor conductivity due to thermal processes and photon absorption is the sum of these effects:

$$C = m e [N_{th} + N_{\nu}] \quad (3.13)$$

and the photoconductor conductivity is a linear function of the incident monochromatic light intensity (watts or photons/sec) and has an offset 'dark' conductivity determined by the substrate temperature. It is common to express the photoconductor response in terms of its resistance [R] instead of the more physically meaningful conductivity [C] according to:

$$R_D = k_g / C = k_g / [m e (N_{th} + N_{nu})] \quad (3.14)$$

where $k(g)$ is a device geometry factor converting from resistance to resistivity. Thus the device conductance change is linear in incident light intensity. However, device resistance [R] is only approximately inversely proportional to incident light intensity due to the thermal offset conductivity factor $[N(th)]$ in Equation (3.14).

Photoconductor manufacturers almost exclusively characterize and test their photoconductor Lead Sulfide and Lead Selenide devices in the constant voltage bias circuit shown in Figure (3.13) where $R(L)$ is a constant load resistor (typically 1.0 megohm), $R(D)$ is the photoconductor resistance, $V(B)$ is a constant voltage bias and the output quantity is the variable voltage $[V(out)]$ which depends on $R(D)$ according to:

$$V_{out} = V_B [R_D / (R_L + R_D)] \quad (3.15)$$

Typically manufacturers' data give the photoconductor responsivity $[\Sigma]$ which is the voltage output change $[\Delta V(out)]$ as a function of a small charge ΔW in incident light intensity on the photoconductor in the circuit of Figure (3.10). Units of Σ are thus (volts/incident watt). Differentiating Equation (3.15) gives:

$$\frac{\partial V_{out}}{\partial R_D} = V_B [R_L / (R_L + R_D)^2] \quad (3.16)$$

and by the definition of responsivity in the circuit of Figure (3.13):

$$\frac{\partial V_{out}}{\partial W} = -\Sigma \quad (3.17)$$

Eliminating $dV(out)$ from the above two Equations:

$$\frac{\partial R_D}{\partial W} = -\Sigma [(R_L + R_D)^2 / V_{in} R_L] \quad (3.18)$$

Since by definition the photoconductor conductance (C) is just:

$$C_D = 1/R_D \quad (3.19)$$

One can write the coordinate transform:

$$\frac{\partial C_D}{\partial W} = (\frac{\partial C_D}{\partial R_D})(\frac{\partial R_D}{\partial W}) = -(1/R_D^2)(\frac{\partial R_D}{\partial W}) \quad (3.20)$$

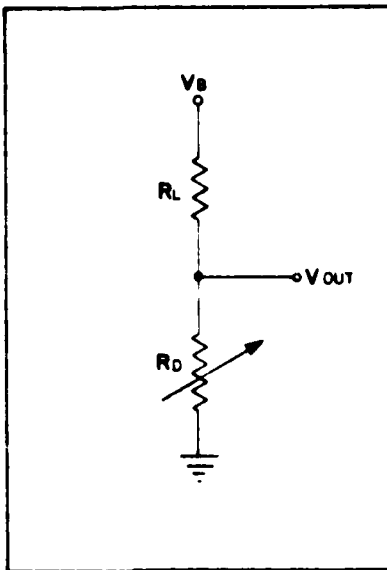


Fig. (3.13) Photoconductor Test and Bias Circuit

Eliminating variables between Equation (3.20) and (3.18) determines a conductance responsivity $[\Sigma(\text{cond})]$ in units of siemens/volt as:

$$\Sigma_{\text{cond}} = \partial C_D / \partial W = [1/(V_B R_L)] [R_L + R_D]^2 / R_D^2 \Sigma \quad (3.21)$$

Integrating Equation (3.21) with the boundary conditions that C goes to $1/R(\text{dark})$ as W goes to zero, gives:

$$C_D = [[\Sigma / V_B R_L] [(R_L + R_D) / R_D]^2] W + 1/R_{\text{dark}} \quad (3.22)$$

The end result of this manipulation is that device conductance is shown to be linear in incident light intensity with a temperature dependent constant offset in accordance with Equations (3.13) and (3.14). The bracket term is a constant easily determined by the manufacturer's test circuit (Figure 3.13) and published value of device voltage responsivity enabling a full DC evaluation of device response to incident light from a single AC coupled manufacturer's data point. This knowledge of device conductance as a function of W will be necessary in Section (3.2.2).

The Lead Sulfide photoconductors used in the absolute humidity sensor (Figure 2.1, Item 10) will be Optoelectronics Inc, Model OTC-22-5 two stage thermoelectrically cooled lead sulfide detectors as shown in Figure (3.10). Relevant manufacturer's data at a cooler stabilized

temperature of - 30° Celsius are:

$$\begin{aligned}R &= 2.5 \text{ megohms} \\ \text{Size} &= 1 \text{ mm square} \\ V &= 50 \text{ volts} \\ R &= 9E + 5 \text{ volts/watt} \\ R &= 1.0 \text{ megohm}\end{aligned}$$

Substituting in Equation (3.22) yields the result:

$$C_{D,OTC225} = 0.035W + 4.0E-7 \quad [\text{Siemens}] \quad (3.23)$$

Converting back to photoconductor resistance as a function of incident light power (watts) via Equation (3.19) results in the characteristic curve of Figure (3.14). The linear conductance relation of Equation

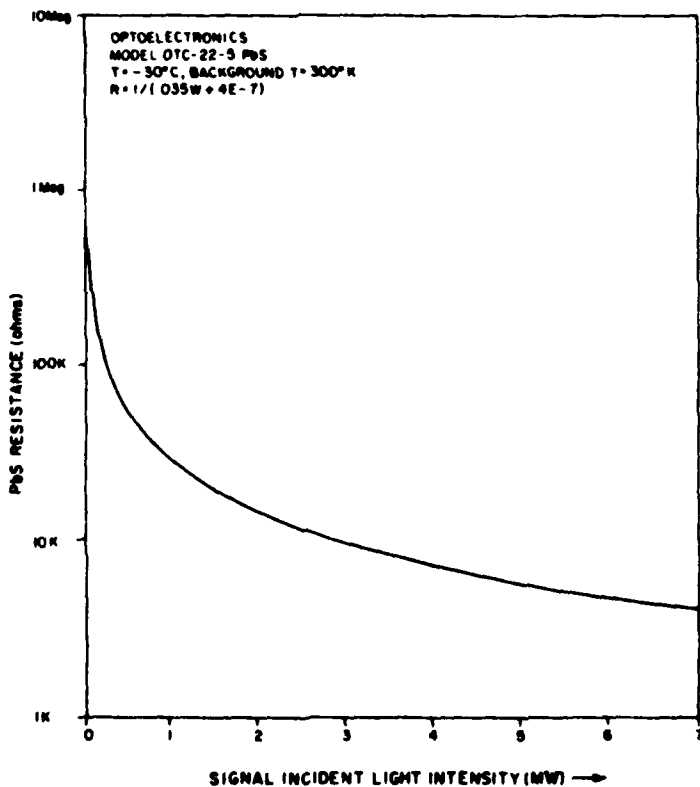


Fig. (3.14) Lead Sulfide Resistance Curve

(3.13) will remain valid so long as the bias current flowing through the

Lead Sulfide resistive element does not cause its temperature to increase due to significant self-heating. This self-heating would cause a thermally induced change in conductance according to Equation (3.10). According to manufacturer's data provided by Infrared Industries, at a detector constant bias voltage of 10 volts DC detector resistance can drop as low as about 10K ohms in a thermally unstabilized 1 millimeter square detector without causing significant self-heating. This corresponds to an electrical power dissipation in the sensor of about 10 milliwatts.

The Lead Sulfide sensor proposed here and shown in Figure (3.10) is thermostatically cooled to a feedback stabilized temperature of -30° Celsius. The sensor two-stage thermoelectric cooler can cool to -30° Celsius from a room temperature background and still have an excess cooling capability of about 100 milliwatts, so the bias voltage electrical sensor heating is automatically compensated in a thermoelectrically stabilized sensor. The Lead Selenide sensors can therefore be operated as temperature stabilized conductance linear elements at sensor resistances of 10.0K ohms. From Figure (3.14) this corresponds to sensor received infrared radiant power of about 3 milliwatts.

In Section (3.1.2), the Osram 64635 light source at rated power is shown to be able to deliver 90 milliwatts to each of two sensors through a 50/50 beamsplitter and 0.01 micrometer bandpass filters. If we now allow for 14% losses at each of two sapphire system windows, a 10% lamp envelope absorption loss, and filter bandpass transmission efficiencies of 40%, then the lamp can theoretically deliver 23 milliwatts to each of the two sensors. Reduce this by a factor of 4 to allow for real-world defocusing losses and the sensors should each receive about 6 milliwatts or twice the goal of 3 milliwatts/sensor. The lamp can thus be operated at 2000° Kelvin filament temperature and much less than rated power where all the synergistic good effects due to the lower filament temperature as mentioned in section (3.1.2) are attained.

3.2.2 DC Ratiometric Coupling

It can be seen from Equation (3.23) and Figure (3.14) that Lead Sulfide sensor conductance is linear with incident light intensity but that sensor resistance is only approximately inversely proportional to incident light intensity due to the constant conductance offset term. Suppose the reference channel power is 3 milliwatts and the signal channel received light power is reduced 80% due to water vapor absorption ($T = 0.200$) to a value of 0.6 millivolts. At this signal strength the simple inverse resistance relation is only accurate to about 2% and does not meet the stated 0.1% accuracy design goal. A signal processing method that includes the constant conductance offset must be devised.

Consider the ratiometrically coupled scheme shown schematically in Figure (2.1) where the 2.67 micrometer filtered signal channel Lead Sulfide detector and the 2.45 micrometer filtered reference channel Lead Sulfide detector are respectively configured as the load and feedback

resistors of an operational amplifier (Figure 2.1, Item 12) with a constant bias voltage [$V(B)$] as in (Figure 2.1, Item 11). The output voltage of the operational amplifier will be:

$$V_{out} = -(R_{2.45}/R_{2.67})V_B \quad (3.24)$$

Converting to conductance-linear input irradiance [W] via Equations (3.23) and (3.19) yields:

$$V_{out} = -[(0.035W_{2.67} + 4.0E-7)/(0.035W_{2.45} + 4.0E-7)] V_B \quad (3.25)$$

Since the reference channel irradiance [$W(2.45)$] is not absorbed by the water vapor in the path, it is essentially a constant set by the device geometry and light source intensity. As shown in Section (1.3), the absolute worst hydrometer attenuation of $W(2.45)$ would be less than 2%. If $V(B)$ is fixed at 10.000 volts DC and $W(2.45)$ is 0.003 watts then Equation (3.25) reduces to:

$$V_{out}/V_B = -332.068 W_{2.67} + 0.000379 \quad (3.26)$$

and is exactly linear in $W(2.67)$ and thus in $(W(2.67)/W(2.45))$. The small constant offset and gain change are easily corrected by standard operational amplifier techniques to give a direct linear reading of the vapor transmissivity, $T = I(1)/I(2)$, from Equation (1.9).

Because of the small conductance offset terms in Equation (3.25), changes in the absolute intensity of the light signals from the ratio $W(2.67)/W(2.45)$ will have slight second order effects on the output voltage estimation of T . At lower vapor densities when $W(2.67)$ is approximately equal to $W(2.45)$ the error goes to zero. The worst case error, if one operates at T larger than 0.2 (See Figure 1.2) resulting from a 5% source received intensity drift equally affecting both channels will cause an error of less than 0.08% in the previously calibrated estimate of T from Equation (3.25). Once again the device becomes more accurate at lower absolute humidities and meets the design goal of all error sources being each less than 0.1% in the measurement of T .

3.2.3 Transmissivity Transfer Equation

The next task is to design a voltage amplification method whereby the linear slope and offset of Equation (3.26) can be adjusted so that $V(out) = 0.0$ when $W(2.67) = 0.0$ and $V(out) = V(B)$ when $W(2.67) = W(2.45)$ due to a complete lack of water vapor in the sample path length [L]. This will result in a direct linear calibrated readout of water vapor transmissivity [T]. Consider the two wavelength transmissometer system shown in Figure (3.15).

The entire optoelectronic system transfer function for the system linear output proportional to [T] can now be derived. Define the following quantities as:

$I(2.67)$ = the bulb output power captured by $R(1)$ at 2.67 micrometer ± 0.05 micrometer (nominally

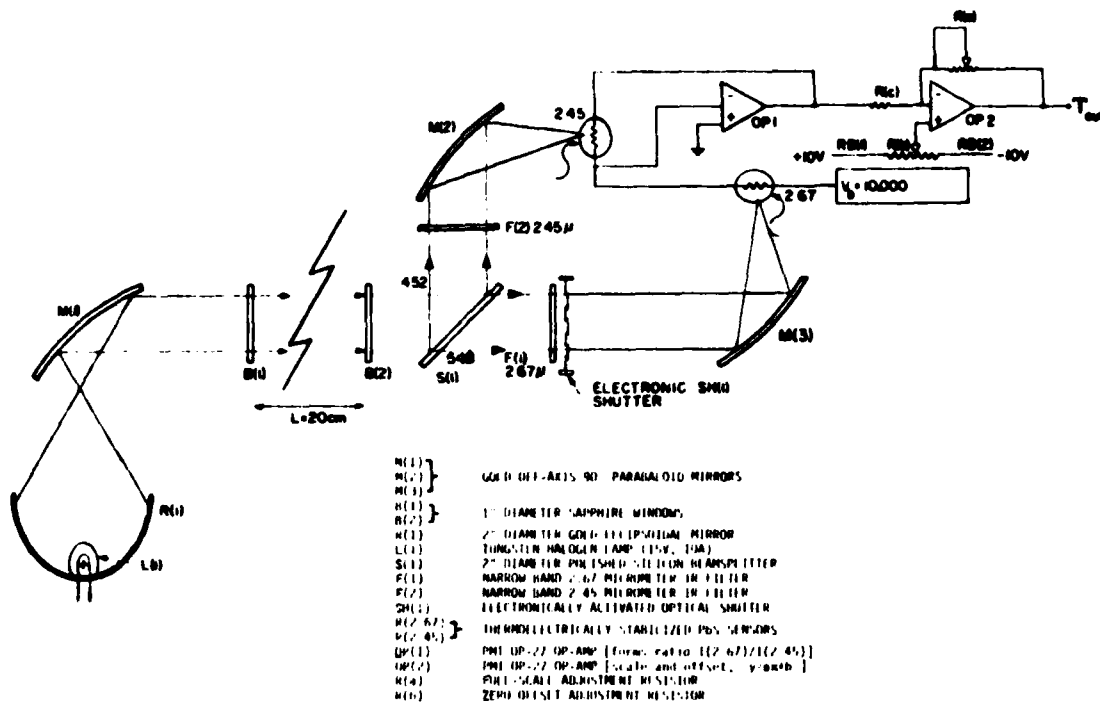


Fig. (3.15) Transmissometer Electro-Optical Schematic

175 milliwatts)

I = the bulb output power captured by R(1) at 2.45 micrometers ± 0.05 micrometers (nominally 185 milliwatts)

Q(abs) = quartz envelope absorption at 2.67 micrometer (nominal 10%)

R(gold) = reflectivity of a vacuum deposited gold surface (nominally 99.4%)

R(sapphire) = 2-surface normal irradiance Fresnel reflection loss of a sapphire window in the 2.45-2.67 micrometer band (nominally 13.3%)

$R(\text{silicon})$ = 2-surface 45° incidence Fresnel reflection loss
 of a silicon beamsplitter in 2.45-2.67 micrometer
 band (nominally 0.452)

 $T(\text{vapor})$ = transmission loss at 2.67 micrometer caused
 by in beam water vapor path L (nominal 0.2 <
 $T(\text{vapor}) < 1.0000$)

 Eff = a system efficiency factor due to focusing energy
 losses (estimate at 25%, i.e. 4x losses)
 $\text{Ir}(2.45)$ = intensity (watts) received at 2.45 micrometer
 sensor

 $\text{Ir}(2.67)$ = intensity (watts) received at 2.67 micrometer
 sensor

We can then write:

$$\text{Ir}(2.45) = \text{Is}(2.45)R(\text{gold})^2 [1 - R(\text{sapphire})]^2 R(\text{silicon}) T(\text{filter}) * R(\text{gold}) [1 - R(\text{sapphire})] \text{Eff} = 5.35 \text{ milliwatts} \quad (3.27)$$

$$\text{Ir}(2.67) = \text{Is}(2.67)R(\text{gold})^2 [1 - R(\text{sapphire})]^2 [1 - Q(\text{abs})] * T(\text{vapor}) [1 - R(\text{silicon})] T(\text{filter}) R(\text{gold}) [1 - R(\text{sapphire})] * \text{Eff} = 5.52 T(\text{vapor}) \text{ [milliwatts]} \quad (3.28)$$

If the Lead Sulfide photosensor responses are as given by Equation (3.23) then the response voltage output $[V(\text{OP1})]$ can be characterized as:

$$V_{\text{OP1}} = -[10.296T_{\text{vapor}} - 0.02132] \quad (3.29)$$

where the constant terms are only approximate due to the many system unknowns such as filter bandpass shape and envelope absorption that appear in Equations (3.27) and (3.28). Ideally, a quantity T is sought so that $T = 0$ when $T(\text{vapor}) = 0$ and $T = 10.000$ volts DC when $T_{\text{vapor}} = 1.0$. This scaling and offset is accomplished by OP2 in Fig (3.15). OP2 operates on its input voltage $[V(\text{OP1})]$ to provide the gain and offset amplification:

$$T = -[V_{\text{OP1}}(R_a/R_e) + 10.000[2 RB_2/(RB_1 + RB_2) - 1]] \quad (3.30)$$

Thus under the conditions of Equation (3.29) the gain error can be removed by adjusting $R(a)$ so that $R(a)/R(c) = 10.0/10.296 = 0.971$ and setting $R(b)$ so that $T = 0.00$ when $T(\text{vapor}) = 0.00$. Then the output T is directly scaled on 0-10 volts DC as linear transmissivity.

This behavior of the circuit shown in Figure (3.15) leads to an inherent instrument self-calibration mode and calibration check capability. In Figure (3.15), remove all water from the path length using a desiccant to be described in Section (3.3.2). Adjust R(a) until the output [T(out)] reads 10.000. Close the electronic shutter SH(1), simulating a total absorption in the path [L] and adjust R(b) so the output [T(out)] reads 0.000. The two adjustments interact so repeat sequentially until the output reads 10.000 with the shutter open and 0.000 with the shutter closed. The device is now inherently and reproducibly self-calibrated and gives a direct linear readout of water vapor transmission [T] in the path [L]. Zero and span can be checked before and after flights with a portable desiccant chamber and system zero can be checked even during flight with the electronic shutter to give confidence in system stability.

The detector assembly includes the cooled Lead Sulfide detectors and their integral temperature regulation thermistors, along with the ratiometric operational amplifier circuitry. The temperature of the detectors is controlled by a temperature regulator which incorporates a switching converter to supply the thermoelectric cooler power.

The gain and offset block is a low noise and offset operational amplifier configured to remove offsets from the raw transmissivity signal and to correct the gain to a uniform level.

The calibrated transmissivity signal is converted by a analog converter to a digital format and then transmitted to a display and to any recording devices in the system. The transmission of the digital data is far preferable to transmission of analog data because of the very much higher noise immunity enjoyed in the digital domain.

3.2.4 Light Source Filament Temperature Controller

Since a light bulb dissipates energy both by radiation, and by thermal conduction, changes in the ambient conditions will generally result in changes in the temperature of the filament under conditions of constant power applied to the bulb. These changes will also be present to a greater or lesser degree when using constant voltage, or constant current drive. Since the resistance of a tungsten filament increases with increasing temperature a constant voltage drive will tend to stabilize the temperature of the filament with respect to environmental conditions while constant current drive will accentuate the errors.

In any application depending on either the intensity of illumination, or the relative magnitude of intensities at differing wavelengths, such a variation in the temperature of the filament will produce unacceptable variations in the output of the bulb.

Regulation of the filament temperature can be accomplished by monitoring the filament resistance and compensating the drive to the bulb.

Due, however, to the moderately high power required to drive the bulb, a linear regulator would be hampered by fairly high parasitic dissipation. This high dissipation will shorten device life and waste potentially expensive supply current. The design of choice is therefore a switch mode regulator which will optimize space, reliability, and power requirements. A schematic of the feedback stabilized switching lamp power supply is shown in Figure (3.16). The feedback voltage is

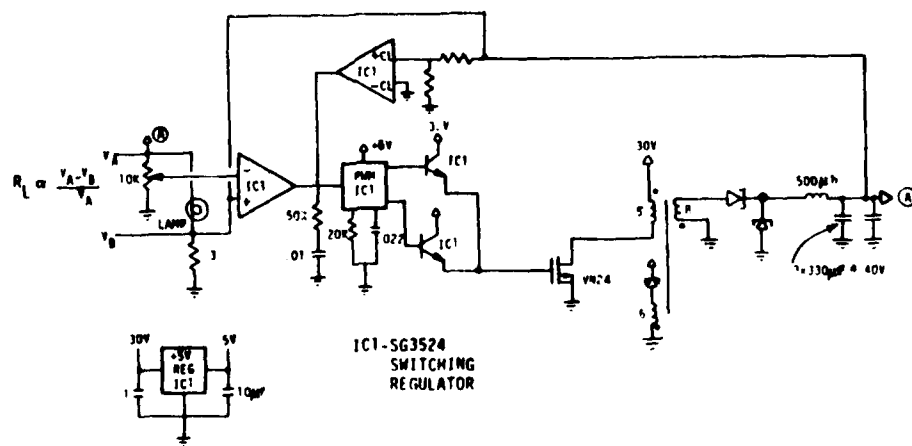


Fig. (3.16) Switching Light Source Regulator Schematic

derived from a bridge configuration which measures the deviation of the filament resistance from the ideal. This error voltage is amplified, filtered and pulse width modulated. The pulse output is applied to the bridge via a transformer coupled forward type DC to DC converter.

A schematic diagram of the filament control loop is also shown in Figure (3.16). The input is a mechanical setting on a potentiometer. This resistance ratio input is compared to the the resistance ratio formed by the lamp filament and a small reference resistance by a simple resistive bridge. This signal is then amplified by the pulse width modulator and DC to DC converter and applied back to the lamp which then converts this voltage to a temperature (by heating itself) and thus to the original resistance. There is an effective noise input at the lamp itself representing variations in non-radiative types of heat transfer.

Since the detectable response of the output of a tungsten lamp extends to nearly 1 kilohertz, the proper design of the feedback loop requires that the response of the lamp be accurately characterized. This characterization is accomplished by opening the feedback loop on the switching regulator and performing impulse response tests. The overall transfer function of both the regulator and the lamp can be derived by measuring the voltage applied to the lamp and the resistance of the lamp. Once these transfer functions are known, optimization of the feedback elements of the control loop can be accomplished.

A secondary loop is used to perform safe area limiting for the DC to DC converter. The voltage across the reference resistor in the lamp side of the bridge is used as a sample point for the output current. If the output current exceeds a preset limit, the duty cycle of the pulse width modulator is decreased. This has the effect of applying an increasingly rigid limit to the output current.

Since the ambient conditions for the light source are fairly variable, the effort to design an optimum controller is well expended. The result will be an optimum response to environmental variations and thus optimum operation of the instrument with regard to light source induced error sources.

The pulse width modulator and DC to DC converter design are conventional, with the exception of the use of resistance as the control variable.

The use of high speed MOS FET power transistors in the design permits efficient operation with a high switching frequency of about 200 kilohertz. The higher switching frequency minimizes component size and simplifies noise reduction measures.

3.2.5 Thermoelectric Lead Sulfide Temperature Control

The circuit used to cool the lead sulfide detector is a switching regulator configured to use the resistance of the on board thermistor as feedback and the Peltier array as the control element. A circuit diagram of the cooler regulator is shown in Figure (3.17).

Any deviations in the resistance of the thermistor away from the set point are amplified and cause the duty cycle of the DC to DC converter to change. The error amplifier is configured with a pole at several hundred Hertz to provide stability in the amplifier itself and yet still provide high enough response so that the thermal characteristics of the detector determine the loop response.

A secondary feedback loop prevents the voltage applied to the cooler from exceeding approximately 2 volts. This is done using the section of the regulator normally devoted to current limiting. The effect of this output limit is that under maximum cooling situations such as power up, the maximum permissible power is applied to the device, but under normal operation no limiting action occurs.

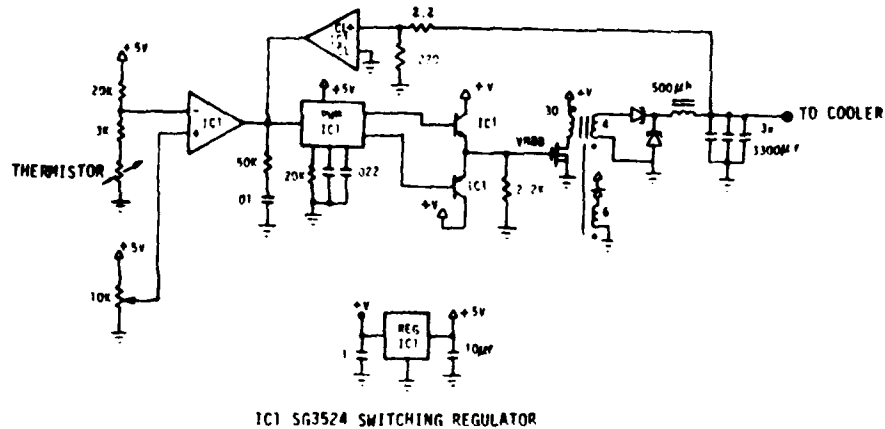


Fig. (3.17) Switching Thermoelectric Cooler Schematic

A prototype of this regulator has been built and its observed stability operating under ambient conditions with an exposed controlled region was better than 0.01° Celsius. Under operating conditions inside the Dewar flask formed by the detector enclosure, operation should be even better. Testing under transient conditions exhibited over-shoot so small as to be at the limit of detectability.

The loop gain is on the order of 30 decibels at zero frequency. This implies that the ultimate DC error in temperature of the detector is approximately 1000 times smaller than for constant voltage excitation. This loop gain can be increased to a maximum of approximately 60 db in the present design.

3.2.6 Potential Electronic Problem Areas

Many potential error sources are greatly reduced by the device self-calibration mode described in Section (3.2.3). This capability enables virtually all electronic and optical age degradations or drifts to be readily identified and corrected.

Lead Sulfide photoconductors have $1/f$ noise and exhibit less detectivity at DC than at typical chopped frequencies of about 1 KHz. Thus there could be some legitimate concern over whether the sensors will be excessively noisy at DC as proposed here. The proposed Lead Sulfide sensor has a D^* of $2.7E+9$ centimeter per root hertz per watt at 600 Hz chopping frequency. From D^* , the noise equivalent power (NEP) at a given system bandpass $[\Delta f]$ for a sensor of area $[A]$ can be computed as:

$$NEP = (A\Delta f)^{1/2} / D^* \quad (3.31)$$

For the proposed 1 millimeter square detector then, $NEP(1000 \text{ hertz}) = 1.2E-9$ watts. As shown in Figure (3.18), the direct coupled D^* will be down by about one order of magnitude and the NEP will be $1.2E-8$ watts. At $T = 0.2$ the worst case lowest incident power is about 0.6 milliwatts and the thus the $1/f$ noise level is exceeded by about a factor of fifty thousand. This is one of the luxuries of an active

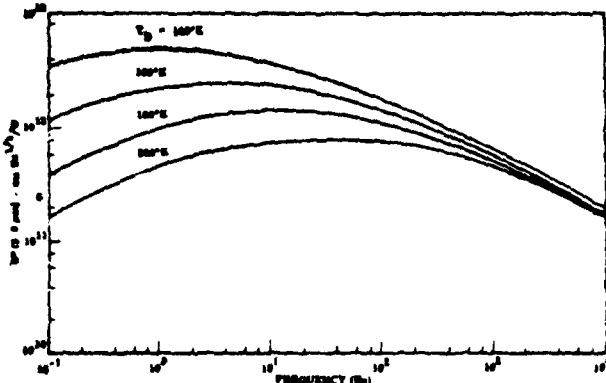


Fig. (3.18) Lead Sulfide D^* versus Chopper Frequency

light-source system where optical signal power can be increased until system low-level error terms become negligible. Preliminary tests with a Lead Sulfide DC coupled detector have confirmed this theoretical expectation that $1/f$ noise will not be a significant error term. Precedent for successful use of a similar ratiometric DC coupled technique can be found in Tomasi and Guzzi (1974).

Lead sulfide sensor temperature offset drifts were, however, confirmed as a principal error source in our laboratory tests. Detectable error signals could be caused by simply putting a warm finger on the case enclosing the uncooled, unthermostated test Lead Sulfide sensor. As discussed in section (3.2.1) sensor substrate temperature stability must be maintained to within about 0.06° Celsius to meet the

design goal of 0.1% accuracy in T . Because of the inherent self calibration features discussed in section (3.2.3), only individual temporal stability at this level is required, not absolute accuracy or even relative temperature accuracy between the two detector substrate temperatures. This makes the goal attainable. Since this stability is a critical design item, a prototype of the feedback switching thermoelectric controller has been built and tested as discussed in Section (3.2.6) and shown schematically in Figure (3.17). An open-air thermoelectric cooler with attached feedback thermistor was successfully maintained at a relative temperature stability of 0.01° Celsius so the design goal for the control specifications should be even more easily met when the thermoelectric cooler is enclosed in a factory provided hermetically sealed evacuated container as shown in Figure (3.10). Since this stability is critical to accuracy, front panel readout of Lead Sulfide substrate temperature will be provided in the prototype. Light source design temperature accuracy of 0.5% should be easily attained using a variant of the same cooling circuitry. Since the Osram lamp filament resistance at working temperature is only about 1.5 ohms, great care must be taken to avoid resistance changes in the attachment of the light bulb to the power and measuring circuit. Soldered leads rather than conventional plug-in bulb mounting sockets will probably be required. Conventional 4-wire resistance sensing techniques may also be useful.

In general, it is expected that the accuracy and stability of the electronic design will exceed that of the mechanical and optical components due to use of recently available integrated electronic amplifiers and components such as the PMI OP-27 low noise ultrastable op-amp. The major significant unknown will be long term stability of the Lead Sulfide sensors over periods of months or years. Should such drifts occur, they can however be easily detected and corrected by the self-calibrating feature of section (3.2.3).

3.3 Mechanical Design

3.3.1 Enclosures/Prototype System

The prototype design philosophy will be to configure the mechanical and optical components for easy laboratory adaptability and ability to incorporate design layout changes without major engineering effort. With this goal in mind mechanical mounting and alignment of the electro-optical components will be done on a prototyping system obtained commercially from the Newport Research Corporation.

Separate light-tight and essentially hermetically sealed enclosures will be fabricated around the light source and two-wavelength receiver. These two enclosures will be mounted on an optical rail to permit easy alignment and variation of the system path length [L]. Electronic readout and control circuitry will be in a separate enclosure connected by cable to the sensor optical heads. No attempt will be made in this prototype stage to configure the optical and mechanical elements in an aircraft mountable or aerodynamically reasonable fashion. Instead, prototype design

flexibility will be retained at this stage in the sensor development.

3.3.2 Enclosure Desiccation

The sensor self-calibration technique of Section (3.2.3) can theoretically null away the effect of a constant absorbing water-vapor density in the light source and receiver enclosures. In practice second order effects due to differing temperature and ambient pressure in the enclosures and sample path length [L], would complicate the data recovery. Internal condensation could also occur if the enclosures were cycled over wide temperature ranges. Sensible design thus calls for the water vapor to be removed from the hermetically sealed light source and detector enclosures.

There are three possible methods to accomplish this vapor removal; internal vacuum, system purge with dry nitrogen or some similar water free gas, and internal desiccants. Internal desiccants will be used to remove water vapor from the system enclosures. This is the most straightforward method and also has a number of significant advantages. Table (3.1) shows the efficiency of a number of available desiccants.

CHEMICAL SUBSTANCE	EQUILIBRIUM VAPOR DENSITY (GM/M**3)	FROST POINT (° Celsius)
Barium oxide	0.00065	-80
Magnesium perchlorate	0.002	-72
Calcium oxide	0.003	-69
Calcium sulfate (DRIERITE)	0.005	-66
Aluminum oxide	0.005	-66
Potassium hydroxide	0.014	-58
Silica gel	0.030	-52
Magnesium perchlorate	0.031	-52
Calcium chloride	0.360	-30
Sodium hydroxide	0.80	-21
Barium perchlorate	0.82	-21
Zinc chloride	0.98	-19
Calcium chloride	1.25	-16
Copper sulfate	2.80	-7

TABLE (3.1) DESICCANT EFFICIENCIES

Compared with other known chemical standards DRIERITE has been shown to lie between phosphorus pentoxide and concentrated sulfuric acid in drying efficiency. DRIERITE possesses much more desirable physical properties than desiccants which exceed or approach it in efficiency, and has a higher capacity than those which most closely approach it otherwise.

For example, it is about six times as efficient as the commonly used silica gel. Also DRIERITE can be obtained commercially with a color change indicator to warn of desiccant depletion. Each optical chamber will be purged through a DRIERITE air desiccant column as shown in Appendix I and will also enclose a DRIERITE capsule with the color indicator visible through a sight window as a fail-safe indicator. Thus small gas leaks in the chamber will be compensated by the internal DRIERITE absorption and an absolute hermetic seal is not essential as would be the case in a vacuum or inert gas purge system.

3.3.3 Zero and Span Calibration

As discussed in Section (3.2.3), setting the instrument self-calibrating zero and span adjustments requires a method of removing water vapor from the path length $[L]$. Vacuum techniques, dry purge gases and desiccant dried air could be used. DRIERITE dried air at a residual vapor density of 0.005 grams per cubic meter and a path length $[L] = 20$ centimeters would yield a transmissivity, $T = 0.953$. Thus a simple DRIERITE drying tube providing air to an open ended tube placed in the sample path length $[L]$ can provide a calibration standard for adjusting the purged air T reading to 0.953. This permits the reproducible calibration cycle of Section (3.2.3) to be readily accomplished in practice. Removing all vapor to a $P(r)$ of $1.0E-11$ centimeters precipitable depth to attain a purged T of 0.999 is impractical, even with an inert carrier gas, but not necessary to the calibration cycle since the DRIERITE purge system provides a reproducible test point.

3.3.4 Potential Mechanical Problem Areas

The most significant mechanical design problems of this prototype sensor are expected to arise in the areas of internal baffles to reduce stray light from the intense broad-band light source and insure solar-blindness to both the sun and other potential external light sources. It is possible that additional long-pass filter elements may be useful at the apertures of the light source exit and receiver entrance optics. The more difficult mechanical design problem of adapting the sensor to airborne use meeting FAA and MIL.SPEC. specifications is not a part of this laboratory prototype design contract and will be deferred until a functioning sensor has been demonstrated in the laboratory.

4 AIR TEMPERATURE RADIOMETER

4.1 Optical Design

The complete expression for radiative transfer in a partially absorbing gas layer where absorption and also emission takes place is given by the Schwarzschild Equation which can be written in differential form as:

$$\frac{\partial I_\lambda}{\partial u} = -k_\lambda (I_\lambda - I^*_\lambda) \quad (4.1)$$

The radiation absorbed over an infinitesimal optical thickness [du] is expressed as $k(\lambda)I(\lambda)du$. By Kirchoff's Law, local thermodynamic equilibrium requires that the absorptivity and emissivity are equal and thus the thermal emission at the same layer du is $k(\lambda)I^*(\lambda)du$, where $I^*(\lambda)$ represents the black body monochromatic intensity as given earlier in Equation (1.21). Therefore the differential intensity change is given by Equation (4.1) which can be integrated if the temperature and the absorption coefficient $k(\lambda)$ along the beam path are known.

In Section (3.0) an actively illuminated transmissometer sensor for measuring water vapor transmissivity over a fixed path length [L] was discussed. At that device's 2.67 micrometer active wavelength, thermal emission from substances at tropospheric temperatures is negligible in relation to the intense 150 watt, 2000° Kelvin tungsten light source. $I^*(\lambda)$ in Equation (4.1) can thus be ignored and Equation (4.1) reduces to the differential form of the Beer-Lambert Absorption Law that forms the basis for the theory of transmissometer measurements of attenuating gas densities.

In this section, a passive sensing air temperature sensor based on the second $I^*(\lambda)$ term in Equation (4.1) will be discussed. By looking into a strongly absorbing gas (carbon dioxide at 4.265 micrometer) external light sources at reasonable distances will be attenuated to negligible values before reaching the sensor and thus $I(\lambda)$ in Equation (4.1) can be equated to zero. Under these assumptions, Equation (4.1) reduces to the differential form of Equation (1.20) which forms the theoretical basis for radiometric measurement of air temperature.

Two complications are readily apparent in this passive radiometric air temperature measurement. First, since $I^*(\lambda)$ is fixed by the gas temperature according to Planck's law, the luxury of improving instrument signal/noise ratio by increasing the intensity of an external light source as was done in the absolute humidity transmissometer sensor is not possible. Further, at tropospheric temperatures, one must deal with carbon dioxide band infrared irradiance signals of about 0.01 microwatt. This is about 100,000 times smaller than the transmissometer signal levels of section (3.0). Second, this small signal will be imposed on a background of infrared emission from the instrument housing and local surroundings. This background will vary with housing temperature and be of the same order of magnitude as the sensor signal if the housing is at tropospheric temperatures. The situation is somewhat analogous to operating an optical instrument in a glowing red-hot enclosure. The following sections will discuss methods for dealing with these two engineering problems, low signal level and significant background signal contamination.

4.1.1 Wavelength Selection

The radiometric sensor will operate at a design wavelength of 4.265 micrometers with a filter bandpass of 0.1 micrometer nominal. This will result in the approximate temperature weighting function given as Equation (1.25) and shown in Figure (1.10). This is the most intense available carbon dioxide absorption band and should result in over 50% of the sensor temperature weighting function coming from distances less than one meter from the sensor window.

4.1.2 Aperture and Field of View Tradeoffs

Radiometric sensors viewing extended sources filling their field of view have the non-intuitive property that the signal level they receive is dependent only on the system aperture or F/number. As shown in Figure (4.1) a sensor of area $[a]$ and an acceptance aperture of Ω steradians viewing an isothermal source filling the beam will receive the same signal irradiance regardless of the intervening optical chain. Thus the optical chains shown in Figures (4.1a) and (4.1b) have the same signal strength. Also, if the lens shown in Figure (4.1a) were replaced by an open aperture of the same area $[A]$, the signal strength received from an isothermal gas would be unchanged. The sensor field of view $[w]$ in steradians and the window aperture $[A]$ can be traded off according to the relation:

$$Aw = a\Omega \quad (4.2)$$

The only way to increase the signal is by increasing the sensor area $[a]$ or its acceptance angle Ω . Since Ω can never exceed 2π steradians and a is limited to about 5 millimeter square or less, sensor signal is limited by system F/number regardless of the optical chain employed. A more detailed discussion of this behavior can be found in Astheimer (1962) or Harrison (1960). The device described here will have a geometry as shown in Figure (4.2). Windows and filters are readily available in two inch diameters and this is the simplest mechanical layout consistent with the requirement that accepted radiation impinge on the filter normal to its surface. There are other advantages to a collimated acceptance beam. Sample volume is more consistent with the cylindrical absolute humidity sensor sample volume and calibration is facilitated by the well defined beam. In a possible later development to be described in the final report, a collimated beam temperature sensor could also theoretically be configured with a well defined sample volume exactly equal to that of the absolute humidity sensor.

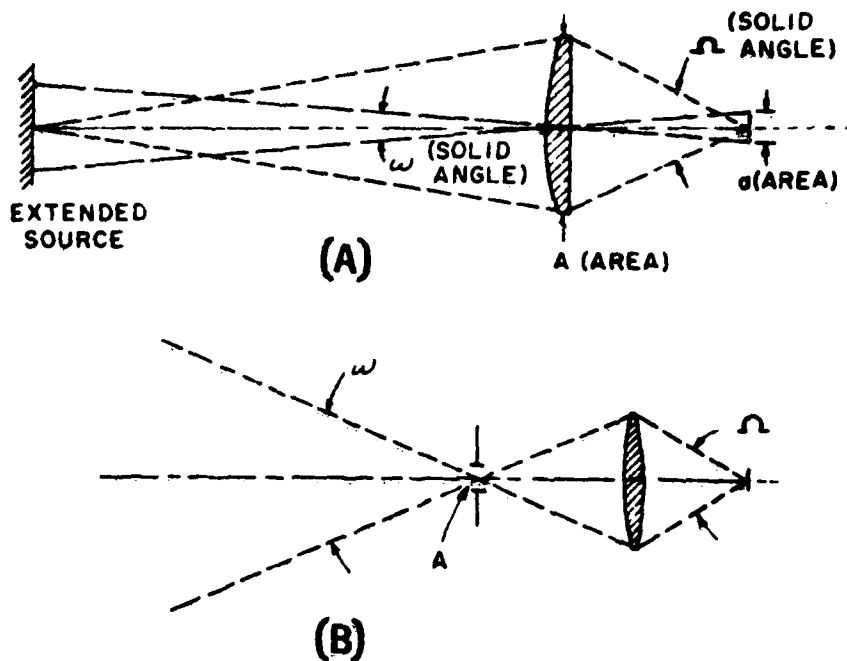


Fig. (4.1) Sensor Aperture and Field-of-view Relations

4.1.3 Focusing Optics and Aperture Stops

The same off-axis parabolic mirrors shown in Figures (3.7) and (3.8) will be used as the focusing optics of Figure (4.2). As shown in Figure (3.7), the off-axis full acceptance angle is 78 degrees from a 1.3 inch diameter beam. System effective F-number is thus 0.617, far higher than can be reasonably achieved by conventional refractive optics.

The system aperture stop is the detector active surface itself. For a 1 millimeter square detector, acceptance beam divergence according to Equation (4.2) is thus about 1° . If the total hemispherical irradiance that could be received by a Lambertian sensor viewing 2π steradians of gas is denoted by $W(2\pi)$ and the system acceptance aperture half-angle is Φ , then actual received irradiance [$W(a)$] is given as:

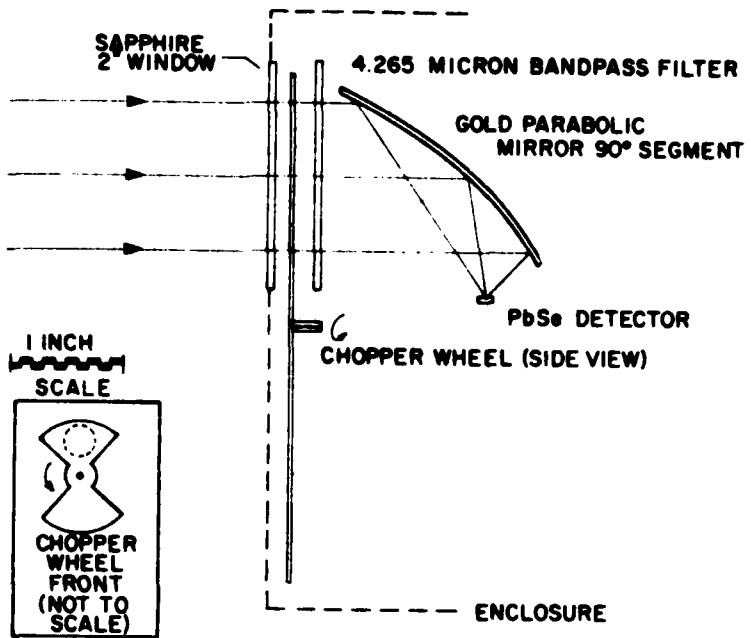


Fig. (4.2) Temperature Sensor Optical Diagram

$$W_a = W_{2\pi} \sin^2 \theta \quad (4.3)$$

The system of Figure (4.2) has an acceptance half-angle of 39° and thus is 40% efficient in capturing the maximum available hemispherical irradiance signal. This is more than 2.5 times the signal level of a more conventional refractive optical system with a maximum practical F-number of about 1.2.

4.1.4 Narrowband Infrared Filter

The general discussion of bandpass filter characteristics given in Section (3.16) also applies here. As discussed in Section (1.4) and Section (4.1.1), the filter center wavelength will be 4.265 micrometers and the filter bandpass will be 0.1 micrometer nominal. This is an order of magnitude larger than the water vapor filter bandpass and is made possible by the broader nature of the carbon dioxide absorption peak. This is fortunate for it permits an order of magnitude increase in received signal power. Near-band and out-of-band filter transmission of the prototype 4.265 micrometer filter is given in Appendix I. Note

that the out-of-band rejection is everywhere better than 99.9% and averages better than 99.99%.

4.1.5 Instrument Thermal Emissions

As discussed in Section (4.1) instrument thermal emissions at 4.265 micrometers will be order of magnitude comparable to the atmospheric irradiance signal level. Not all of the instrument emissions will be intercepted by the filter and thus broad band thermal background emissions will reach the detector. As shown in Figure (1.7), the unfiltered instrument emission peak at about 10 micrometers is one or two orders of magnitude stronger than the 4.265 micrometer signal and occurs over a bandpass about two orders of magnitude wider.

At first glance it seems that this long-wavelength background emission would be about 10,000 times stronger than the signal and thus swamp it out beyond recovery, even with lock-in techniques. This is indeed the case for most conventional infrared radiometer sensors such as thermistor bolometers, thermopiles, and pyroelectrics and may explain why a 4.265 micrometer short wavelength carbon-dioxide air temperature radiometer has apparently never been implemented.

However quantum sensors such as the thermoelectrically cooled lead selenide detector proposed here are spectrally selective and do not respond to all wavelengths equally. For reasons discussed in Section (3.2.1), they exhibit a very sharp long-wavelength cut-off to low-energy photons.

Figure (4.3) illustrates this relative Lead Selenide spectrally sensitive efficiency, the relative black-body emission of an instrument housing at 300° Kelvin, and the resultant detector spectral sensitivity to this background thermal emission. Because of the sharp short wavelength cut-off of the instrument thermal emission coupled with the quantum sensor rapid long wavelength cut-off, the Lead Selenide sensor at 4.265 micrometers should actually exhibit lower relative levels of background signal than the conventional 14.8 micrometer thermal bolometer sensor reported and used on an aircraft by Albrecht et.al. (1979).

4.1.6 Photo-Chopping Signal Modulation

In spite of the above detector spectral selectivity, background signal due to instrument emissions and detector substrate temperature will still be larger than the atmospheric irradiance signal. This background will be removed via the conventional technique of periodically interrupting the atmospheric irradiance signal with a rotating chopper wheel as shown in Figure (4.2). The AC component of the chopped signal is thus the atmospheric signal and the DC component is the variable thermal background offset. The chopper wheel is located as close as possible to the entrance window to minimize stray unchopped

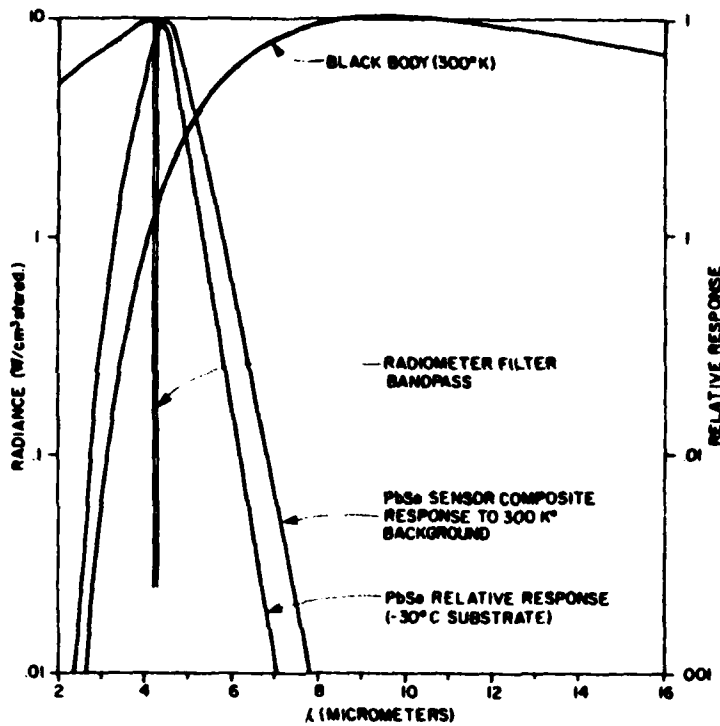


Fig. (4.3) Lead Selenide Spectral Background Selectivity

background signal. Since the filter has a low transmissivity of only about 40%, the chopper must be ahead of the filter to achieve accurate results.

This constraint, added to the requirement that the incident light on the filter be collimated and normal to its surface, requires that the chopper be placed in a large aperture beam as shown in Figure (4.2). Therefore, chopper edge transitions are not sharp as would be the case with more conventional focal point chopping. These slow edge transitions are dealt with in a novel synchronous demodulation scheme to be discussed in Section (4.2). Second order effects such as chopper thermal emission and window reflectivity effects are also discussed in that section.

4.1.7 Window Materials

Since the system window required for practical airborne use is prior to the chopper in Figure (4.2), it is essential that the window be transparent at 4.265 micrometers, so that its thermal emissions are negligible. This condition is extremely well met by a sapphire window as discussed at length in Section (3.1.1). The sapphire two surface Fresnel reflection loss will reduce the atmospheric irradiance signal by about 14% and contaminate it with a 14% reflection inside the instrument enclosure. The important point is that these will be shown in Section (4.2) to be constant offsets independent of the window temperature and thus removable.

4.1.8 Solar Blindness

At the chosen sensor wavelength of 4.265 micrometers ± 0.05 micrometer, the atmospheric absorption will be 99.9% in about 15 meters as illustrated in Figure (1.10). The solar beam passing through many kilometers of atmosphere is essentially perfectly absorbed before reaching the sensor and the sensor is therefore totally solar-blind.

4.1.9 Potential Optical Problem Areas

The major potential problem area in the optical design layout involves effectively removing the slowly varying instrument thermal emission background from the desired atmospheric signal. A number of second order effects must be electronically compensated as discussed in Section (4.2). As shown in Section (2.2) the full utilization of the design goal absolute humidity accuracy in calculating saturation ratio and supersaturation would ideally require a temperature sensor absolute accuracy of 0.1° Celsius. It can be immediately predicted that removing instrument thermal background emissions to this absolute accuracy level will be a much more difficult task than achieving a sensor precision of higher levels such as 0.02° Celsius. This will be by far the most difficult air temperature radiometer design problem.

4.2 Electronic Design

4.2.1 Thermoelectrically Cooled Lead Selenide Photodetectors

The detailed discussion of the behavior of quantum detectors from Section (3.2.1) also applies to the lead selenide detector used in the air temperature radiometer. Lead selenide differs from lead sulfide in having a longer wavelength spectral response peak near 4.3 micrometers as shown in Figure (4.3) and an effective responsivity about one order of magnitude lower. Representative device parameters for a lead selenide 1 square millimeter detector stabilized at -30° Celsius are:

$R(\text{dark})$ = 1.0 megohms
 Size = 1 square millimeter
 V = 50 volts
 R = 8E+4 volts/watt
 $R(\text{load})$ = 1.0 megohm
 D^* = 1.4E+10
 $\text{NEP}(1000\text{hz})$ = 2.25E-10 watts

From Equation (4.8) the device conductivity as a function of incident 4.265 micrometer light power (watts) is thus:

$$C = 1/R = 6.4E-3 W + 1.0 E-6 \quad (4.4)$$

As discussed in Section (1.4), it is reasonable to expect black body irradiance from the atmosphere at tropospheric temperatures, through a 4.265 micrometer filter and a 0.1 micrometer bandpass into an F/number = 0.6 optical system to produce an optical signal of 0 to 6 microwatt at the above detector.

It can be immediately seen that this signal is small in relation to the background dark level. The detector will be biased and amplified as shown in Figure (4.4). This active bias technique is chosen in preference to the conventional passive bias of Figure (3.13) since it produces an output linear in incident irradiance. This linearity is

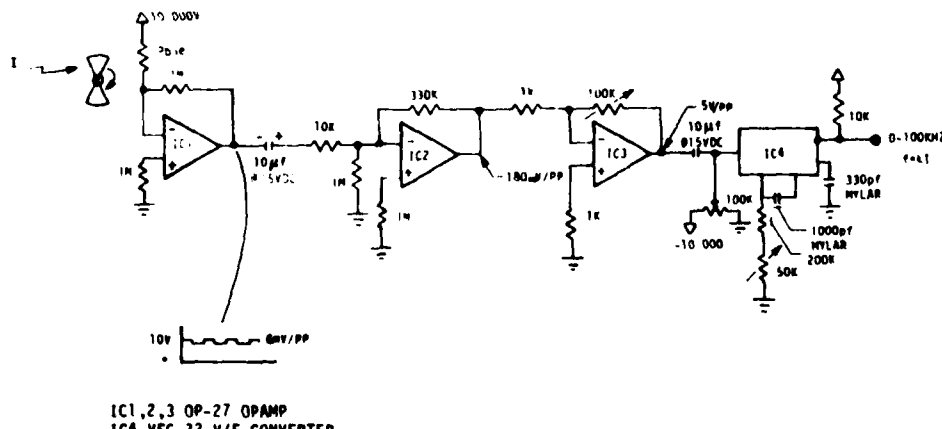


Fig. (4.4) Lead Selenide Low-level Amplifier Schematic

achieved at the expense of added noise from the first stage operational amplifier. This Precision Monolithics OP-27 operational amplifier is a recent introduction with the phenomenal noise figure of 0.3 nanovolt per

root hertz and thus does not add significant noise to the low level detector output. Its offset drift is similarly low at 0.2 microvolt per° Celcius and 0.2 microvolt per month but these specifications are not strictly necessary due to the AC coupling between stage one and stage two of Figure (4.4). Signal levels are at about 0.06% of voltage bias and thus synchronous chopping is needed to remove slow baseline drifts in bias resistors and passive components even though the ultra-low-noise precision op-amp is extremely stable itself. Also the full scale 6 millivolt electrical signal level will be equalled by a substrate temperature drift of only 0.03° Celcius. This explains why a dual matched sensor approach as in the absolute humidity module cannot be used in this low signal level application. Substrate thermoelectric temperature control is simply not accurate enough to eliminate drifts between the two sensors. However chopper modulation of the incoming light at about 1 kilohertz and synchronous demodulation readily removes these slow baseline drifts.

Therefore due to the very low signal levels in the radiant thermometer, the incoming radiation is chopped. The detector is presented alternately with the thermal radiation from the chopper wheel itself and with the incoming atmospheric radiation.

The 14% sapphire Fresnel reflection of the incoming atmospheric radiation, the similar 14% internal window reflection during the chopper open period, and the imperfect emissivity of the chopper wheel are compensated for in the system by using a selectable effective emissivity for the chopper wheel and a composite gain applied to both signals. These quantities are used in preference to signals more reflective of physical quantities in order to simplify the subsequent processing.

The lead selenide detector is cooled by a thermoelectric cooler and power supply similar to that used for the detectors in the hygrometer. The chopped AC output signal from the detector is amplified as shown in Figure (4.4) and converted to a proportional frequency by a precision voltage controlled oscillator (VCO). This frequency is processed by a set of counters which perform correction for the radiation from the chopper wheel. Processing this signal in terms of frequency counted pulses in the digital domain is advantageous primarily due to the decreased problems with circuit stability and increased facility of complex processing since the Planck's radiance law is very monlinear and not easily synthesized by analog components.

The output of the counters at the conclusion of a processing cycle represents directly the incident radiation from the carbon dioxide atmospheric black body external to the thermometer. Artifacts of optical imperfections, variable reference, and variable baseline are removed from the data at this point as will be discussed in detail in the following sections.

4.2.2 Synchronous Chopper Driver

As shown in Figure (4.5) the chopper blade is driven by a standard DC permanent magnet motor (M) which is controlled by a one megahertz crystal reference which is divided down to provide control signals for the signal processing counters.

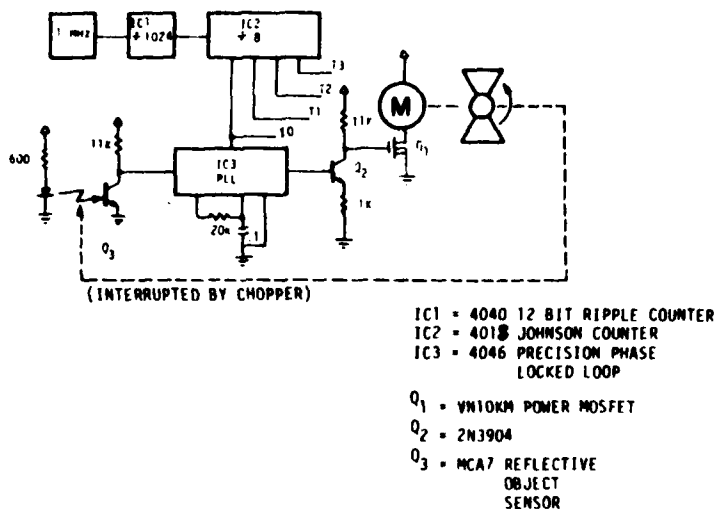


Fig. (4.5) Photchopper Phase-Locked Driver Schematic

The phase locking of the chopper blade to the internal crystal based reference is done with a high precision complimentary metal oxide semiconductor (CMOS) phase locked loop. The variable frequency oscillator feedback function is accomplished by the blade motor and associated drive electronics.

The phase comparator used in the phase locked loop is a special design which utilizes a state machine to drive a tri-state output high or low in the time period between the rising edges of the input waveforms. If the reference input rises before the comparison input, the output is driven high, and if the comparison input rises before the reference it is driven low. At times other than between the rising edges, the tri-state output is left in the high impedance mode. This type of phase comparator does not permit locking to harmonics and results in zero phase offset error after lock. These characteristics are vital in a motor controller whose initial conditions are zero motor speed.

The RC filter network only provides secondary poles for the transfer function; the primary determinant of the system response is the response of the motor. The RC filter can, however, be used to modify the overall loop gain.

After division by 1024 and 8 to a basic frequency of 122.07 hertz, the following Johnson counter is also used to generate a four phase clock with timing relationships T_0 , T_1 , T_2 , and T_3 as shown in Figure (4.6).

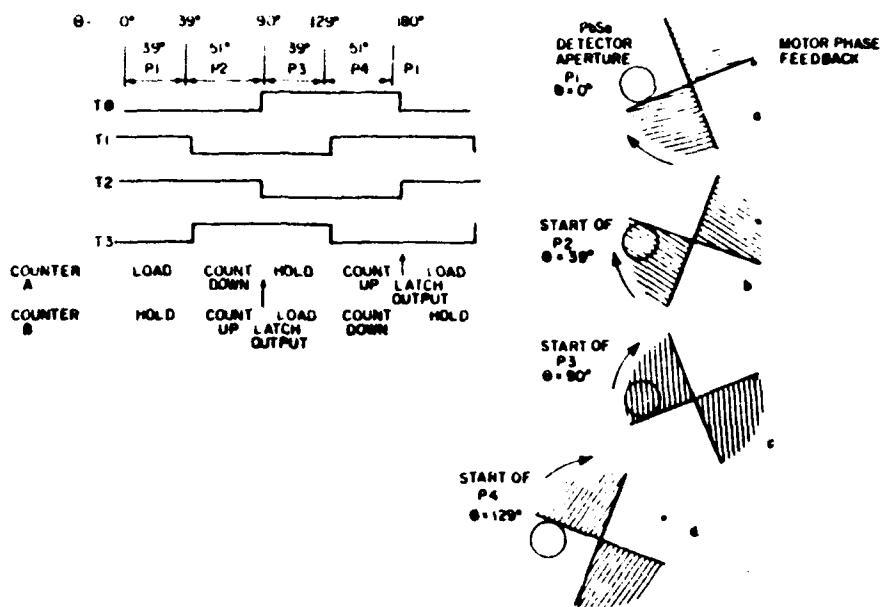


Fig. (4.6) Photochopper Timing Diagram

The motor driven chopper wheel periodically interrupts a reference light beam from a light emitting diode to yield a signal indicating chopper position, phase, and rotation rate. The phase locked loop (PLL) adjusts the motor speed to both phase and frequency lock the rotating chopper wheel to the crystal derived reference frequency. In this manner a chopper rotation rate of 3662.109 revolutions per minute with a long-term stability of 0.01% is attained. The rotation of the blade can be divided into distinct time periods as represented in Figure (4.6).

The first period, (P1), begins as the chopper wheel first impinges on the detector aperture. Period (P1) is a transitional time during which the signal is not purely from the chopper wheel or the region under test since the chopper is in a collimated one inch diameter beam far from a focal point as shown in Figure (4.2). This time is used to preload counters with the derived intensity of illumination from the chopper. The second time period (P2) begins when the detector is completely covered and the signal is purely from the interior of the instrument. During (P2), the counters count down at a rate proportional to the incoming signal. Period (P3) is the transitional period from covered detector to fully uncovered detector. Since the profile of the uncovering is unknown, the counters are disabled during this time. During (P4), which represents the time when only the external signal is being detected, the counters increment at the rate determined by the signal voltage as converted to frequency by the high-stability voltage controlled oscillator (VCO) shown schematically in Figure (4.4). The VCO data sheet is given in Appendix I.

One complete cycle represents 180° of rotation of the chopper blade. Due to the symmetry of the blade, a mirror image set of cycles is produced by the other side of the blade. The complete (P1,2,3,4) cycle, therefore, can be considered to occur at twice the blade rotation rate of 3662.109 rotations per minute.

4.2.3 Digital Synchronous Demodulator

The output of the detector is AC coupled and biased to coincide with the input range of the high speed monolithic voltage to frequency converter shown in Figure (4.4). This operation eliminates any problems involving the actual DC baseline of the detector.

The problem of separating the level of the internal radiance and the level of the external radiance still exists. The optimum detector for finding the level of the stable portion of a chopped signal such as that found in the radiant thermometer is an arithmetic mean of the signal over the stable period. This is inherently the function accomplished by a gated counter driven by a frequency proportional to the input signal. Electronic circuitry to accomplish this true arithmetic averaged signal demodulation is shown in Figure (4.7).

Given that the preloaded value of the presetable up-down counters shown in Figure (4.7) is (C1), then the number contained in the counters during (P3) is given by:

$$C_3 = C_1 - b k s_1 \quad (4.5)$$

where k is a factor describing the composite gain of the optical input and the electronic amplification and frequency modulation, b is an effective emissivity of the chopper blade and, s_1 is the emission of the blade and surroundings.

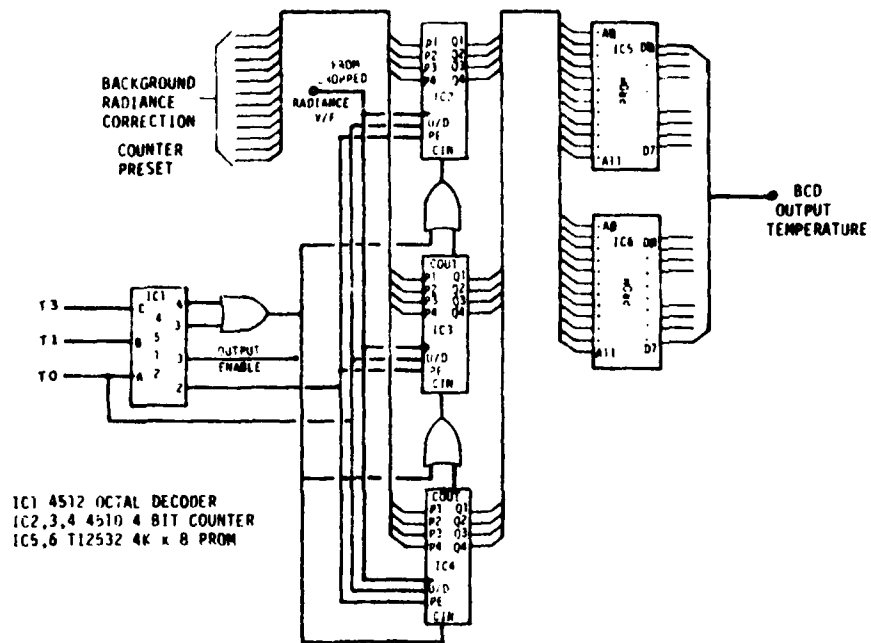


Fig. (4.7) Irradiance Signal Lock-in Demodulator

The value in the counters at the end of (P4), then is

$$C_4 = C_3 + k s_2 \quad (4.6)$$

where k is the same optical gain, but s_2 is the signal from the exterior of the instrument. Overall, then,

$$C_3 = C_1 - b k s_1 + k s_2 \quad (4.7)$$

If the value C_1 is derived from the temperature of the interior of the box so as to coincide with the expected value of $b k s_1$, then the final value of the counters becomes,

$$C_4 = k s_2 + e(s_1, t) \quad (4.8)$$

where the $e(s_1, t)$ is an error function composed of the uncompensated portion of $b k s_1$ and the noise introduced in processing.

At the end of each full cycle the composite effect of the unknown chopper emissivity (about 0.92) and the internal sapphire Fresnel reflections during the chopper open period (about 0.14) is to determine the effective internal instrument emissivity [b] used in presetting the counters with the value C1 based on the internal chopper temperature and the grey-body approximation to the Plank Radiance Law. The 14% atmospheric signal Fresnel reflection loss is constant and allowed for in the programmable read only memory (PROM) look-up table.

Since the processing counters are only 12 bits long, it seems conceivable for them to overflow during the subtraction operation due to the way that the input to the voltage to frequency converter is biased. However, no matter what the actual inputs are, they will be centered on the mid-point of the input range. Thus, if the maximum frequency of the voltage to frequency converter is selected to provide a near full scale reading in the counters, and if the difference between the radiance signals due to the maximum possible temperature and the minimum temperature does not exceed the full scale range of the voltage to frequency converter then no overflow can take place.

The update rate for the external temperature could be doubled by operating two sets of counters out of phase. One set of counters is operated as described and the other set is loaded during (P3) instead of during (P1). This means that the second set of counters will produce an output at the beginning of (P3). This could provide an independent sample update of temperature every four instead of eight milliseconds.

If even higher output response speed is required, then more sophisticated measurement techniques could provide continuous output. If two detectors are placed at 90° to each other with reference to the center of the chopping wheel, then the obscured and non obscured time periods will be exactly out of phase. Since the entropy of the reference signal is fairly low, an ensemble of digital circuits or a microprocessor could perform the averaging operation to determine the background reference, and then during the non obscured period (P4 or P2) depending on the detector) sample the signal output at high speed, subtracting the background reference on the fly. This method would provide a continuous stream of corrected samples since the streams from the detectors would consist of complementary bursts of data. The ultimate throughput of such a scheme would be limited by the response of the detector which is about 25 microseconds.

Such maximized sample rates would be largely of interest for radar and infrared structure function and propagation studies where refractive index fluctuations on the order of half the system wavelength are of great importance. Signal to noise ratio degradation according to Equation (3.31) and sample volume reduction would also have to be considered at such high bandwidths.

In this prototype development, only a single set of up-down counters will be implemented as shown in Figure (4.7) with a resultant sample update every eight milliseconds.

4.2.4 Reference Synthesis from Internal Temperature

The monochromatic radiant power from a grey body is given by Equation (4.9) where k and c are constants.

$$I = c / [\exp(k/T) - 1] \quad (4.9)$$

Since at the temperature of interest, $\exp(k/T) \gg 1$, we have approximately,

$$I = c \exp(-k/T) \quad (4.10)$$

The output of a linear band gap temperature sensor inside the instrument housing is therefore such that $\ln(I)$ is linear in $1/T$.

$$1/T = 1/k[\ln(c) - \ln(I)] \quad (4.11)$$

The emissivity factor $[\ln(c)]$ is thus an offset constant in Equation (4.11) and the effects of fixed but unknown chopper emissivity and window internal Fresnel reflections are dealt with by manipulating this linear offset constant.

The above equation is embodied directly in the hardware used to derive the expected radiance to be used as a preset for the correction counters shown in Figure (4.8). The current output of a linear temperature sensor reading the chopper temperature is offset and converted to a frequency proportional to temperature by IC(3). The counter chain (IC4,5,6) is clocked by a stable one megahertz signal for a time duration set by the period of the temperature linear VCO frequency and then latched. This results in a latched stable digital output inversely proportional to enclosure baseline temperature. Enclosure emissivity offset is accomplished by presetting these counters with a hexadecimal thumbwheel calibration switch. Background radiance is then determined from this emissivity corrected digital output in the PROM's (IC7,8) and latched by the counters (IC9,10,11). The resulting 12 bit digital output representing the chopper blade radiance as adjusted for blade emissivity and Fresnel window reflections forms the background radiance counter preset digital word for the demodulator of Figure (4.7). This enables its output to read true air temperature directly in ° Kelvin or ° Celsius regardless of enclosure and background drifts.

4.2.5 Non-linear Conversion of Radiance to Temperature

The output of the counters in Figure (4.7) thus represents purely the radiance entering the thermometer. This radiance is related to the black body temperature according to Equation (4.11) where c is fixed by calibration and k is derived from the Planck's formula. Once scale and offset errors are removed from I , this conversion can be accomplished

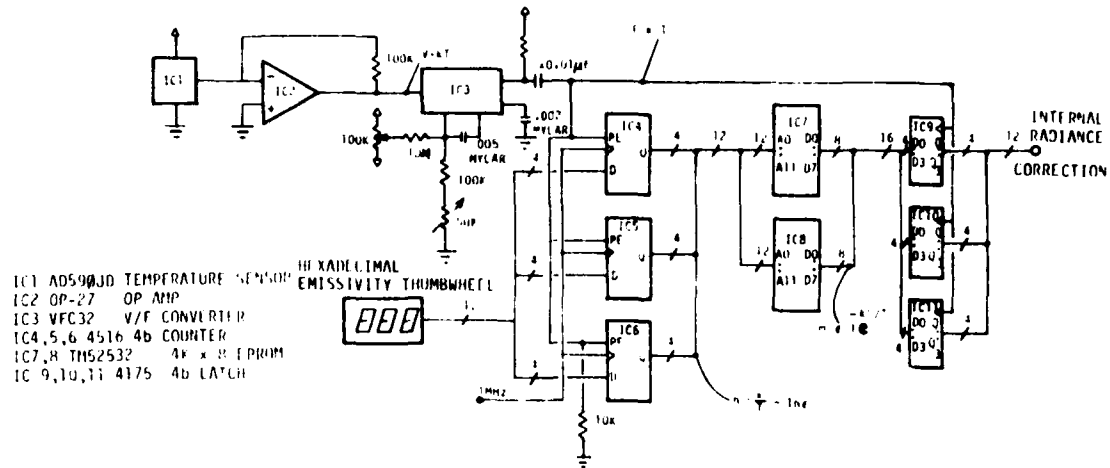


Fig. (4.8) Temperature-Irradiance Converter Schematic

without reference to anything but physical constants. A lookup technique is thus appropriate. In the radiant thermometer this conversion is performed by a set of programmable read only memories (IC5 and IC6 in Figure(4.7)) which are programmed so that the 12 bit binary input representing atmospheric signal radiance is converted to four binary coded decimal digits representing absolute temperature. The lookup table design approach performs the non-linear correction and conversion to binary coded decimal in one step without the cumbersome analog hardware which would normally be needed to do the conversion from a more conventional lock-in amplifier output stage.

4.2.6 Potential Electronic Problem Areas

Many electronic drift error sources in the conversion of atmospheric radiance to temperature are eliminated by chopping, synchronous demodulation, and the use of digital look-up tables rather than analog circuits to derive temperature from the nonlinear Planck Function.

Primary electronic difficulties will be in the layout and grounding practice required to operate a microvolt level sensor in the presence of high frequency digital noise from the counter logic and motor controller. This should not be insurmountable since conventional thermocouples with even smaller voltage outputs are routinely used in electrically noisy industrial environments.

4.3 Mechanical Design

4.3.1 Enclosures and Prototyping System

Enclosures, prototyping system components and design philosophy will be identical to that of the absolute humidity mechanical design as described in Section (3.3).

4.3.2 Carbon Dioxide Emissions in Enclosures

In the two-wavelength absolute humidity sensor, provision was made to remove water vapor from the sensor enclosure to minimize potential interference to the sample volume absorption. In this carbon-dioxide band temperature sensor, the analogous operation would be to attempt to remove carbon dioxide from the sensor enclosure; a much more difficult task. However, by mounting the chopper of Figure (4.2) very close to the system entrance window, all internal gas emissions are chopped and thus eliminated by the AC synchronous demodulation. Sensor enclosure purging thus becomes unnecessary, simplifying the mechanical design. Since carbon dioxide is a constant mixing ratio atmospheric component, second order effects should also be minimized.

4.3.3 Potential Mechanical Problem Areas

The only significant mechanical problem area is expected to be the need for devising a light and infrared tight system of internal baffles to eliminate strong light and reflection as discussed in Section (3.3.5).

5 SUPERSATURATION SENSOR DESIGN SUMMARY

Section (1) of this report has detailed the end-user utility and theory of an atmospheric absolute humidity, true-air temperature, and supersaturation sensor potentially suitable for airborne use in condensing, cloudy, sub-freezing environments where current sensors are impractical and inaccurate. Section (2) presented a brief overview of the instrument functional design. Sections (3) and (4) gave detailed, optical, electronic and mechanical preliminary prototype design philosophy and information for the absolute humidity and true-air-sensor subsystems respectively. The resultant summarized design goals and intended specifications are tabulated below for quick reference.

5.1 Absolute Humidity Sensor Design Specification Goals

Pathlength = 20 cm nominal
Range [T] = (0.2 < T < 0.95)
Accuracy [T] = 0.1%
Dynamic Range = 0.01 to 50 grams per cubic meter (3.5 orders of magnitude)
Accuracy = 2% of reading over full range
Accuracy = 1% of reading above 0.1 grams per cubic meter
Source Temperature = 2000° Kelvin nominal
Source Temperature Stability = 0.5%
Sensor Substrate Temperature = -30° Celsius nominal
Sensor Substrate Temperature Stability = 0.06° Celsius
Irradiance Signal Bandpass = 2.67 micrometer \pm 0.005 micrometer
Irradiance Reference Bandpass = 2.45 micrometer \pm 0.005 micrometer
Irradiance Reference Bandpass = 2.45 micrometer \pm 0.005 micrometer
Signal Response Time (1/e) = 2 ms

5.2 Air Temperature Radiometer Design Specification Goals

Sample Path Length = 50% weighting from first 1 meter of path
Temperature Dynamic Range = (-50° Celsius < T < 50° Celsius)
Temperature Resolution = \pm 0.02° Celsius
Absolute Accuracy Goal = \pm 0.1° Celsius
Lead Selenide sensor substrate temperature = -30° Celsius nominal
Substrate Temperature Stability = 0.06° Celsius
Irradiance Signal Bandpass = 4.25 micrometer \pm 0.05 micrometer
Sensor Signal Output (before amplification) = 50 microvolt/° Kelvin nominal
Chopper frequency = 950 RPM nominal
Chopper stability = Phase Locked 0.01% (long term)
Jitter = 2% or less
Signal Response Time = 8 milliseconds

6 PROTOTYPE HARDWARE FABRICATION

Laboratory proof of concept prototype hardware implementations of the 2.67 micrometer Absolute Humidity Sensor described in Section (3) and the 4.25 micrometer Air Temperature Radiometer described in Section (4) have been fabricated at Ophir Corporation and demonstrated at the Air Force Geophysics Laboratory. These prototypes as fabricated under the subject contract were specifically intended to prove the validity of the physics and electro-optical design of the two sensors in a laboratory environment. They are thus designed for easy modification in the course of laboratory experimentation and optimization and to make maximum use of available off-the-shelf infrared optical prototyping systems and equipment.

In pursuit of this contractual goal of cost effective proof of concept verification in a laboratory environment, we have made design compromises that render the prototypes far less than optimally designed for use in the field and airborne environments. We intend to specifically redesign and construct field and airborne qualified versions of these sensors incorporating design refinements from the laboratory prototype testing process and are actively seeking contractual support for this follow-on development from AFGL and other agencies and funding sources.

This field and airborne qualified next generation of the sensor development will be greatly reduced in size and weight via custom mechanical engineering and elimination of bulky optical prototyping system hardware. Large reductions in power consumption are also feasible. Detailed next-generation engineering changes will be proposed in a later section. Sections (6.1) and (6.2) will document the currently existing first-generation laboratory proof of concept prototypes.

6.1 Absolute Humidity Sensor Laboratory Prototype

The laboratory implementation of the differential transmissivity absolute humidity sensor is configured as an electronics and readout box attached by cable to a remote sensing head. The system readout box is configured for a standard 19 inch rack mount and is shown in Figure (6.1). As shown in the photograph, a front panel power switch activates all system functions. Bi-color red-green LED's act as status indicators to visually monitor infrared source stability and thermoelectric cooler stability of the two cooled Lead Sulfide infrared photodetectors. A front panel 4 1/2 digit display of differential vapor transmissivity has a resolution of 0.01 percent and also gives a parallel BCD digital output. A calibration momentary test button can be used to close an electronic shutter to block the 2.67 micrometer detector and yield a stable calibration signal. Separate 'Zero' and 'Span' thumbwheel switches can be used to scale any portion of the output range to available external data system input ranges. Analog Monitor 3NC outputs on the front panel can be used to monitor the differential vapor transmissivity output, source stability, and thermoelectric cooler temperature setpoints.

The remote vapor density transmissometer sensing head is shown in Figure (6.2) mounted on its optical prototyping rail. Figure (6.2) thus illustrates the laboratory prototype physical realization of the electro-optical chain shown schematically in Figure (3.15).



Fig. (6.1) Absolute Humidity Sensor Readout Panel

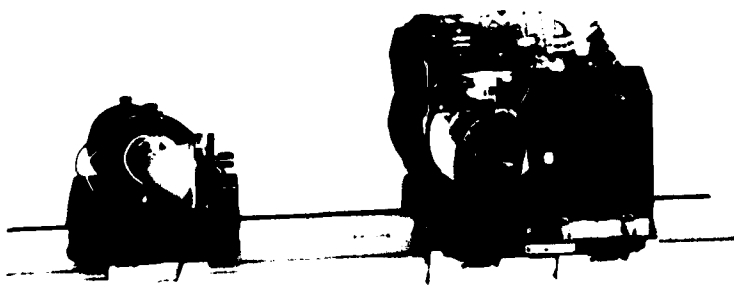


Fig. (6.2) Absolute Humidity Sensor Remote Head

Figure (6.3) is a labeled view of the individual electro-optical components present in the receiver head of Figure (6.2).

Figure (6.4) shows the remote transmissometer head of Figure (6.2) as normally operated in the laboratory inside sealed dessicated light source and receiver enclosures.

6.2 Air Temperature 4.25 Micrometer Radiometer Laboratory Prototype

The currently implemented laboratory prototype physical realization of the 4.25 micrometer air temperature radiometer is also implemented as an electronics and display box attached by cable to a remote sensing head.

As shown in Figure (6.5) the electronics and display box is designed for standard 19 inch rack mounting. A single power switch activates all system functions. Bi-color red-green status indicator lights are provided to show that the rotating chopper wheel is properly phase and frequency synchronized to the lock-in amplifier circuitry and to indicate temperature stability of the thermoelectrically cooled Lead Selenide detector. A 4 1/2 digit front panel display shows the temperature of the rotating chopper wheel to a resolution of 0.01 degrees Celsius. A second 4 1/2 digit panel meter indicates the chopped irradiance signal arising from temperature differences between the atmosphere and the black chopper wheel. Irradiance signal resolution is 0.01 nanowatts of chopped optical power. Both front panel meters provide parallel BCD outputs for connection to external data systems. A front panel 4 digit thumbwheel switch can be used to adjust overall system gain. Front panel analog BNC outputs are used to monitor the chopped irradiance signal, the rotating black chopper temperature, the Lead Selenide thermoelectric cooler temperature setpoint, and the synchronization square wave from the rotating chopper wheel.

Figure (6.6) shows an interior view of the air temperature radiometer remote sensor head with both internal and external covers removed. Individual components are labeled on the figure which thus illustrates the actual laboratory prototype physical realization of the electro-optical and electronic system chain shown schematically in Figures (4.2) through (4.6). In actual laboratory use, the sensor head of Figure (6.6) is enclosed in a sealed metal box and views its atmospheric signal field of view through a 2 inch diameter sapphire window as shown in Figure (6.7).

7 LABORATORY AND FIELD PROTOTYPE TESTING AND CALIBRATION

Laboratory testing and calibration of the air temperature radiometer and differential absolute humidity transmissometer has taken place using Ophir Corporation laboratory facilities and additional calibration standards and facilities provided to the contract by the Aviation Facility of the National Center For Atmospheric Research (NCAR) and the Boulder Atmospheric Observatory (BAO) of the National Oceanic and Atmospheric Administration (NOAA).

An additional opportunity has been made available to the Ophir Corporation, outside the scope of this contract, allowing actual field trials and data gathering and testing in an experiment conducted by Dr. John Gaynor and Mr. Tant Priestly of NOAA at the BAO tower in Erie, Colorado. Both the 4.25 Micrometer Air Temperature Radiometer and the 2.67 Micrometer

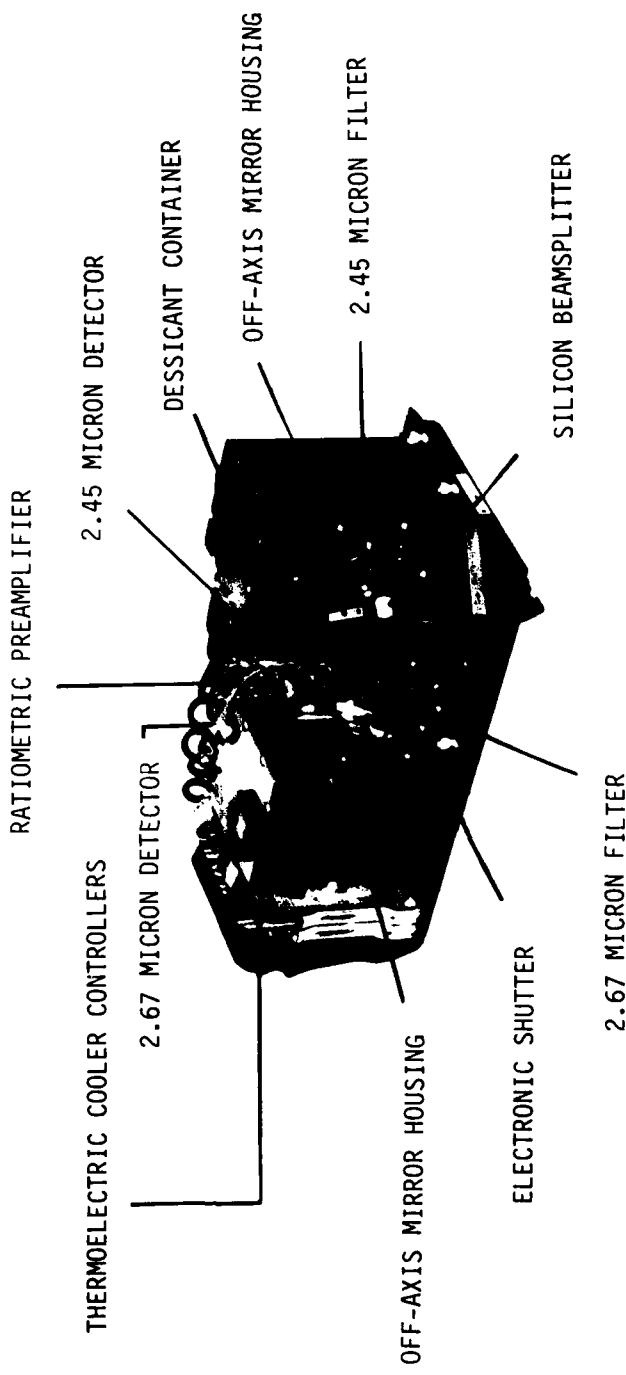


Fig. (6.3) Detailed View of Humidity Sensor Receiver (cover removed)

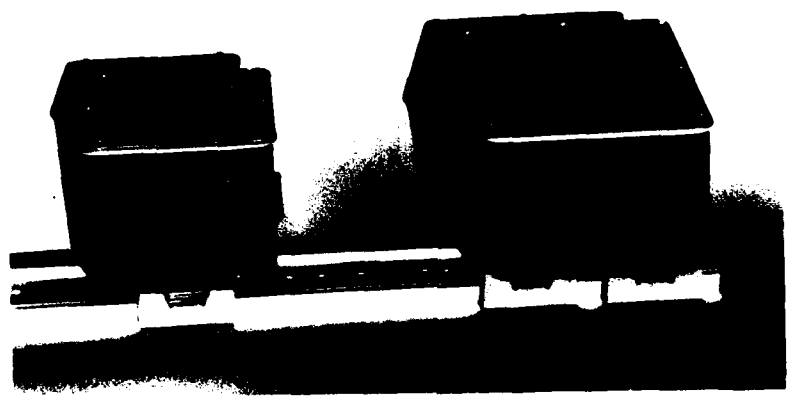


Fig. (6.4) Absolute Humidity Sensor Head (covers in place)



Fig. (6.5) Air Temperature Radiometer Readout Panel

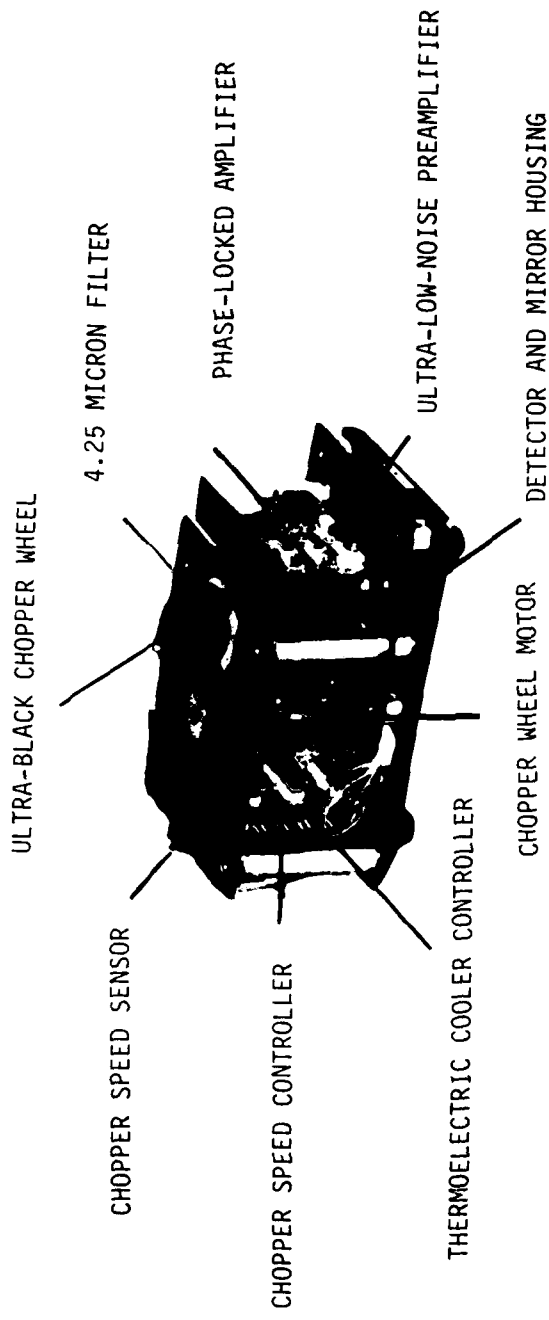


Fig. (6.6) Air Temperature Radiometer Remote Head (covers removed)

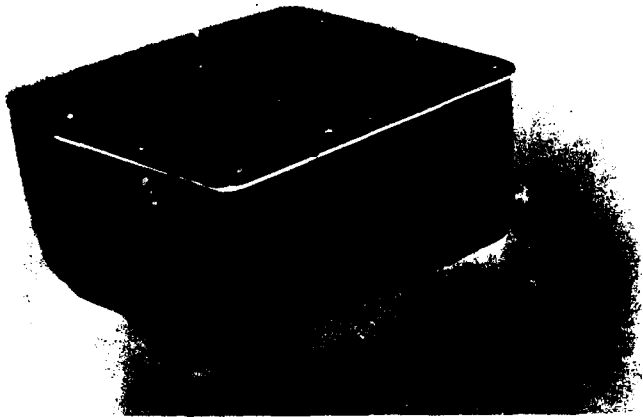


Fig. (6.7) Air Temperature Radiometer Remote Head (covers in place)

Differential Water Vapor Transmissivity Absolute Humidity Sensor prototypes are currently involved in these field trials at the BAO tower as of this writing.

The first preliminary results from these field trials will be reported in this document. Since the majority of the BAO field test data gathering period will take place after the due date of this AFGL final report, those results will be reported in more detail in the Proceedings of the Conference on Cloud Physics, to be held in Chicago, Illinois on November 15-18, 1982.

7.1 Absolute Humidity Sensor Testing

7.1.1 Laboratory Tests

After sensor fabrication as shown in Figures (6.1) through (6.4) a system functionality test was conducted by exhaling and inhaling into a 12 inch long tube placed in the sample beam path. The test was conducted with front panel gain set to unity and front panel offset set to zero (see Figure 6.1). As shown in the chart recorder trace reproduced as Figure (7.1), system functionality and response to water vapor were verified.

In-house tests with an oscilloscope trace recording of sensor response when the front panel test switch was depressed to suddenly occlude the 2.67 micrometer detector indicate a system response time (10 to 90 percent) to changes in absolute humidity of 5 milliseconds.

AD-A121 713

THEORY ELECTRO-OPTICAL DESIGN TESTING AND CALIBRATION
OF A PROTOTYPE ATMO. (U) OPHIR CORP DENVER CO

L D NELSON 15 JUL 82 AFGL-TR-82-0283 F19628-81-C-0071

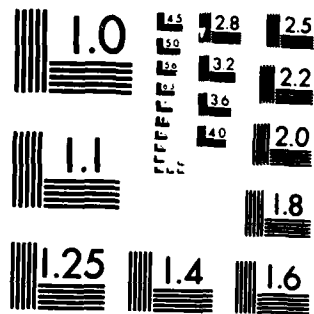
22

UNCLASSIFIED

F/G 4/2,

NL

END
DATA
REMOVED
[REDACTED]
DTIC



MICROCOPY RESOLUTION TEST CHART
NATIONAL BUREAU OF STANDARDS 1963 A

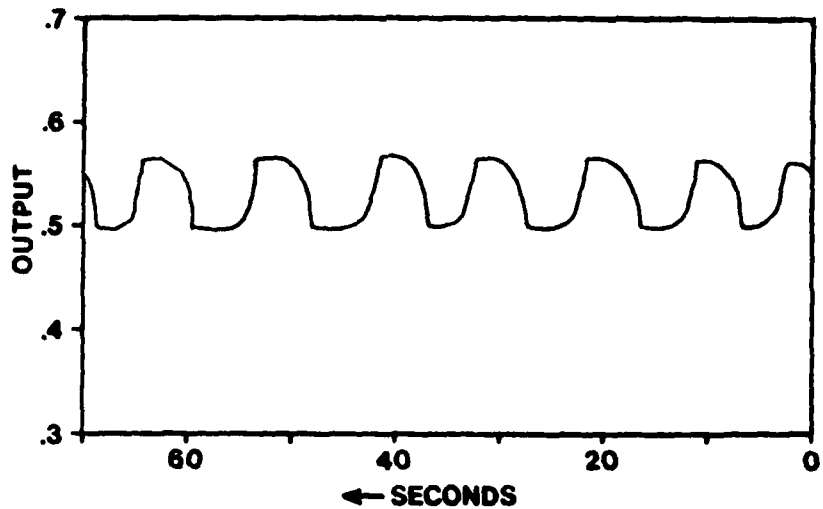


Fig. (7.1) Chart Recorder Trace Resulting from Breathing into Humidity Sensor Beampath

Two significant engineering problems in the implementation of the absolute humidity sensor became apparent during this preliminary in-house testing.

First, only about one percent of the theoretically calculated source intensity calculated in Section (3.2.1) was found to actually be impinging on the sensors. This light loss was traced to the physically large filament size of the 125 watt Osram quartz halogen light source. Since the source size is substantially larger than the 1 mm square detector, it becomes optically impossible to focus a large fraction of its output on the detector with a simple optical chain. The logical solution is a more point-like light source with lower wattage. Since the focused beam intensity on the detectors was smaller than expected, the sensor dark resistance offset terms in Equation (3.25) become relatively large with respect to the optical signals and the simplification of Equation (3.26) is not accurate. Thus the front panel output meter, see Figure (6.1), is not linear in differential transmissivity and responds instead to the more complex Equation (3.25).

Differential calibrated water vapor transmissivity can still, of course, be recovered from the meter reading and sensor constants via the nonlinear Equation (3.25).

When this conversion was made in the laboratory under known humidity conditions for a variety of system optical path lengths, a second engineering problem became apparent. As shown in Figure (7.2) the actual measured system transmissivity response to water vapor in the beam path was significantly less than theoretically expected according to the empirical approximation of Equation (1.5) as graphed in Figures (1.2) and (1.3). The solid line marked (T) is the estimated theoretical response as reproduced from Figure (1.2) and the dashed line shows the experimental measurements.

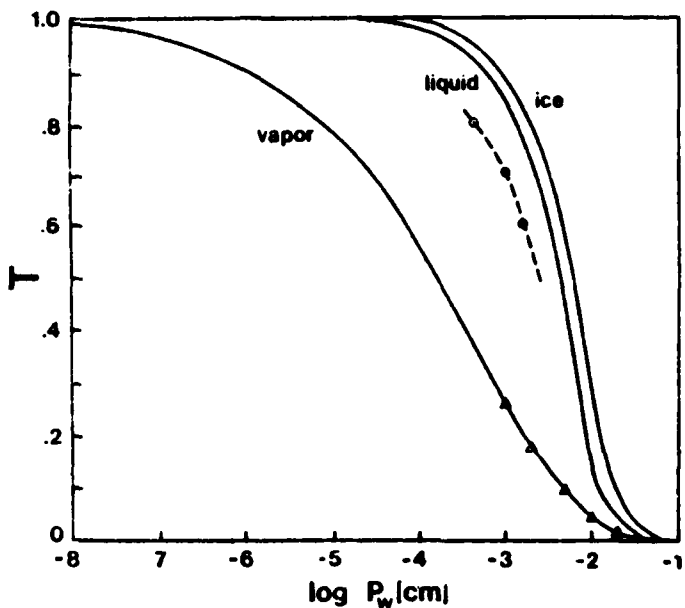


Fig. (7.2) Preliminary Variable Path Tests of Absolute Humidity Sensor

This discrepancy between theory and practice was traced to an out of specification 2.67 micrometer bandpass filter somewhat lower in center wavelength than optimal. The filter was sent to an optical manufacturer to obtain the actual bandpass curve shown as Figure (7.3). Both precision measurements of the filter bandpass curve and the atmospheric carbon dioxide and water vapor absorption bands are shown in the figure. It can be seen that the filter is somewhat low in wavelength and thus its lower bandpass wing is out of the strong water vapor absorption band shown in the figure. Thus, some infrared energy from the source always passes through the lower part of the filter bandpass to the detector, even if the water vapor density were so high as to be totally absorbing in its wavelength band. The result is that transmissivity always reads artificially high due to this low-wing filter leakage as shown in Figure (7.2). As a point of interest, the atmospheric 4.25 micrometer carbon dioxide band absorption used in the passive air temperature radiometer is

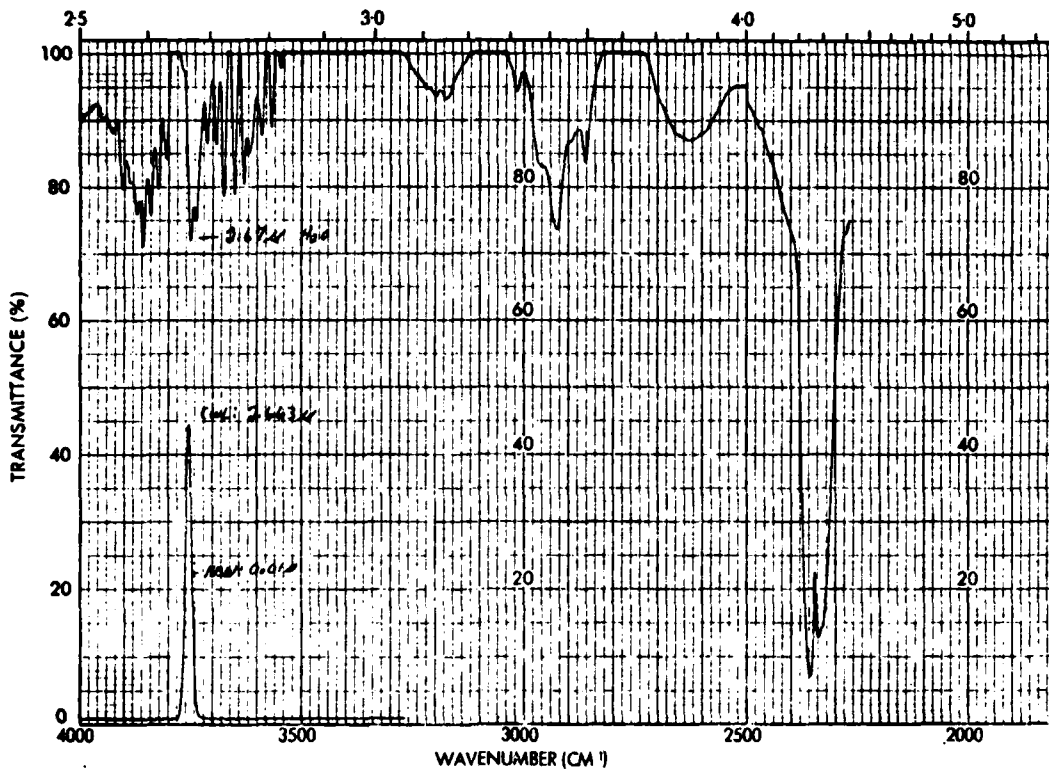


Fig. (7.3) Infrared Spectrophotometer Traces of Actual Filter Bandpass and Atmospheric Absorption Bands

also visible in Figure (7.3).

The obvious solution to this out of optimum specification filter caused offset would be to procure another filter at the proper wavelength and bandpass. Unfortunately, this has not been possible within the temporal scope of this contract since custom infrared filter fabrication lead times exceed four months.

Fortunately, valid data can still be collected with the prototype absolute humidity sensor since this offset affects only an arbitrary calibration term; and sensor calibration against a series of known humidities is required to establish system constants in any case. Measured system short term optical stability of the ratiometric optical output exceeds 0.01 percent and thus the front panel zero and span controls, see Figure (6.1), can be used to scale the system transmissivity response of Figure (7.2) to fill completely a 0 to 10 VDC analog data recording system input range. This scale expansion and shift has the effect of electronically lengthening the effective path length, thus permitting full scale humidity reading changes in a 12 inch path length

system in spite of the non-optimal 2.67 micrometer center wavelength bandpass filter. A future system with a better filter would have a short pathlength without this tradeoff of electronic path shortening for increased system noise.

We had intended to calibrate the absolute humidity sensor in a temperature-humidity chamber maintained by NOAA in Boulder. However, the 12 inch path length requirement necessitated by the non-optimal filter no longer permits this prototype sensor to fit inside the chamber for testing. Absolute humidity sensor calibration will thus take place in the free atmosphere using a dew-point cooled mirror hygrometer as discussed in the next section.

7.1.2 Field Testing and Calibration

As discussed earlier in this section, field testing of both the air temperature radiometer prototype and the absolute humidity sensor prototype is currently in progress at the NOAA/BAO Tower. While these tests are funded internally by NOAA and Ophir Corporation and will not be completed until after the due date of this Final Report under AFGL sponsorship, preliminary results will be given here.

The two Ophir Corporation sensors and a number of other accurate and/or fast response humidity and temperature sensors are exposed together on a 20 foot tower at the BAO site in Erie, Colorado. The tested sensors and their placement on the tower are shown in Figure (7.4). Simultaneous sensor data outputs are recorded digitally on two data systems with sample times of 0.01 and 0.1 seconds.

As can be seen in Figure (7.4), the two Ophir Corporation sensors have been modified for this test series. Modifications to the air temperature radiometer were minor, including an exterior coat of high-reflectance white paint and internal changes to improve system offsets and ground loop problems. Improvements to the Ophir absolute humidity sensor also included a new hermetically sealed infrared source with a smaller more point-like emitter, lower power (25 watts), and tighter beam focus. As discussed earlier in this section, the front panel gain and offset on the absolute humidity sensor have been adjusted to fill the available data system resolution (0 to 10 VDC) in spite of the non-optimal 2.67 micrometer filter in the existing prototype.

Preliminary results of a tower calibration of the Ophir absolute humidity sensor against a cooled-mirror dew-point hygrometer are given in Figure (7.5). Twenty minutes of fast response data are shown; each point shown corresponds to a 10 second average. Figure [7.5(a)] shows the Ophir vapor transmissometer output voltage plotted against the aspirated EG and G dew point reading and Figure [7.5(b)] shows the output voltage of a Lyman-Alpha hygrometer plotted against the same dew point record. It can be seen that the Ophir absolute humidity sensor is stable within about 0.5 degrees of the dew point hygrometer readout in spite of the non-optimal nature of the present prototype. The Ophir transmissometer and the Lyman-Alpha scatter diagrams show virtually identical scatter and excellent internal consistency. Thus much of this 0.5 degree scatter range seems to be due to the slow response of the dew point instrument.

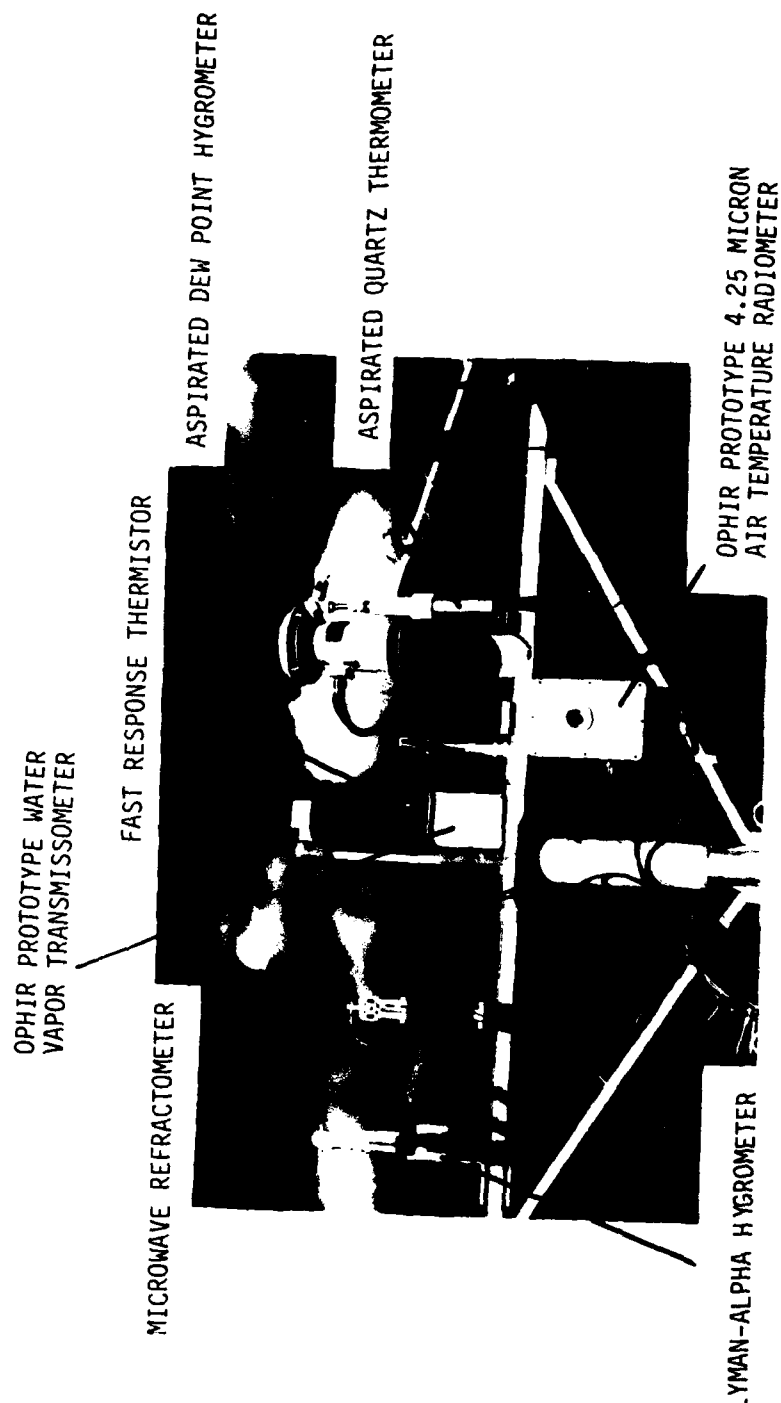


Fig. (7.4) Sensor Placement on NOAA/BAO Tower

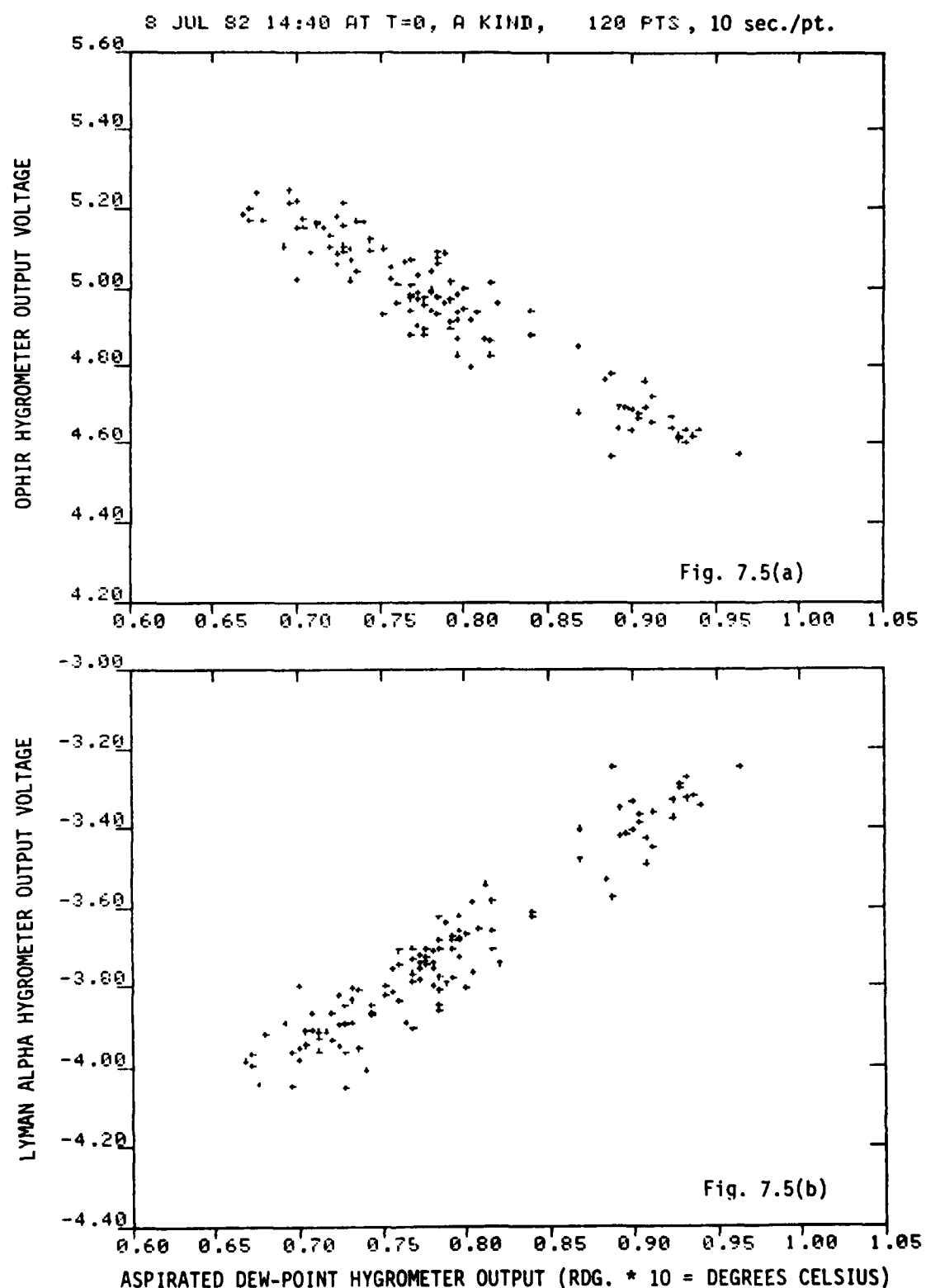


Fig. 7.5(a) Scatter Diagram - Ophir Vapor Transmissometer Output Voltage versus Aspirated Dew Point Hygrometer Reading in Degrees Celsius

Fig. 7.5(b) Scatter Diagram - NCAR Lyman-Alpha Hygrometer Output Voltage versus Aspirated Dew Point Hygrometer Reading (10 second averages)

Fast response comparisons to a Lyman-Alpha Humidity Sensor and co-spectral comparisons to a colocated fast response temperature sensor on time scales of 0.01 second will become available after this present AFGL contract terminates and will be presented at the Cloud Physics Conference in Chicago, Illinois, in November of 1982.

7.2 Air Temperature 4.25 Micrometer Radiometer Calibration and Testing

7.2.1 Laboratory Tests and Calibration

The prototype 4.25 Micrometer Air Temperature Radiometer has exceeded our design goals in all respects and shows promise of becoming a new standard air temperature measuring device which simultaneously combines both fast response and high absolute accuracy in a field and airborne environment. Radiation shields and compressability corrections are both unnecessary in this infrared optical sensor. A significant advantage of this 4.25 micrometer radiometer is its near sensor weighting of the temperature spatial weighting function as theoretically estimated in Figure (1.10). In this wavelength band, air becomes essentially black in one to ten meters, about 2 orders of magnitude faster than the more conventional 14-16 micrometer band used in previous air temperature radiometers. Figure (7.6) shows an experimental verification of this rapid approach to blackness in the temperature spatial weighting function which provides the 4.25 micrometer radiometer with many of its operational advantages. The individual data points shown on Figure (7.6) were obtained by moving the sensing head calibrated distances away from an Aztec radiant heater panel serving as a beamfilling large area greybody source. The theoretical and experimental curves labeled (T) for transmissivity can be interpreted as that fraction of the radiometer's temperature weighting function coming from distances greater than (T) from the sensor head. It can be seen that the sample weighting function actually falls off somewhat more rapidly than the theoretical estimate given in Section (1.4.2). Fifty percent of the sensor experimental weighting comes from the first 75 centimeters of path length while the theoretical curve shown predicts 1 meter. This experimental improvement in sample volume probably occurs since the theory assumed a top-hat filter profile while the actual filter bandpass is somewhat gaussian and thus weights the strongly absorbing band center more strongly. Recall that the details of this weighting curve affect only the sample volume over which the temperature reading is averaged. Temperature accuracy is independent of the spatial weighting function so long as the field of view goes to blackness in a reasonably isothermal sampled path length. This condition is easily met in the 4.25 micrometer band but is questionable in the two orders of magnitude weaker 14-16 micrometer band.

Calibrations of the absolute accuracy of the prototype 4.25 micrometer radiometer were accomplished using facilities and an EG and G Model 1100 Low Temperature Blackbody Calibration Standard provided to the contract by the Aviation Facility of the National Center for Atmospheric Research. In these trials the chopper temperature was allowed to float at ambient temperature of about 23 to 25 degrees Celsius and the blackbody honeycomb calibration source was varied over a range of 50 degrees. The sensor window and the calibration source were placed within 1 inch of each other and the intervening space was purged with laboratory grade dry

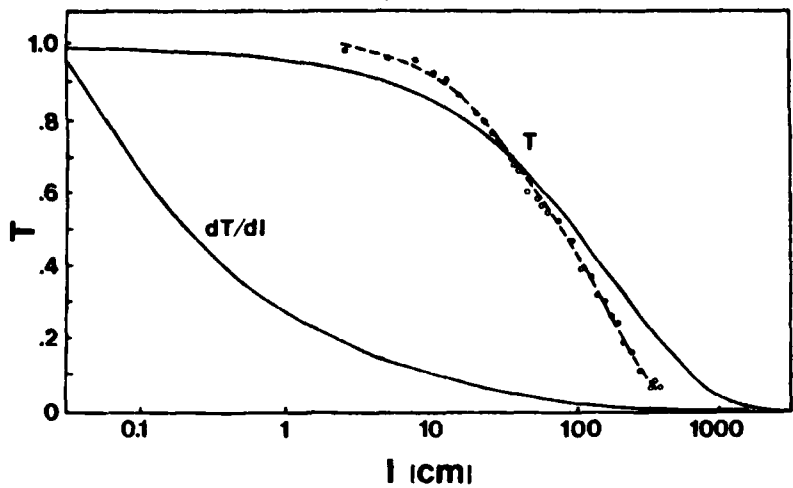


Fig. (7.6) Ophir Air Temperature Radiometer Spatial Weighting Function

nitrogen to eliminate air temperature contributions to the received irradiance. Chopper temperature, air temperature, and black body calibration source temperature were recorded to high accuracy and the radiometer estimates of the known EG and G Model 1100 blackbody source temperature were then calculated from the measured instrument chopper temperature and the measured differential signal irradiance (see Figure 6.1) via a dual application of Planck's law.

Results of this laboratory calibration are shown in Figure (7.7). Calibration source temperature was recovered from the 4.25 micrometer radiometer measurements to an accuracy of 0.2 degrees Celsius over a tested range of 50 degrees Celsius in source temperature as shown in the figure. Since the published accuracy of the EG and G Model 1100 Black Body Calibration Standard is 0.2 degrees Celsius, it seems likely that the accuracy of the Ophir prototype 4.25 micrometer Air Temperature Radiometer exceeds this value.

The RMS noise equivalent temperature fluctuations due to sensor electronics are about 0.01 degrees Celsius into a 1 Hz bandwidth at 25 degrees Celsius. A five to ten fold improvement in this specification seems theoretically practical in the next generation sensor redesign.

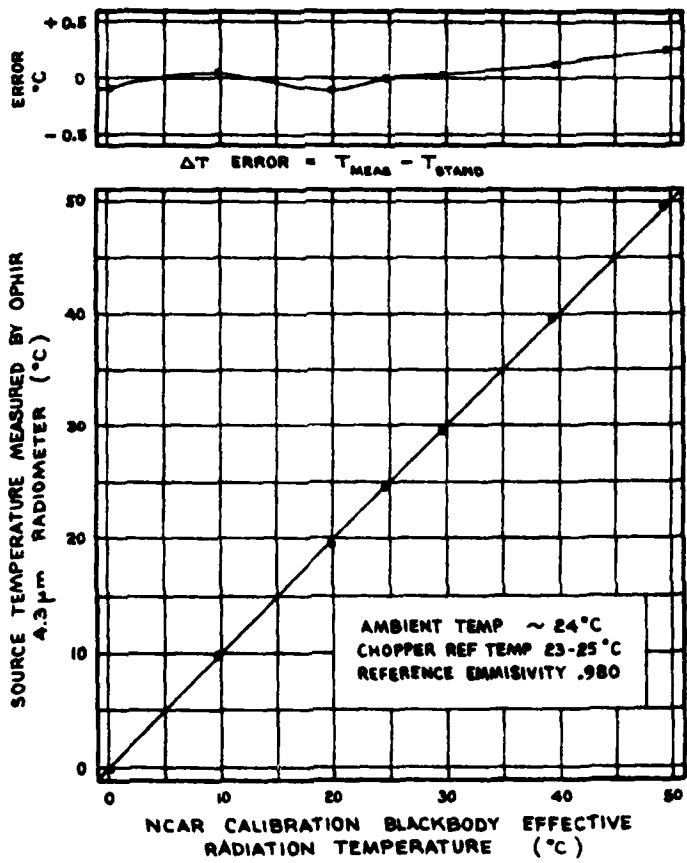


Fig. (7.7) Laboratory Calibration of the Absolute Temperature Accuracy of the Ophir 4.25 Micrometer Radiometer

7.2.2 Field Tests of the 4.25 micrometer Air Temperature Radiometer

The first field tests of the 4.25 micrometer radiometer are also now beginning at the NOAA/BAO tower as of this writing. A description of these field trials has been given in Section (7.1.2) and a photograph of the tower installation is shown in Figure (7.4). No analyzed data from the 4.25 micrometer radiometer and comparison aspirated quartz thermometer on the tower is not yet available as of the due date of this AFGL final report. Detailed results of these comparisons will be presented at the Cloud Physics Conference to be held in Chicago, Illinois, in November of 1982.

8 SUMMARY AND CONCLUSIONS

8.1 Design Feasibility

Design feasibility of both the 4.25 Micrometer Air Temperature Radiometer and the 2.67 Micrometer Differential Absolute Humidity Transmissometer has been conclusively proven by design, fabrication, and successful laboratory testing of proof-of-concept prototype hardware as required by the contract. All significant design goals as called out in Section (5) have been met and in some cases exceeded.

Performance of the 4.25 micrometer Short Path Air Temperature Radiometer has exceeded our expectations. It now seems likely that the next-generation redesign of the air temperature radiometer will result in a sensor which could become a new standard in both ground-based and airborne in situ air temperature thermometry. Both high accuracy and fast response can be attained in a single sensor which requires no aspiration, radiation shielding, or air-speed compressibility corrections. Valid measurements can theoretically be expected in rain, inside clouds, and at ice and water supersaturations without errors due to sensor wetting.

Design feasibility of the 2.67 micrometer Differential Absolute Humidity Sensor has been shown in spite of a non-optimally fabricated 2.67 micrometer bandpass filter in the prototype sensor. Higher than expected sensor signal to noise ratios in the transmissometer permit the available smaller than expected output signal level to be scaled to full scale data system values without excessive noise. Further improvements in resolution can be expected when a more optimal filter is procured in possible follow on redesign of the humidity sensor. Transmissivity signal stability of about 0.01 percent and response time of about 5 milliseconds has been attained in the proof of concept absolute humidity prototype.

The first trials of the potential utility of using the two sensors together to compute derived quantities from the non-contact, fast-response, measurements of true air temperature and absolute humidity are now beginning at the NOAA/BAO Tower facility in Erie, Colorado. Use of the two sensors together as discussed in Sections (1.1) and (1.5) should permit a variety of atmospheric measurements which have never before been practical within the limitations of existing sensors. Some of these potential end uses are described in Section (1.1). They include accurate in-cloud measurements of relative humidity and supersaturations with respect to both water and ice and calculations of the small scale refractive index structure of the undisturbed atmosphere on time scales approaching 0.01 seconds.

8.2 Recommendations for Future Work

Field trials of both sensors in a ground environment are now in progress and will provide much new information and insight on sensor capabilities and shortcomings.

Since many of the significant advantages and areas of utilization of the two sensors involve airborne measurements inside clouds, they should be redesigned and tested in an airborne environment as soon as possible.

Since the present sensor prototypes were designed under the contract to prove technical feasibility in the laboratory in a cost effective manner, they are far from optimal with regard to size, weight, power consumption, streamlining, and environmental survivability. Significant improvements in all of these areas as well as signal accuracy and signal to noise ratio are attainable in the next generation design making use of the learning process under this development.

Artist's conceptions of this next generation airborne redesign of the 4.25 micrometer Air Temperature Radiometer and the 2.67 micrometer Differential Water Vapor Transmissometer are given in Figures (8.1) and (8.2). Design changes and improvements envisioned in these redesigns

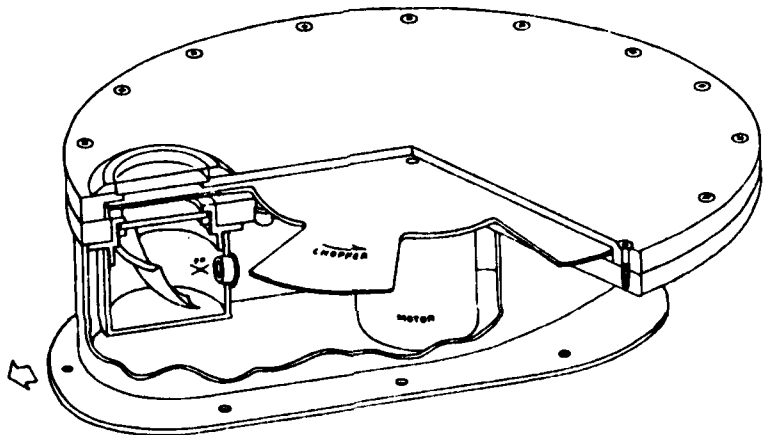


Fig. (8.1) Artist's Conception - Airborne 4.25 Micrometer Air Temperature Radiometer

include:

- (1) Airworthy and field survivable packaging.
- (2) Wide temperature range electronic component specifications.
- (3) Digital, optically isolated data transmission from sensor heads to electronic receivers to avoid ground loop and interference problems common on aircraft and long cable runs.

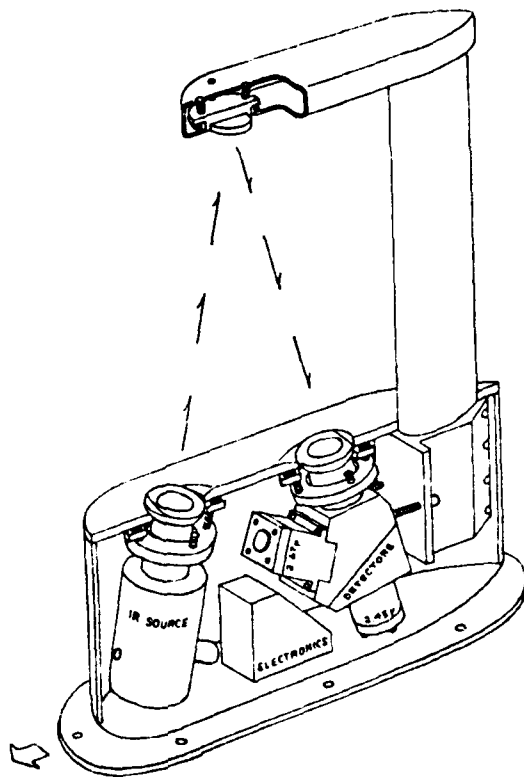


Fig. (8.2) Artist's Conception - Airborne 2.67 Micrometer Water Vapor Transmissometer

- (4) Operation from 28 VDC aircraft power, including filtering and point-of-use regulation at the sensor heads and local high quality analog grounding (110 VAC power options for ground use will also be included).
- (5) An improved and miniaturized refractive infrared optical chain in the absolute humidity sensor.
- (6) Integration of the beamsplitter and 2.45 micrometer filter in the absolute humidity sensor to a single optical element.
- (7) Provision for filter tilt adjustment in the absolute humidity sensor to maximize signal and minimize pathlength.

- (8) Window Heating to permit airborne and field use in clouds and at high humidity.
- (9) Vibration isolation to eliminate possible PbSe and PbS sensor microphonics in airborne use.
- (10) Added stages of sensor thermoelectric cooling in both the temperature and humidity sensors to reduce offsets, permit lower power light sources, improve signal-to-noise ratios, and permit use at high altitudes.
- (11) A completely re-engineered, lower power, and more 'pointlike' light source for the absolute humidity sensor.
- (12) A wide temperature range, low noise motor for the photchopper wheel in the radiometer to permit faster rotation.
- (13) Improvements in the temperature sensor phase-locked low-noise amplifier to reduce background noise and offset and thus improve temperature resolution, especially at high cold altitudes.

9 ACKNOWLEDGMENTS

A number of scientific and technical personnel outside Ophir Corporation have made contributions to the development and testing of the sensing technology presented herein. Dr. Arnold Barnes, Mr. Vernon Plank, and Mr. Robert Berthel of AFGL provided technical discussions and hardware equipment loans under the contract. A Black-Body Calibration Test Facility was made available by Dr. Byron Phillips and Mr. Alex Kennel of the NCAR Aviation Facility. Encouragement and laboratory and field test facilities were made available by Dr. Chandrin Kaimal of NOAA and Dr. John Wyngaard of NCAR. Dr. John Gaynor and Mr. Tant Priestley of NOAA made it possible for these sensors to take part in ongoing field trials at the Boulder Atmospheric Observatory. Field support was provided by Mr. Don Wolf, Mr. Norbert Szczepczynski, and Mr. Jim Newman of the Boulder Atmospheric Observatory.

REFERENCES

Albrecht, B.A., S.K. Cox and W.H. Schubert, 1979: Radiometric measurements of in-cloud temperature fluctuations, J. Appl. Meteor., 18, 1066-1071.

Allen, L.B. and J.L. Kassner, 1969: J. Coll. and Interface Science, 30, 81.

Anderson, B.J. and J. Hallett, 1976: Supersaturation and time dependence of ice nucleation from the vapor on single crystal substrates, J. Atmos. Sci., 33, 822-832.

Astheimer, R.W., 1962: An infrared radiation air thermometer Proc. Univ. of Michigan Symposium on Remote Sensing of Environment, Oct. 17, 1962.

Balsley, B., 1981: Doppler radar measurements of clear-air atmospheric turbulence at 1290 megahertz, J. Appl. Meteor., 20, 3, 266-274.

Bigg, E.K. and R.T. Meade, 1971: Clear air seeding in the presence of ice supersaturation, Proc. of the International Conference on Weather Modification, Canberra, Australia, Sept. 6-11, 1971, American Meteorological Society, 141-142.

Bogolomova, L.V., V.I. Dianov-Klokov and S.L. Zubkovskiy, 1974: Double beam infrared spectrometer for measuring humidity fluctuations in the atmosphere, Izvestia, Atmospheric and Oceanic Physics, 10, 9, 933-942.

Braham, R.R. and P. Spyers-Duran, 1967: Survival of cirrus crystals in clean air, J. Appl. Meteor., 6, 1053-1061.

Burch, D.E., E.B. Singleton and D. Williams, 1962: Absorption line broadening in the infrared, Appl. Optics, 1, 3, 359-363.

Carlton, H.R., 1978. Phase transition changes in the molecular absorption coefficient of water in the infrared: evidence for clusters, Appl. Optics, 17, 20, 3192-3195.

Carlton, H.R., 1979: Ion content and infrared absorption of moist atmospheres, J. Atmos. Sci., 36, 832-837.

Carlton, H.R., 1979b: Variations in emission spectra from warm water fogs: evidence for clusters in the vapor phase, Infrared Physics, 19, 49-64 (Great Britain).

Chylek, P., 1978: Extinction and liquid water content of fogs and clouds, J. Atmos. Sci., 35, 296-300.

Clark, T.L., 1973: Numerical modeling of the dynamics and microphysics of warm cumulus convection, J. Atmos. Sci., 30, 857-878.

Das, P., 1969: The thermodynamic equation in cumulus dynamics, J. Atmos. Sci., 26, 399-407.

Eckert, E.R.G. and R.M. Drake, Jr., 1972: Analysis of heat and mass transfer, McGraw-Hill, 1972, 806 pp.

Edwards, G.R. and L.F. Evans, 1960: Ice nucleation by silver iodide, I: freezing vs. supersaturation, J. Meteor., 17, 627-634.

Edwards, O.J., 1966: Optical transmittance of fused silica at elevated temperatures, J. Opt. Soc. Am., 56, 10, 1314-1319.

Elsasser, W.M. and M.F. Culbertson, 1960: Atmospheric Radiation Tables, Meteor. Monographs, 4, 23, 43 pp.

Foskett, L.W., N.B. Foster, W.R. Thickstun and R.C. Wood, 1953: Infrared absorption hygrometer, Monthly Weather Review, 81, 267-277.

Fowle, F.E., 1912: The spectroscopic determination of aqueous vapor, Astrophys. J., 35, 3, 149-162.

Gagin, A., 1972: The Effect of supersaturation on the ice crystal production by natural aerosols, J. Rech. Atmos., 6, 175-185.

Gerber, H.E., 1981: Microstructure of a radiation fog, J. Atmos. Sci., 38, 2, 454-458.

Hale, B.N. and P.L.M. Plummer, 1974: On nucleation phenomena I: A molecular model, J. Atmos. Sci. 31, 6, 1615-1621.

Hall, W.D. and H.R. Pruppacher, 1976: The survival of ice particles falling from cirrus clouds in subsaturated air, J. Atmos. Sci., 33, 10, 1995-2006.

Harrison, T.R., 1960: Radiation Pyrometry and Its Underlying Principles of Radiant Heat Transfer, John Wiley and Sons, N.Y. 232 pp.

Heist, R.H. and H. Reiss, 1973: J. Chem. Phys., 59, 665.

Howard, J.N., 1963: Errors in infrared absorption measurements due to wall adsorption of water vapor Appl. Optics, 2, 11, 1196-1197.

Howell, W.E., 1949: The growth of cloud drops in uniformly cooled air, J. Meteor., 6, 134-149.

Huffman, P.J., 1973: Supersaturation spectra of AgI and natural ice nuclei, J. Appl. Meteor. 12, 1080-1082.

Hyson, P. and B.B. Hicks, 1975: A single beam infrared hygrometer for evaporation measurement, J. Appl. Met., 14, 3, 301-307.

Irving, W.M. and J.B. Pollack, 1968: Infrared optical properties of water and ice spheres, Icarus, 8, 324-360.

Johns, J.W.C., 1965: The Absorption of Radiation by Water Vapor, Humidity and Moisture, Vol. I (New York: Reinhold) 417-427.

Johnson, G.N. and P.L. Smith, Jr., 1980: Meteorological instrumentation system on the T-28 thunderstorm research aircraft, Bull. Am. Met. Soc., 61, 9 972-979.

Johnson, J.C., 1963: Physical Meteorology, The MIT Press, Cambridge, Mass. 393 pp.

Kaimal, J.C. and J.A. Businger, 1963: A continuous wave sonic anemometer-thermometer, J. Appl. Meteor., 2, 156-164.

Knollenberg, R.G., 1972: Measurements of the growth of the ice budget in a persisting contrail, J. Atmos. Sci., 29, 1367-1374.

Kuhn, P.M., 1970: Airborne observations of contrail effects on the thermal radiation budget, J. Atmos. Sci., 27, 937-942.

Lala, G.G., 1969: M.S. Thesis, State Univ. of New York at Albany, Albany, N.Y.

Lamb, D. and P.V. Hobbs, 1971: Growth rates and habits of ice crystals grown from the vapor phase, J. Atmos. Sci., 28, 1506-1509.

Lin, S.S., 1977: Detection of large water clusters by a low RF quadrupole mass filter, Review of Scien. Instru., 44, 4, 516-517.

List, R.J., 1963: Smithsonian Meteorological Tables, Smithsonian Institution Press, Washington, D.C. 527 pp.

Low, R.D.H., 1967: Acoustic Measurement of Supersaturation in a Warm Cloud, U.S. Army Electronics Command, Report No. ECOM-5146.

McKay, D.J., 1978: A sad look at commercial humidity sensors for meteorological applications, Fourth Symposium on Meteorological Observations and Instrumentation, American Meteorological Society, 7-14.

Middleton, W.E.K., 1958: Vision through the Atmosphere, Oxford Univ. Press, London, 250 pp.

Neilburger, M. and C.W. Chien, 1960: Computation of the growth of cloud drops by condensation using an electronic digital computer, Physics of Precipitation, Geophys. Mono., 5, Amer. Geophys. Union, 191-209.

Nelson, L.D., 1979: Observations and Numerical Simulations of Precipitation Mechanisms in Natural and Seeded Convective Clouds, Ph.D. Dissertation, Univ. of Chicago (also avail. as Univ. of Chicago Cloud Physics Lab. Tech. Note No. 54)

Owiccki, J.C., L.L. Shipman and H. A. Scherago, 1975: Structure, energetics and dynamics of small water clusters, J. Phys. Chem., 79, 17, 1794-1811.

Pinnick, R.G., S.G. Jennings, P. Chylek, and H.J. Auermann, 1979: Verification of a linear relation between infrared extinction, absorption liquid water content of fogs, J. Atmos. Sci., 36, 1577-1586.

Platt, C.M.R., 1976: Infrared absorption and liquid water content in stratocumulus clouds, Quart. J. Royal Met. Soc., 102, 553-561.

Pruppacher, H.R. and J.D. Klett, 1978: Microphysics of clouds and precipitation, Dordrecht, Holland, D. Reidel Publ. Co., 714 pp.

Randall, 1975: Optical engineering, Vol. 14, No. 1.

Rothman, L.S., S.A. Clough, R.A. McClatchey, L.G. Young, D.E. Snider, and A. Goldman, 1978: AFGL Trace Gas Compilation, Appl. Optics, 17, 4, 507.

Rottner, D. and G. Vali, 1974: Snow crystal habit small excesses of vapor density over ice saturation, J. Atmos. Sci., 31, 560-569.

Searcy, J.G. and J.B. Fenn, 1974: Clustering of water on hydrated protons in supersonic free jet expansion, J. Chem. Phys., 61, 12, 5282-5288.

Showalter, A.K., 1965: State-of-the-art survey on the application of hygrometry to meteorology, Humidity and Moisture, Vol II (New York: Reinhold), 441-445.

Soong, S.T., 1974: Numerical simulation of warm rain development in an axisymmetric cloud model, J. Atmos. Sci., 31, 1262-1285.

Staats, W.F., L.W. Foskett and H.P. Jensen, Infrared absorption hygrometer, Humidity and Moisture, Vol 1, (New York: Reinhold) 465-480.

Stewart, D.A., 1977: Infrared and submillimeter extinction by fog, Tech. Report TR-77-9, U.S. Army Missile Research and Development Command Redstone Arsenal, Alabama (also available from the NCAR library as Reference No. 17812).

Stull, V.R., P.J. Wyatt and G.N. Plass, 1964: The infrared transmittance of carbon dioxide, Appl. Optics, 3, 2, 243-254.

Subbarao, M.C. and P. Das: Microphysical implications of precipitation formation in an adiabatic vertical current: aerosol scavenging by enhanced nucleation, J. Atmos. Sci., 32, 2338-2357.

Suck. S.H., J.L. Kassner Jr. and Y. Yamaguchi, 1979: Water cluster interpretation of infrared absorption spectra in the 8-14 micron wavelength region, Appl. Optics, 18, 15, 2609-2617.

Tampieri, F. and C. Tomasi, 1976: Size distribution models of fog and cloud droplets and their volume extinction coefficients at visible and infrared wavelengths, Pure and Appl. Geophy., 114, 571-586.

Tank, W. G. and E. J. Wergin, 1965: A long path infrared hygrometer, Humidity and Moisture, Vol 1, (Reinhold: New York), 481-491.

Tillman, J. E., 1965: Water vapor density measurements utilizing the absorption of vacuum ultraviolet and infrared rotation, Humidity and Moisture, Vol 1, (Reinhold: New York), 428-443.

Tomasi, C. and R. Guzzi, 1974: High precision atmospheric hygrometry using the solar infrared spectrum, J. of Phys. E: Sci. Instruments, 7, 647-649.

Vasko, A., 1960: Infrared Radiation, CRC Press, Cleveland, Ohio, 364 pp.

Vyaltseva, E. Ye., F. Ya. Klinov, and N.P. Tofanchuk, 1967: Optical instrument for measurement of absolute atmospheric humidity, Leningrad. Institute Prinkladnoy Geofiziki, Trudy (Institute of Applied Geophysics, Transactions) 10, 60-66.

Wexler, A. and L. Greenspan, 1971: Vapor pressure equation for water in the range 0 to 100 C, J. Res. Nat. Bur. Stand. U.S., 75A, (Phys. and Chem.), 3, 213-230.

Wollman, L. R., 1979: The thermopile - the commercial infrared detector, Electro Opt. Sys. Design, 37-43.

Wood, P. C. 1958: Improved infrared absorption spectra hygrometer, Rev. Sci. Instr., 29, 1, 36-42.

Wyatt, P. J., V. R. Stull and G. N. Plass, 1962: Infrared Transmission Studies, Final Report, Vol. II, The Infrared Absorption of Water Vapor, Space Systems Division, Air Force Systems Command, Contract No. AF19(604-7479), Report No. SSD-TDR-62-127 and SSD-TDR-62-128.

Wyatt, P.J., V.R. Stull and G.N. Plass, 1964: The infrared transmittance of water vapor, Appl. Optics, 3, 2, 229-241.

APPENDIX I (Manufacturer's Data Sheets)

IR THIN FILM PRODUCTS
WALTHAM, MASSACHUSETTS

4-29-81

Filter No. 7-4245

Date 4-29-81

Calib Date 0-6

Full Scale 176

Ambient Temp 28

Instrument Beckman IR-4

28

